2008

NOVEL CATALYSTS FOR THE PRODUCTION OF CO- AND CO_2-FREE HYDROGEN AND CARBON NANOTUBES BY NON-OXIDATIVE DEHYDROGENATION OF HYDROCARBONS

Wenqin Shen
University of Kentucky, wq.shen@uky.edu

Recommended Citation
Shen, Wenqin, "NOVEL CATALYSTS FOR THE PRODUCTION OF CO- AND CO_2-FREE HYDROGEN AND CARBON NANOTUBES BY NON-OXIDATIVE DEHYDROGENATION OF HYDROCARBONS" (2008). *University of Kentucky Doctoral Dissertations*. 689.
https://uknowledge.uky.edu/gradschool_diss/689

ABSTRACT OF DISSERTATION

Wenqin Shen

The Graduate School

University of Kentucky

2009

NOVEL CATALYSTS FOR THE PRODUCTION OF CO- AND CO_2-FREE HYDROGEN AND CARBON NANOTUBES BY NON-OXIDATIVE DEHYDROGENATION OF HYDROCARBONS

ABSTRACT OF DISSERTATION

A dissertation submitted in partial fulfillment of the
requirements for the degree of Doctor of Philosophy in the
College of Engineering
at the University of Kentucky

By
Wenqin Shen

Lexington, Kentucky

Director: Dr. Gerald P. Huffman, Professor of Chemical Engineering

Lexington, Kentucky

2009

ABSTRACT OF DISSERTATION

NOVEL CATALYSTS FOR THE PRODUCTION OF CO- AND CO_2-FREE HYDROGEN AND CARBON NANOTUBES BY NON-OXIDATIVE DEHYDROGENATION OF HYDROCARBONS

Non-oxidative dehydrogenation of hydrocarbons is an attractive alternative route for the production of CO- and CO_2-free hydrogen. It will satisfy a major requirement for successful utilization of polymer electrolyte membrane (PEM) fuel cells (< 10 ppm CO) and sequestering carbon as a potentially valuable by-product, carbon nanotubes (CNTs). Due to the deposition of carbon on the surface of catalyst particles during the reaction, catalyst performance, life-time, and purification of the generated carbon product, are significant issues to solve in order to make the process practically feasible. The scope of this thesis includes: the development of novel Fe, Ni, and Fe-Ni catalysts supported on a Mg(Al)O support to achieve improved catalytic performance with easily-purified CNTs; evaluation of catalysts for ethane/methane dehydrogenation at moderate reaction temperatures; and study of activation and deactivation mechanisms by a variety of characterization techniques including TEM, HRTEM, XRD, Mössbauer spectroscopy, and x-ray absorption fine structure (XAFS) spectroscopy. The Mg(Al)O support was prepared by calcination of synthetic MgAl-hydrotalcite with a Mg to Al ratio of 5. The catalysts were prepared either by conventional incipient wetness method or by a novel nanoparticle impregnation method, where the monodisperse catalyst nanoparticles were prepared in advance by thermal decomposition of a metal-organic complex in an organic-phase solution and then dispersed onto the Mg(Al)O support. Dehydrogenation of undiluted methane was conducted in a fix-bed plug-flow reactor. Before reaction, the catalysts were activated by reduction in hydrogen. Fe-based catalysts exhibit a higher hydrogen yield at temperature above 600ºC compared with monometallic Ni catalyst. FeNi-9 nm/Mg(Al)O, Fe-10 nm/Mg(Al)O and Fe-5 nm/ Mg(Al)O nanoparticle catalysts show much improved performance and longer life-times compared with the corresponding FeNi IW/Mg(Al)O and Fe IW/Mg(Al)O catalysts prepared by incipient wetness. 10 nm is the optimum particle size for methane dehydrogenation. Addition of Ni to Fe forming a bimetallic FeNi alloy catalyst enhances the catalytic performance at the temperatures below 650ºC. Metallic Fe, Ni, FeNi alloy and Fe-Ni-C alloy, unstable iron carbide are all catalytically active components. Catalysts deactivation is due to the carbon encapsulation. The carbon products are in the form of stack-cone CNTs (SCNTs) and multi-walled CNTs (MWNTs), depending on the reaction temperature and catalyst composition. The growth of CNTs follows a tip growth mechanism and the purity of cleaned CNTs is more than 99.5%.

KEYWORDS: Non-oxidative dehydrogenation; Nanoparticle impregnation; Monodisperse nanopartilces; CO_x-free hydrogen; Carbon nanotubes

Wenqin Shen

Jan, 2009

NOVEL CATALYSTS FOR THE PRODUCTION OF CO- AND CO_2-FREE HYDROGEN AND CARBON NANOTUBES BY NON-OXIDATIVE DEHYDROGENATION OF HYDROCARBONS

By

Wenqin Shen

Dr. Gerald P. Huffman
Director of Dissertation

Dr. Barbara L. Knutson
Director of Graduate Studies

Jan, 2009
Date

RULES FOR THE USE OF DISSERTATIONS

Unpublished dissertation submitted for the Doctor’s degree and deposited in the University of Kentucky Library are as a rule open for inspection, but are to be used only with due regard to the rights of the authors. Bibliographical references may be noted, but quotations or summaries of parts may be published only with the permission of the author, and with the usual scholarly acknowledgements.

Extensive copying or publication of the dissertation in whole or in part also requires the consent of the Dean of the Graduate School of the University of Kentucky.

A library that borrows this dissertation for use by its patrons is expected to secure the signature of each user.

Name	Date

DISSERTATION

Wenqin Shen

The Graduate School

University of Kentucky

2009

NOVEL CATALYSTS FOR THE PRODUCTION OF CO- AND CO_2-FREE HYDROGEN AND CARBON NANOTUBES BY NON-OXIDATIVE DEHYDROGENATION OF HYDROCARBONS

DISSERTATION

A dissertation submitted in partial fulfillment of the
requirements for the degree of Doctor of Philosophy in the
College of Engineering
at the University of Kentucky

By
Wenqin Shen

Lexington, Kentucky

Director: Dr. Gerald P. Huffman, Professor of Chemical Engineering

Lexington, Kentucky

2009

DEDICATION

To

Ella S. Xing

ACKNOWLEDGEMENTS

First, I would like to express my deepest gratitude to my advisor, Dr. Gerald P. Huffman, who has given me encouragement, guidance and support for the past three years. I also want to thank Dr. Tate T. H. Tsang, Dr. M. Pinar Mengüc, Dr. Nerash Shah and Dr. Burtron H. Davis for serving as my dissertation committee and final examiner and providing valuable suggestions.

Special thanks go to my co-advisor, Dr. Frank E. Huggins, for all his help, guidance and friendship. I also want to thank all the members at the Consortium for Fossil Fuel Science for the dynamic working environment and all their sincere help including Dr. Nerash Shah, Nicholas Cprek, Judith C. Cromer, Kathy (Xuebei) Shi and Dr. Yuguo Wang.

Finally, I would like to thank my husband, Dr. Rong Xing, for his love and support throughout these years. Without him, I couldn’t be here. We are so happy and excited with the arrival of our beautiful daughter, Ella S. Xing during my Ph.D studies. I would also like to thank my mother, Chengxia Yu and my entire family for their support and encouragement.

This work was funded by the U.S. Department of Energy under contract DE-FC26-05NT42456.

Table of Content

List of Tables

List of Figures

List of Files

Chapter 1. Introduction

U.S. Energy policy is directed by the need for a secure energy supply and the desire for sustainable growth. With the development of Asia, especially the two most populated countries, China and India, energy consumption is growing very fast and oil prices have recently soared to over $140/barrel. Moreover, proven reserves for oil known today will be depleted within about 40 years [1]. Thus, alternative energy sources are required to reduce the dependency of economies and life-styles on oil. Hydrogen is envisioned as the energy of the future [2], as it provides solutions to growing concerns about energy supply while minimizing the environmental impact of economic and energy supply activities. Hydrogen is an ultra-clean energy carrier, because it produces no emissions by the consumer, except for water. Hydrogen can be extracted from diverse feedstocks including fossil fuels such as coal, natural gas and petroleum, biomass, and water by a variety of processes such as thermochemical processes, electrolysis, thermolysis, photoelectrochemical and photobiological processes. Nuclear power and renewable energy such as solar, wind, geothermal energy can all be used to produce hydrogen by water splitting.

Globally, hydrogen production is already a large and significant industry. Most of it is used primarily as a chemical rather than a fuel in ammonia production (50%), oil refining (37%), methanol (8%), and other chemical and metallurgical industries (4%) [3]. Currently, only 4% of hydrogen is produced from water by electrolysis while the rest is derived from natural gas (48%), oil (30%), coal-derived syngas or synfuels (18%) through thermochemical path due to security and cost issues of renewable and nuclear energy [4]. In the U.S.A., 95% of the hydrogen is produced by steam reforming of natural gas, followed by water gas shift reaction (WGSR) [5]. The steam reforming reaction (equation 1-1) is a highly endothermic reaction, which requires high reaction temperatures from 700°C to 1100°C. However, WGSR (equation 1-2) is exothermic, performing at high temperature (350-400°C) and low temperature (180-240°C) in series to minimize the amount of water.

$$CH_4 + H_2O \rightarrow CO + 3\ H_2 + 191.7\ kJ/mol \qquad (1\text{-}1)$$

$$CO + H_2O \rightarrow CO_2 + H_2\ -41.1\ kJ/mol \qquad (1\text{-}2)$$

There are other processes under extensive investigation for hydrogen production through thermochemical means such as methane partial oxidation (equation 1-3) [6, 7], autothermal reforming (combination of equation 1-1 and 1-3) [8, 9], dry reforming (equation 1-4) [10, 11], steam reforming of ethanol (equation 1-5), methanol, biodiesel derived from biomass [12, 13] and sorption enhanced reforming [14-16].

$$C\ H_4 + O_2 \rightarrow CO + 3\ H_2 - 35.7\ kJ/mol \qquad (1\text{-}3)$$

$$C\ H_4 + CO_2 \rightarrow 2CO + 2\ H_2 + 165\ kJ/mol \qquad (1\text{-}4)$$

$$C_2H_5OH + H_2O \rightarrow 2CO + 4\ H_2 + 347.4\ kJ/mol \qquad (1\text{-}5)$$

However, these processes require further bulky WGSR, followed by purification (methanation or preferential oxidation (PROX)) and separation process in order to obtain high purity hydrogen. Moreover, carbon in hydrocarbons is released in the form of CO_2, which is regarded as greenhouse gas. CO_2 capture and sequestration are big issues that need to be solved in order to satisfy the ever more demanding requirements of environmental impact, thus adding to the cost of these processes.

As the fuel of the future, hydrogen will be used in advanced energy generation devices such as hydrogen combustion turbines, engines and fuel cells. One of the most important applications of hydrogen is to fuel polymer electrolyte membrane (PEM) fuel cells. The PEM fuel cell has experienced tremendous attention in the past few years. It is expected to provide portable electrical power and be used in vehicles. Most major automobile manufacturers are developing fuel-cell concept cars. The purity of hydrogen used in PEM fuel cells is very demanding, <10 ppm CO, since CO is a poison for the catalysts used in PEM fuel cells. Further, CO_2 in the hydrgoen stream is also detrimental to the performance of the PEM fuel cell. Therefore, new methods for hydrogen production should be developed which can result in high purity hydrogen and minimize the formation of CO_x. One approach is the non-oxdiative dehydrogenation of hydrocarbons to solid carbon and CO_x-free hydrogen. The general reaction can be expressed as following equation:

$$C_xH_y \rightarrow xC + 0.5yH_2 \qquad (1\text{-}6)$$

A comprehensive review on this subject has been conducted by T. V. Choudhary et al. [17, 18]. In this reaction, one of the products is solid carbon, which deposits on the surface of the catalyst causing the catalyst to deactivate very quickly. Only under certain conditions can carbon deposited on the catalyst surface diffuse through catalyst particles and grow whisker carbon in the form of carbon nanotubes (CNTs) or carbon nanofibers (CNFs), thereby prolonging the life-time of the catalysts.

Non-oxidative dehydrogenation of hydrocarbons for CO_x-free hydrogen on Ni-supported catalysts has been extensively investigated [19-33]. Takenaka et al. [19] studied methane dehydrogenation into hydrogen and carbon over supported Ni catalysts. The results showed that Ni supported on SiO_2, TiO_2 and graphite was catalytically active with long life-times, whereas Ni supported over Al_2O_3, MgO, and MgO-SiO_2 were catalytically inactive. XRD and XANES characterization revealed that metallic Ni was the active phase for methane decomposition reaction, whereas unreduced Ni, as either unsupported nickel oxide or after formation of a Ni^{2+} compound by reaction with the support was catalytically inactive. The porosity of the catalyst support also played a significant role on catalytic activity and stability. The silica with no pore structure was found to enhance the catalytic activity and stability. Further investigation showed that Ni catalysts with particle size in the range from 60 to 100 nm were most effective for methane decomposition. A deactivated Ni/TiO_2 catalyst could be regenerated by gasification of deposited carbon with CO_2 at 923 K for at least 5 cycles [20, 21]. Guil-López et al. [22] prepared Ni-Mg-Al catalysts from hydrotalcite-like compounds for methane decomposition and the regeneration experiment was carried out in both CO_2 and O_2 atmosphere. It turned out that the stability of metallic Ni was the key factor for the regenerability, and the presence of Mg increased the thermal stability of Ni catalyst particles. Research conducted by

Bonura et al. [23] confirmed the “structure sensitive” character of Ni-based catalysts for consecutive methane decomposition-CO_2/O_2 regeneration and revealed that carbon encapsulation was responsible for catalyst deactivation. Choudhary et al. [24-26] claimed that trace amounts of CO were formed over silica, zeolite, SiO_2-Al_2O_3 supported Ni catalysts due to the reaction of carbonaceous species with hydroxyl group contained on the surface of the support, even though it was called a CO_x-free process. [24-26] Chen et al. [27] reported that doping suitable amount of Cu into Ni/Al_2O_3 was able to increase catalyst stability for methane decomposition. Hydrogen production via the catalytic decomposition of ethane and ethylene was also investigated by Chin [28] and Savva [29] over Ni based catalysts. In addition to hydrogen and carbon, methane was detected as a gaseous product at temperature above 500°C.

Fe-based catalysts have been extensively studied for the production of filamentous carbon at temperatures above 1000°C with the co-feed of hydrocarbon gas or CO plus H_2. The presence of H_2 is believed to suppress the formation of encapsulated carbon, thus, elongating iron catalyst life-times. Literature references on Fe-based catalysts for hydrogen production via decomposition of undilute methane at moderate temperature (600-900°C) are relatively rare due to the fact that Fe-based catalysts are more prone to deactivation. But Fe-based catalysts can be used at higher temperatures than Ni-based catalysts, which are usually used at temperatures below 600°C. Hydrocarbon decomposition is an endothermic reaction and therefore a higher reaction temperature is desired for a high conversion. Thus, it is significant to develop Fe-based catalysts for this reaction. Konieczny et al. [34] used Fe-based catalysts prepared in-situ by reduction of magnetite either in CH_4 or H_2 for dilute methane decomposition (5% in N_2). 98% methane conversion was achieved and the reaction was able to last for 75 h without deactivation by using 2 g of catalyst at 800°C with an inlet gas flow of 5 mL/min. Whisker carbon was produced as a by-product. However, the operating conditions are so far removed from desired industrial conditions. Takenaka et al. [21] reported methane decomposition to hydrogen and carbon at

800°C over Fe_2O_3/Al_2O_3 and Fe_2O_3/SiO_2. No pre-reduction period was used. Fe_2O_3 crystallites with particle size less than 30 nm were transformed to α-Fe and Fe_3C, while particles larger than 30 nm were transformed to austenite after contact with methane at 800°C. Carbon yield over Fe_2O_3/Al_2O_3 was 105 mol C/mol Fe, 3 times more than that over Fe_2O_3/SiO_2. Ermakova et al. [35, 36] investigated α-Fe based catalysts to produce hydrogen and filamentous carbon from high-purity methane over the temperature range of 650-800°C. It was found that the optimal operating temperature was 680°C, where, iron carbide was at the point of transition from a stable to metastable state. It was believed that both α-Fe and carbide phases were important for oriented growth of carbon. Coarse iron particles were not active in methane stream. The addition of hard-to-reduce oxides, such as SiO_2, TiO_2, ZrO_2 and Al_2O_3, to the iron catalyst as texture promoters could either inhibit or promote the reaction. The maximum carbon yield of 45 g carbon/g Fe was achieved with the addition of 15 wt.% SiO_2. Fe, Fe-Co and Fe-Ni catalysts supported on alumina prepared by coprecipitation were studied for methane decomposition at moderate temperatures (600-650°C). The addition of 5-10 wt.% of a second metal like Co or Ni to Fe/Al_2O_3 catalyst significantly improved the catalytic performance for methane decomposition due to the formation of specific alloy particles and the optimum particle size distribution. The best catalyst contained 50-60 wt.% Fe, 5-10 wt.% Co (or Ni) and the balance Al_2O_3 with carbon capacity as high as 145 g carbon/g catalyst. At 625°C, a Fe-Ni bimetallic catalyst on alumina showed much higher methane conversion than a $Fe\text{-}Co/Al_2O_3$ catalyst, initially 24% versus 16%. Carbon was formed as multi-walled CNTs. Catalysts deactivation may be caused by carbon encapsulation, or by irreversible phase changes during reaction or by fragmentation of catalyst particles [37, 38].

Metals or metal alloys other than Ni and Fe have also been used for investigations of hydrogen production by hydrocarbon catalytic decomposition. Co-based catalysts usually operate over the same temperature range as Ni-based catalysts, but with less efficiency. Co/MgO, Co/SiO_2, Co/Al_2O_3 were prepared and tested by Avdeeva et al.

[39]. Among all the prepared catalysts, 50 wt.% Co on Al_2O_3 showed the highest methane conversion (12%) and 75 wt.% Co on Al_2O_3 had the longest life-time and highest carbon capacity (63 g C/g Co) (7% methane conversion) at 500°C with space velocity 45 $dm^3 \cdot g\ catalyst^{-1} \cdot h^{-1}$. Methane conversion increased with increasing reaction temperature, but life-time and carbon capacity decreased. It was reported that copper can enhance the ability for carbon growth and allowed operations at temperatures above 600°C when introduced into Ni, forming Ni-Cu bimetallic catalysts. But, the presence of Cu promoted the formation of carbon grains rather than filamentous carbon [27]. Monometallic Cu/Al_2O_3 catalysts with different Cu loading for methane decomposition over a temperature range of 800-1000°C were also studied by Ammendola et al. [40] in a fluidized-bed. The identified active phase was cupper aluminum spinel on surface. Copper oxide showed very poor activity. By using a Cu-based catalyst, CO was detectable in the effluent, even though the catalysts were pre-reduced. Precious metal Pd-based catalysts on alumina have also been investigated for methane decomposition at temperatures above 700°C to achieve CO_x-free and highly concentrated hydrogen. Pd-based bimetallic catalysts containing Ni, Co, Rh or Fe (molar ratio, 1:1) showed higher catalytic activity and longer life-times compared with any of monometallic catalysts. Pd-Ni/Al_2O_3 and Pd-Co/Al_2O_3 were especially efficient catalysts. 94 vol.% of hydrogen could be produced by Pd-Co/Al_2O_3 at 850°C. TEM study revealed that formation of Pd-Co alloy particles enhanced the growth of CNTs from one facet on Co or Pd metal particles to several facets, thereby improving the performance of the alloy catalysts [40].

Carbon products have also been used as catalysts for methane decomposition to produce CO_x-free hydrogen. One obvious advantage of carbon catalysts is that because the carbon by-products deposit directly on the carbon catalysts, no further purification process is required to obain relatively pure carbon product. Dunker et al. [41] employed a fluidized-bed for methane decomposition by using three types of carbon black at temperatures of 810-980°C. The hydrogen yield decreased rapidly during the first 50 min, kept constant for about 1000 min, and then decreased fast again. Under the optimum conditions, the decomposition of methane produced more than 40 vol.% hydrogen in the effluent. The carbon by-product remained on the reactor bed and had little graphitic character. At the temperature above 930°C, the formation of polycyclic aromatic hydrocarbons (PAHs) became significant. Bai et al. [42] found that the catalytic reaction of methane decomposition occurred mainly inside the micropores of activated carbon. Muradov et al. [43, 44] tested several activated carbons, carbon blacks and natural graphites as catalysts for methane and propane decomposition at 850°C. It was found that the catalytic activity was determined mostly by the surface and structure properties of the carbon catalysts. The catalytic activity was in the order amorphous carbon > turbostratic carbon > graphite and proportional to the external surface area. Compared with activated carbons, carbon blacks had higher methane decomposition rates due to higher external surface areas. Catalyst deactivation was due to blocking of the pore mouth by deposited carbon from hydrocarbon decomposition. Different types of reactors, including tubular, fluid wall, spouted and fluidized-bed, were tested and evaluated for their usefulness for hydrocarbon decomposition. It was concluded that the fluidized-bed reactor was the most promising reactor for this process. However, carbon deposited onto the surface of carbon catalyst was poorly crystalline. It was difficult to find applications for the carbon by-products and the efficiency of the carbon catalysts was relatively low, only around 20% carbon product on the carbon catalyst. Thus, the application of this process is limited.

Despite the extensive research work conducted, the major barrier for the application of non-oxidative dehydrogenation of hydrocarbons remains the short life-time of catalysts at temperatures above 600°C in order to obtain higher conversion. Some catalysts were reported regenerable for several cycles by exposure to oxidants such as CO_2, air and steam. However, during the regeneration process, CO_x was produced in significant amounts, comparable to that from the reforming process. Carbon sequestration is again a problem that needs to be solved cost efficiently. Therefore, novel catalysts are required that have high activity, long life-times, and, equally important, useful carbon by-products.

Our group at the University of Kentucky has been developing catalysts for CO_x-free hydrogen production from non-oxidative dehydrogenation of hydrocarbons. In prior work, alumina supported nanoscale binary Fe-M (M=Pd, Mo, or Ni) catalysts (5 wt.% Fe-M, supported on γ-Al_2O_3) were prepared for the catalytic decomposition of undiluted methane to produce H_2 and carbon product [45]. The result showed that all binary Fe-M catalysts exhibited significantly higher activity than monometallic Fe or any of the secondary metals (Pd, Mo and Ni) on their own. At the reaction temperature of approximately 700-800ºC and space velocities of $600 mLg^{-1}h^{-1}$, the effluent contained over 80 vol. % of H_2, with unreacted methane as balance. The solid product, carbon, was in the form of multi-walled CNTs. At temperatures higher than 900ºC, carbon deposited on the surface of catalyst was in the form of amorphous carbon, carbon flakes and carbon fiber, which deactivated the catalysts rather quickly. The same catalysts were also applied to the decomposition of ethane, propane and cyclohexane [46, 47]. Above 475ºC, hydrogen and methane were the only gas products for ethane and propane decomposition. For cyclohexane, the same gas products were obtained at temperatures above 500ºC. The texture of CNTs was dependent on the reaction temperature. Taking ethane and propane decomposition as examples, CNTs were predominantly in the form of multi-walled CNTs with parallel walls formed by the concentric graphene sheets at temperatures above 600ºC. Carbon nanotubes with capped and truncated stack-cone structure (SCNTs) were produced at temperatures ≤ ~500ºC. At 625ºC, decomposition of cyclohexane produced a mixture of these two types of CNTs structures. The characterization of these alumina supported bimetallic catalysts by X-ray absorption fine structure (XAFS), Mössbauer spectroscopy and X-ray diffraction (XRD) showed that all three binary metal catalysts had similar structures. The formation of hercynite ($FeAl_2O_4$) was believed to enhance the activity of the catalysts by binding the catalyst particles to the alumina surface, preventing demetallization at high reaction temperatures [48, 49]. However, the CNTs produced were very difficult to clean due to the limited solubility of alumina and the strong bonding of the CNTs to the support caused by the formation of hercynite during the reaction. Therefore, one of our goals of this thesis research was to develop a new catalyst support and catalysts for non-oxidative dehydrogenation of hydrocarbons to produce easily purified CNTs and CO_x-free hydrogen.

In chapter 3, a synthetic catalyst support, Mg(Al)O, prepared from calcination of a Mg-Al-hydrotalcite with a Mg to Al ratio of 5, is used as the catalyst support for ethane dehydrogenation. Monometallic Ni and bimetallic FeNi nanoscale catalysts on this Mg(Al)O support prepared by incipient wetness method with total metal loadings of 5 wt.% were studied and compared. The dehydrogenation of undiluted ethane was evaluated over these two catalysts at the temperatures of 500, 650, and 700ºC. The morphology of the carbon by-product was seen to depend on both catalyst composition and reaction temperature. The produced CNTs were easily purified by a one-step dilute nitric acid treatment. The catalysts and CNTs were characterized using spectroscopic and XRD methods and the reaction mechanism was revealed.

In chapter 4, a novel approach, nanoparticle impregnation, is described that was employed to develop FeNi nanoparticle catalysts supported on Mg(Al)O for methane dehydrogenation. The performance of these FeNi nanoparticle catalysts for methane dehydrogenation was significantly improved compared with that of the FeNi catalyst prepared by the conventional incipient wetness method. The carbon product was μm scale long multi-walled CNTs with relatively uniform diameter. A comprehensive investigation of this novel catalyst is reported. In chapter 5, the preparation of monodispersed Fe nanoparticles with particle sizes of 5 nm, 10 nm and 15 nm is described. These catalysts were loaded onto the Mg(Al)O support for investigation of catalyst particle size effects on methane dehydrogenation. It turned out that 10 nm was the optimum particle size, exhibiting both longer life-times and higher activity. The explanation of this size effect is investigated and discussed. A brief summary and future work are given in chapter 6.

Different characterization techniques were used in this thesis to understand the behavior of catalysts and reveal the catalytic mechanism. Transmission electron microscopy (TEM), both high resolution TEM (HRTEM) and scanning TEM (STEM), was used to image and determine the structure of the monodisperse nanoparticle catalysts and the CNTs. Energy dispersive x-ray (EDX) elemental mapping was employed to observe Fe and Ni distribution on reduced FeNi/Mg(Al)O catalysts. Other common techniques such as x-ray diffraction (XRD), thermal gravimetric analysis (TGA), BET surface area, temperature programmed reduction (TPR), and so on were also used. In particular, Mössbauer spectroscopy and x-ray absorption for fine structure (XAFS) spectroscopy were used in this work to identify catalytic active phases, analyze catalyst compositions and crystal structures, and discern catalyst structural details at the atomic scale. A brief introduction to Mössbauer spectroscopic and X-ray absorption fine structure spectroscopic techniques has been given in chapter 2.

Chapter 2. A Brief Introduction to Mössbauer and X-ray Absorption Fine Structure Spectroscopic Techniques

2.1 Mössbauer Spectroscopy

2.1.1. Introduction

Mössbauer spectroscopy, as a nuclear technique, was first developed in 1958. It analyzes the resonant absorption of γ-rays from nuclear transitions between the ground state and an excited state and provides information on oxidation states, magnetic field, lattice symmetry and lattice vibrations. Mössbauer spectroscopy has been applied to characterize solid catalysts since 1971. It is a powerful method in catalysis that can be used to identify catalyst phases, determine chemical states, and investigate magnetic relaxation phenomena in nanoscale particles, from which information concerning about particle size distribution, surface chemisorption, and catalyst dispersion can be obtained. Compared with electron microscopy or photoelectron spectroscopy, Mössbauer spectroscopy is a relatively inexpensive method. It can also be easily applied in-situ to character the catalysts under working conditions. However, only a limited number of elements can be studied by Mössbauer spectroscopy such as ^{57}Fe, ^{119}Sn, ^{57}Co (in emission mode), ^{121}Sb, ^{197}Au, ^{99}Ru, ^{193}Ir, ^{195}Pt, ^{151}En and so on. Comprehensive literature reviews about Mössbauer spectroscopy in recent years can be found elsewhere [50-55]. In this study, Mössbauer spectroscopy has been used to investigate iron-containing catalysts supported on Mg(Al)O and to identify the active and inactive phases for the catalytic hydrocarbon dehydrogenation reaction.

2.1.2 The Mössbauer Effect

The Mössbauer effect is named after Rudolf L. Mössbauer, who discovered it in 1957, and refers to recoilless nuclear resonance absorption of γ-ray by atoms bound in a solid [52]. It can be simply described as the fraction of the photons emitted by the source nucleus that will be absorbed by the nucleus in an absorber of same type with recoil energy of the photon emission and absorption significantly smaller than the energy of the lattice vibrations [55].

The intensity of the Mössbauer effect depends on the recoilless factor (*f*), which is defined as:

$$f = e^{-k_r^2 < x^2 >} \tag{2-1}$$

It can be rewritten in the Debye model:

$$f = \exp[-\frac{3E_R}{2k\theta_D}(1 + 4\frac{T^2}{\theta_D^2})\int_0^{\frac{\theta_D}{T}}\frac{xdx}{e^x - 1}] \tag{2-2}$$

Where f is the recoilless factor, k_r is the wave number of the γ-ray, $< x^2 >$ is the mean squares of displacement of atoms from their average position due to lattice vibrations, E_R is the recoil energy of the nucleus upon emission of γ-ray ($E_R = E_r^2/2Mc^2$, where E_r is the energy of γ-ray; M is the mass of the nucleus; c is the velocity of light), k is Boltzmann's constant, θ_D is the Debye temperature, and T is the Kelvin temperature [55].

Equations 2-1 and 2-2 give insights on the limitations of the Mössbauer technique in terms of the mass of Mössbauer isotopes, the strength of chemical bonds and the temperature, since θ_D should not be too small (non-rigid lattice), T not too high, M not too small (>40) [50, 51]. Another constraint of the Mössbauer effect is the choice of γ-ray source, in which the nucleus should have a long lifetime decay to the excited state that we want to study and follow by an instantaneously energy transition to generate γ-ray [51, 55]. ^{57}Co is most commonly used as a source for ^{57}Fe isotope. The half-life of ^{57}Co decaying to ^{57}Fe is 270 days and the energy of the γ-ray generated by following fast decay is 14.4 keV, which is used for Fe Mössbauer spectroscopy.

2.1.3 Mössbauer Spectroscopy

The nucleus interacts with its surroundings through hyperfine interactions. The energy level between the source and absorber differs slightly due to different local environments. In order to observe the Mössbauer effect, the energy level between source and absorber must be the same. The Mössbauer spectrometer thereby utilizes the Doppler effect to compensate for the variation of the incident energy and the energy level of the absorber, which can be expressed by the following equation:

$$E(v) = E_o(1 \pm \frac{v}{c}) \tag{2-3}$$

Where $E(v)$ is the incident energy, v is the Doppler velocity of source operated by a constant acceleration oscillator, E_o is the energy difference between ground state and excited state of nucleus, and c is the velocity of light [55].

In a typical Mössbauer Absorption Spectrometer (MAS), a solid sample is exposed to a beam of γ-ray and a detector measures the intensity of the beam that is transmitted through the sample. The schematic illustration of MAS and Doppler Velocity is shown in figure 2.1. For convenience, the Mössbauer spectrum records the intensity of the transmitted γ-ray as a function of the Doppler velocity v instead of the corresponding energy. The Doppler velocity for ^{57}Fe is in the range of ±10 mm/s [50].

Generally, a Mössbauer spectrometer measures three types of hyperfine interactions between the nucleus and the surrounding electrons [50, 51, 55]. The first and the simplest interaction is the electric monopole interaction between the positively charged nucleus and the negatively charged s-electrons. It shifts since the size of the nucleus in the excited state differs from that in ground state, leading to the variation of s-electron density at the probe nucleus. This measured shift is called isomer shift (IS) with unit of mm/s, which provides information on the chemical state of the absorber. In the case of ^{57}Fe, the IS values are given with respect to the peak position of α-Fe. The isomer shift is also temperature dependent due to the second order Doppler Shift.

The second interaction is the electric quadrupole interaction between the electric quadrupole moment of the nucleus and the local electric field gradient. In the case of ^{57}Fe, when the nucleus is excited to the 14.4 eV level, it changes shape from spherical to ellipsoid, thus orientating itself in two ways in an electric field with slightly different energies. The Mössbauer spectrum splits into a doublet in consequence of the nucleus quadrupole splitting (QS). QS is equal to the velocity (V) difference of the two splitting peaks and the IS is measured at the center of the two peaks.

$$QS = V_2 - V_1 \tag{2-4}$$

$$IS = (V_1 + V_2)/2 \qquad (2\text{-}5)$$

The third interaction arises from the interaction between the nuclear magnetic dipole moment and the magnetic field H at the nucleus. In the case of ^{57}Fe, the magnetic field H consists of five contributions including s-electron spin polarization, unpaired 3-d orbital electron parallel spin, the dipole interaction related to the local electron spin moments on the probe site, the field resulting from the magnetization of the sample particle, and the external magnetic field applied to the sample. The magnetic hyperfine splitting (H_0) gives six peaks called a sextet in an iron Mössbauer spectrum. Again, the IS is measured at the center of the six lines. H_0 with unit of kGauss is proportional to the difference between the position of line 1 and line 6 of the spectrum.

$$IS = (V_1 + V_6)/2 \qquad (2\text{-}6)$$

$$H_0 \propto (V_6 - V_1) \qquad (2\text{-}7)$$

All hyperfine interactions can actually occur simultaneously, thus leading to more complicated spectra. For example, the shift of the spectrum occurs depends a lot on the relatively strength of the magnetic interaction and the electric quadrupole interaction. Mössbauer parameters are also temperature-sensitive, and this characteristic is sometimes exploited by using lower temperatures to improve peak resolution and induce interesting magnetic phenomena.

The techniques for processing Mössbauer data are complex and variable. In this study, the spectra were analyzed by least-squares fitting using a computer routine that fits individual Fe components as single peaks, quadrupole doublets, or magnetic sextets based on a lorentzian line profile.

2.2 X-ray Absorption Fine Structure Spectroscopy

2.2.1 Introduction

X-ray Absorption Fine Structure Spectroscopy (XAFS) uses the x-ray photoelectric effect and the wave nature of the electron to probe materials at the atomic scale, providing information of local atomic coordination and chemical/oxidation state. This technique was developed in the 1970s. Practically, it can be applied to any element with atomic number (Z) larger than 2 and requires minimal sample amount. Unlike x-ray diffraction techniques applied to crystalline samples, XAFS does not require long range order, thus working equally well in amorphous materials, liquids, (poly) crystalline solids, and gases. XAFS is the modulation of the x-ray absorption coefficient at energies near and above an x-ray absorption edge. The spectrum is typically divided into two regimes: x-ray absorption near-edge spectroscopy (XANES) and extended x-ray absorption fine structure spectroscopy (EXAFS). XANES is strongly sensitive to the oxidation state and coordination chemistry, while the EXAFS is used to determine the distance, coordination number and species of the neighbors of the absorbing atom. XAFS measurements need intense and energy-tunable source of x-rays, thereby, are usually conducted at synchrotron laboratory [55-59].

2.2.2 Simple Theoretical Description

X-rays with energies ranging from 120 eV to 200 keV are absorbed by all matter through the photo-electric effect. If the bonding energy of a core level electron (E_0) is less than the energy of an incident x-ray (E), the electron may be removed from its quantum level. In this case, the x-ray is absorbed and any energy in excess of the electronic binding energy is given to a photoelectron ($E-E_0$) that is ejected from the atom, thus leaving the absorbing atom in an excited state with an empty electronic level (a core hole). The excited core hole will eventually be filled with higher level core electrons, thereby a fluorescent x-ray or Auger electron is emitted from the absorbing atom. Once the x-ray energy is large enough to excite a core level to the continuum, there is a sharp increase in absorption. This is the so-called absorption edge, which occurs at specific energies for each element. When the absorbing atom is not isolated, the emitted photo-electron can be scattered from neighboring atoms by single path scattering or multiple path scattering, depending on local coordination environment of the absorbing atom and return back to the absorbing atom, interfering with itself [57].

As mentioned above, XAFS is the technique to measure the energy dependence of the x-ray absorption coefficient $\mu(E)$ near and above the absorption edge of a selected element. The extended spectrum, EXAFS, measures the energy dependent oscillations in $\mu(E)$ and can be expressed as:

$$\chi(E) = \frac{\mu(E)-\mu_0(E)}{\Delta\mu_0(E_0)} \qquad (2\text{-}8)$$

Where $\mu_0(E)$ is a smooth background function representing the absorption of an isolated atom and $\Delta\mu_0$ is the edge step in the absorption at the threshold energy E_0. As EXAFS is an interference effect, depending on the wave nature of the photo-electron, it is common to express EXAFS in k space by converting x-ray energy to k, photo-electron wavenumber. Practically, $\chi(k)$ is often weighted by k^2 or k^3 to amplify oscillations at higher k.

EXAFS can be modeled by the EXAFS equation:

$$\chi(k) = \sum_j \frac{N_j S_0^2 f_j(k) e^{-2R_j/\lambda(k)} e^{-2k^2\sigma_j^2}}{kR_j^2} \sin\left[2kR_j + \delta_j(k)\right] \qquad (2\text{-}9)$$

Where $f(k)$ and $\delta(k)$ are scattering amplitude and phase-shift, S_0^2 is the amplitude reduction factor related to the relaxation effects in the emitting atom, λ is the inelastic mean free-path of the photo-electron, N is the coordination number of the neighboring atom, R is the distance to the neighboring atom, σ^2 is the mean-square disorder of neighbor distance, j is the lablel of the coordination shells around the electron-emitting atom, the sum is over shells of similar neighboring atoms. The EXAFS equation allows us to determine N, R and σ^2 if the scattering amplitude $f(k)$ and phase-shift $\delta(k)$ are known and also to determine the species of neighboring atom due to the fact that $f(k)$ and $\delta(k)$ are atomic number sensitive. The $f(k)$ and $\delta(k)$ can be calculated by using computer program FEFF.

The near edge spectra, XANES, are typically within 100 eV of absorption edge. Unlike the EXAFS, to extract physical and chemical interpretation of all spectral features is still difficult to do accurately, precisely and reliably as there is still no simple equation for XANES. However, XANES can be done at lower concentrations and less-than-perfect sample conditions because it has a much stronger signal than

EXAFS. It can be applied qualitatively in terms of coordination chemistry, molecular orbitals, band-structure and multiple-scattering. For many systems, the XANES analysis can be as simple as making linear combination of “known” spectra to get compositional fraction of these components [57, 58].

2.2.3 Experimental

The energy dependence of the absorption coefficient$\mu(E)$ can be measured either in transmission mode or in fluorescence mode as illustrated in figure 2.2. In the transmission mode, the absorption is measured directly by measuring what is transmitted through the sample. Where,

$$I = I_0 e^{-\mu(E)t} \tag{2-10}$$

$$\mu(E)t = -\ln(I/I_0) \tag{2-11}$$

In fluorescence mode, the fluorescence x-ray is measured with:

$$\mu(E) \propto I_f/I_0 \tag{2-12}$$

Where I_0 is the intensity of incident x-ray beam; I is the intensity of transmitted x-ray beam; t is the thickness of the measured material; $\mu(E)$ is x-ray absorption coefficient depending on x-ray energy E, atomic number Z, density and atomic mass of measured material. Due to self-absorption, the XAFS in fluorescence is limited to use with the dilute samples and very thin samples. [57].

2.2.4 Data Analysis

In both transmission and fluorescence modes, the data processing is essentially the same, including data reduction, pre-edge subtraction, E_0 determination and normalization, post-edge background subtraction, Fourier transforms and reverse Fourier transforms [60].

In this study, the analysis of XAFS spectra followed the usual steps and was carried out by using SIXPack (Sam’s interface for XAS package) software package for personal computer, which builds on Matt Newville's IFEFFIT engine [60-63]. First, the collected raw intensity data are loaded, converted to $\mu(E)$ and averaged in SamView Menu option. The energy E_0 is calibrated by first order derivative of $\mu(E)$

function and applying energy shift to data. Secondly, in the background subtraction dialog, the saved average data in $\mu(E)$ are input and edited by deglitching, if necessary. And then, the pre-edge normalization and post-edge normalization are applied to get rid of any instrumental background slope and absorption from other edges, and the spectra are normalized to absorption step of unity. The normalized $\mu(E)$ is then convert to k^2 or k^3 weighted $\chi(k)$ in the typical range of 2-15 $Å^{-1}$. The R space can be obtained by Fourier transforms of $\chi(k)$ by applying different FT window, for example, Kaiser-Bessel window, in the typical range of 0-6 Å. $\mu(E)$, $\chi(k)$ and R functions are saved individually as ASCII files for later data analysis [63].

The least squares fitting module of SIXPack is used to fit experimental data mainly in XANES as linear combination of standard reference compounds in order to extract component information of absorbing sample. The primary inputs are the data file to be fit and the set of reference spectra to be considered in the fit. Various fitting constraints are applied such as energy limits, k weighting, non-negative fitting, summary component to one, allow data E to floating and so on. The fitting results are evaluated by Chi squared or reduced Chi squared [63].

FEFF EXAFS fitting acts as an interface to IFEFFIT, which performs fits of FEFF derived scattering amplitude $f(k)$ and phase-shift $\delta(k)$ to experiment data. The fits can be done by simple shell-by-shell models, or extremely complicated and constrained structural models by choosing “templates” options in this dialog. The FEFF input file “feff.inp” containing crystallgraphic coordination can be generated by ATOM or Web ATOM program by Bruce Ravel [64]. After running FEFF 6 built in IFEFFIT, “feefnnnn.dat” files are generated and stored individually, representing different scattering paths. The fitting is usually operated in R-space because working in R-space allows us to selectively ignore higher coordination shells. In order to set up a fit, the loading of the main data file $\chi(k)$, definition of paths and variables have to be done properly. The common fitting parameter including:

S_0^2 —the amplitude reduction parameter;

E_0 —the energy shift in the Fermi level between experiment and theory;

ΔR —the difference between the fitted radial distance and the one defined by the FEFF file;

σ^2 —the disorder parameter, commonly used as Debye-Waller factor.

The fitting may be evaluated by statistic parameters such as chi squared, reduced chi squared and R factor and also the physical meaning of the above fitting parameters. The data and fits can be plotted in k space, R-space and q-space (back-transformed k-space by reverse Fourier transforms) and saved, respectively [63].

More details of the fitting can be found in the documentation files for SixPACK software.

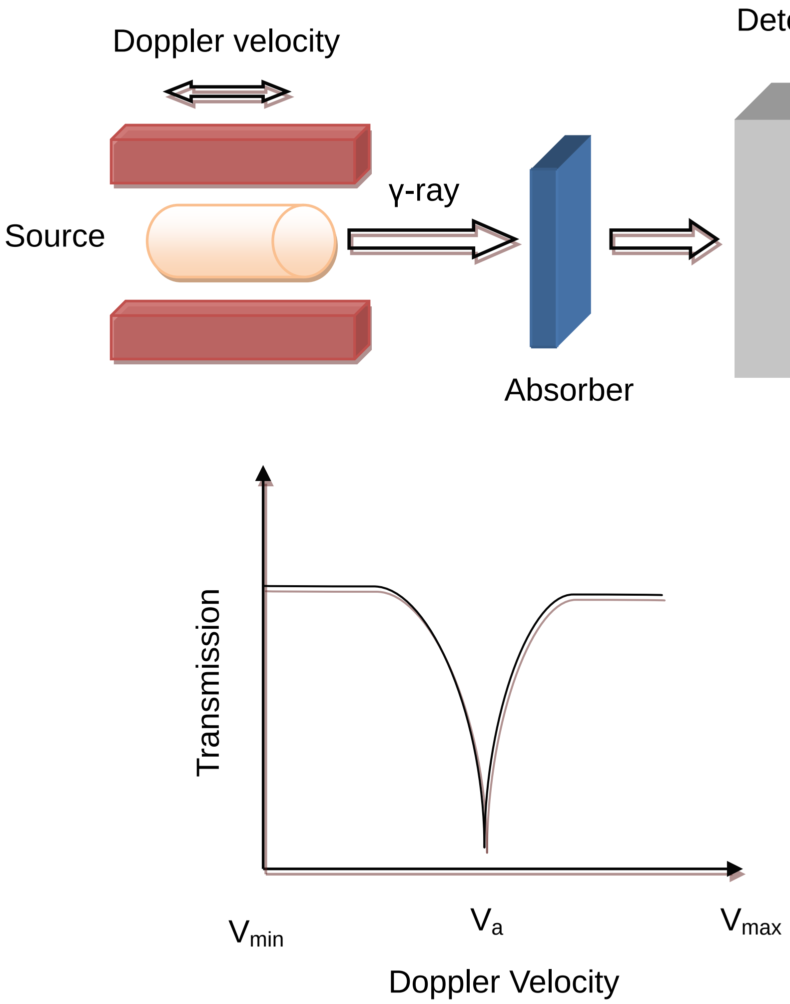

Figure 2.1. Schematic illustration of a Mössbauer Absorption Spectrometer (MAS). The energy of the source radiation is modulated by using the Doppler effect in order to cover all possible transitions in the nucleus of absorber [55].

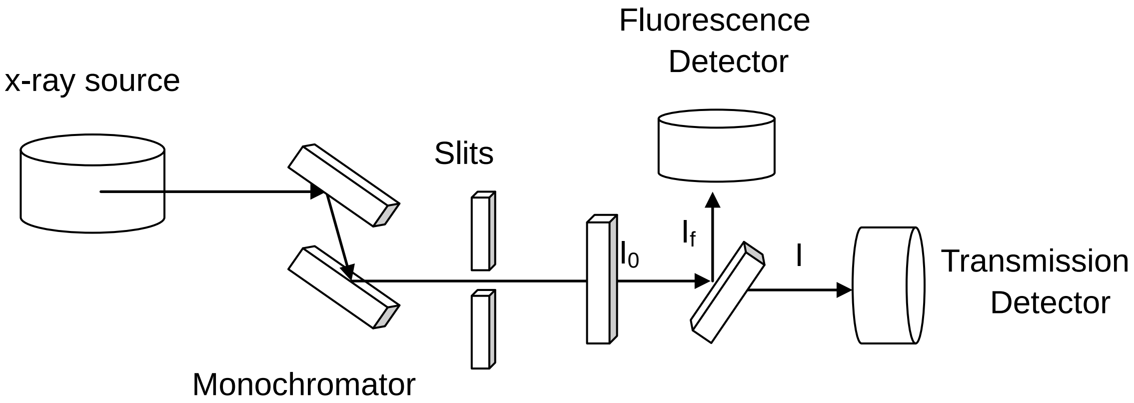

Figure 2.2. Schematic illustration of synchrotron x-ray absorption spectroscopy in both fluorescence mode and transmission mode [57].

Chapter 3. Catalytic Non-oxidative Dehydrogenation of Ethane over FeNi and Ni Catalysts Supported on Mg(Al)O to Produce Hydrogen and Easily Purified Carbon Nanotubes

This chapter is based on work published as: W. Shen, Y. Wang, X. Shi, N. Shah, F. Huggins, G.P. Huffman “Catalytic non-oxidative dehydrogenation of ethane over Fe-Ni and Ni catalysts supported on Mg(Al)O to produce pure hydrogen and easily purified carbon nanotubes”, *Energy & Fuels*, 2007, 21(6), 3520-3529. Copyright 2007 American Chemical Society.

3.1 Introduction

An energy economy based on hydrogen could alleviate growing concerns about energy supply, air pollution, and greenhouse gas emissions. Currently, the most widely used method of hydrogen production is steam reforming or partial oxidation of fossil fuels, particularly natural gas, followed by the water gas shift reaction (WGS) and separation and purification steps. However, the hydrogen purity requirement for use in polymer electrolyte membrane (PEM) fuel cells is demanding (<10 ppm CO), since CO is a poison for the catalysts used in PEM fuel cells. Additionally, the steam reforming – WGS process produces significant amounts of CO_2, a gas believed to contribute to global warming. Therefore, direct, non-oxidative decomposition of hydrocarbons into hydrogen and carbon is an attractive alternative method of producing hydrogen that is free of CO and CO_2. Moreover, the process is a simple one-step reaction:

$$C_xH_y \rightarrow xC+(y/2)H_2 \tag{3-1}$$

Previous work by our research group has shown that binary Fe-M (M = Ni, Mo, or Pd) catalysts prepared by incipient wetness or co-precipitation on γ-alumina supports have excellent activity for dehydrogenation of methane, ethane, propane and cyclohexane [45, 46, 65]. Results from Mössbauer and XAFS spectroscopy suggest that the active phase is an austenitic Fe-M-C alloy that is bound to the alumina support by hercynite ($FeAl_2O_4$) [48, 49]. The carbon produced by the reaction was present as potentially valuable carbon nanotubes (CNTs), which were in the form of multi-walled nanotubes (MWNTs) in the most active temperature range. However, the CNTs were very difficult to clean because of the limited solubility of alumina and the strong binding of the nanotubes to the support caused by the formation of $FeAl_2O_4$ during the reaction.

To obtain high quality CNTs by the catalytic chemical vapor deposition (CCVD) method requires almost complete removal of the catalyst particles and support. A number of different approaches and purification methods have been developed [15, 66-70]. Conventional catalyst supports, such as alumina, silica, and zeolite, are excellent supports for CNTs production by CCVD. However, a multi-step purification process is required, which leads to a low CNTs yield and may even damage the structure of the CNTs. Recently, several investigations have used basic catalyst supports to produce CNTs by CCVD because of the facile dissolution of the support in dilute acid. Flahaut et al. [71] used a $Mg_{0.9}Co_{0.1}O$ solid solution prepared by combustion synthesis to crack methane in a hydrogen-methane mixture (18 vol. % methane) at a temperature of 1000ºC. The solid product was treated with an HCl solution and the MgO was completely dissolved. There was still some Co left as Co particles embedded within the CNTs. Couteau et al. [72]used $CaCO_3$ as catalyst support for Fe and Co monometallic and bimetallic catalysts for acetylene decomposition at 720°C. The metallic particles and support could be dissolved in dilute acid (30% HNO3 or HCl) in one step. The purified MWNTs were found to be an excellent catalyst support for Fischer-Tropsch (FT) synthesis [73].

Here, a basic catalyst support, Mg(Al)O, was prepared by calcination of a synthetic hydrotalcite (HTL) precursor. The product of the calcination has pronounced basic character, high surface area, and good stability towards heat and steam and was easily dissolved in dilute nitric acid. Monometallic Ni and bimetallic FeNi (molar ratio of Fe/Ni = 65/35) nanoscale catalysts were deposited on this support by the incipient wetness method and used for decomposition of undiluted ethane, providing both a high hydrogen yield and an easily purified CNTs by-product.

3. 2 Experimental Section

3.2.1 Catalyst Preparation

$Mg_{(1-x)}Al_x$ HTL with a Mg/Al molar ratio of 5 was prepared by coprecipitation at constant pH and temperature [74]. A flow of magnesium nitrate and aluminum nitrate solution with a total cation concentration of 1 M and a flow of solution with 10 mol. % excess of KOH and K_2CO_3 (molar ratio of CO_3^{2-} to Al^{3+} equal to 0.5) were pumped into a matrix solution using syringe pumps. The pH value of the matrix solution was controlled to between 8.5 and 9.5 by tuning the syringe pump flow rates. The reaction temperature was controlled at 70°C. The end point pH was adjusted to 9.5 by adding excess KOH. After reaction, the precipitate was aged overnight at room temperature, then filtered and re-dispersed in hot deionized water for several cycles to completely wash off any adsorbed K^+ (pH = 7), and finally dried at 100ºC for 24 h. The dried precipitate was then calcined in air at 550ºC for 5 h, cooled to room temperature, and ground into a fine powder (<100 mesh), which was labeled as Mg(Al)O catalyst support.

The catalysts were prepared by incipient wetness. The catalyst precursors, $Fe(NO_3)_3•9H_2O$ and $Ni(NO_3)_2•6H_2O$, based on the desired Fe/Ni ratio (65/35) and total metal loading of 5 wt. %, were dissolved in deionized water, then mixed with the dry Mg(Al)O powder, and dried in an oven at 80ºC. This was repeated three or four times with a volume of the added solution close to the total pore volume of the support powder each time until the catalyst precursor solution was totally absorbed. The resulting material was then dried in an oven overnight at 80ºC, calcined in air at 550ºC for 5 h, cooled to room temperature, and stored in a dry place.

3.2.2 Ethane Dehydrogenation Reaction

The dehydrogenation reaction was performed in a fixed-bed plug-flow reactor described in detail with a schematic diagram elsewhere [65]. Briefly, the reaction chamber was a quartz tube with an inner diameter of 22.5 mm. One gram of catalyst powder was loaded at the center of the reactor and activated by reduction in hydrogen. The reduction was conducted by heating the furnace slowly at 2ºC/min up to 700ºC and maintaining this temperature under a hydrogen flow rate of 50 mL/min for 2 h. The decomposition reaction was conducted at 500, 650, and 700°C, with an ethane flow rate of 10 mL/min. The inlet gas flow was controlled by a mass flow controller, and the effluent was monitored by a bubble flow meter and analyzed by online gas chromatography (GC) with a thermal conductivity detector (TCD). The solid product was collected after reaction. The various gaseous products were quantified as volume percentages of the total gaseous effluent.

3.2.3 CNTs Purification

Nitric acid was used to remove the catalyst from the produced CNTs. The collected CNTs were purified at room temperature or under reflux in 6M HNO_3 solution for 2 h. The material was filtered and then thoroughly washed using deionized water to remove any adsorbed HNO_3. The purified CNTs were then dried in an oven at 80ºC overnight.

3.2.4 Catalyst Characterization

The N_2 adsorption-desorption isotherms were measured for the Mg(Al)O support, the catalysts in their as-prepared and reduced conditions at liquid nitrogen temperature on a Micromeretics TRISTAR 3000 instrument. Prior to the adsorption and desorption measurement, the samples were degassed overnight at 150°C with a N_2 purge. Powder X-ray diffraction was conducted on a Siemens 5000 diffractometer using Ni filtered Cu-Ka radiation and a scanning rate of 0.5° 2θ min^{-1}. The Mg(Al)O support grain size was calculated from the full width at half maximum (FWHM) of the principal peaks, using the Debye-Scherrer equation. The morphologies of the catalysts and the produced CNTs were characterized by transmission electron microscopy (TEM) using a JEOL 2010F instrument at a voltage of 200 kV. TEM samples were prepared by crushing the samples, dispersing them in acetone by ultrasonication for 15 minutes, loading a single drop of the suspension onto lacey carbon TEM grids, and drying the grids at room temperature for 10 min. ^{57}Fe Mössbauer spectroscopy was used to characterize the atomic structure of the FeNi catalyst on the Mg(Al)O support, while the X-ray absorption spectroscopy was used to characterize the Ni/Mg(Al)O catalyst. Thermal gravimetric analysis was carried out in a 100 mL/min flow rate of air to measure the purity of the produced and purified CNTs. The heating rate was 10ºC/min from room temperature to 950ºC.

3. 3 Results and Discussion

3.3.1 Properties of Mg(Al)O Support and Catalysts

Hydrotalcite (HTL) compounds, also known as layered double hydroxides (LDH), are natural or synthetic materials with the general formula of $[M^{2+}_{1-x}M^{3+}_{x}(OH)_2]A^{n-}_{x/n}\cdot mH_2O$, where M^{2+} and M^{3+} represent divalent and trivalent cations in the octahedral sites within the hydroxyl layers, x is equal to the ratio of $M^{3+}/(M^{2+}+M^{3+})$, typically in the range of 0.17-0.33, and A^{n-} is the exchangeable interlayer anion, balancing the positive charge on the layers. The $M^{2+}/M^{3+}(OH)_6$ octahedra form two-dimensional sheets that stack together by hydrogen bonding between the hydroxyl groups of adjacent sheets. Usually, synthetic hydrotalcites are reported to have a hexagonal structure [75]. In this study, M^{2+} and M^{3+} represent Mg^{2+} and Al^{3+} cations, respectively, and $x = 0.167$.

Figure 3.1 shows the X-ray powder diffraction patterns of MgAl-HTL as-prepared, the Mg(Al)O catalyst support prepared by calcination of MgAl-HTL at 550°C for 5 h, and the as-prepared FeNi/Mg(Al)O catalyst. The XRD pattern of MgAl-HTL exhibits a typical crystalline layered double hydroxide structure with a hexagonal stacking. Kuśtrowski et al. [76] found that the crystallinity of HTL decreased with increasing molar ratio of Mg to Al. In our experiments, we used a Mg to Al molar ratio of 5, which is on the borderline of effective formation of HTL. The crystallite size of the as-prepared MgAl-HTL was calculated from the FWHM of the (018) and (006) reflections using the Debye-Scherrer formula and found to be around 6 nm. Thermal decomposition of HTL leads to a solid solution, which is characterized by a high surface area and homogeneous dispersion of the metal oxides. The XRD pattern of

Mg(Al)O after calcination at 550ºC for 5 h shows only the pattern of cubic MgO with high crystallinity due to the fact that aluminum ions also occupy the octahedral sites in the MgO lattice. This special structure has been verified by ^{27}Al solid state NMR by Schapter et al. [74] The thermal decomposition behavior of MgAl-HTL was studied by Rao et al. [77] using a TG-DTA thermogram. They observed three main stages: (1) the loss of physisorbed and interlayer water below 260°C; (2) dehydroxylation and removal of carbonate ions between 260°C and 500°C; and (3) the decomposition of $MgCO_3$ above 500°C. In our experiment, calcination at 550ºC is sufficient for dehydroxylation to form Mg(Al)O oxide with a high surface area. The XRD pattern of the as-prepared FeNi/Mg(Al)O catalyst exhibits no obvious difference from that of the pure Mg(Al)O support, indicating that Fe^{3+} trivalent ions and Ni^{2+} divalent ions are either dispersed in the support or are present in oxide particles too small in size and amount to yield a significant diffraction pattern.

The surface areas of the Mg(Al)O support, and the Ni/Mg(Al)O and the FeNi/Mg(Al)O catalysts, both as-prepared and reduced in hydrogen, are listed in Table 3.1. It is seen that the surface areas decrease slightly on adding the catalyst precursors, possibly due to interaction between the precursor and the support, and undergo a more significant decrease after reduction at 700ºC due to sintering of both the support and the catalyst particles. The decrease in surface area during reduction for the FeNi/Mg(Al)O catalyst was ~30%. Schaper et al. [74] investigated the effect of the calcination temperature on the surface area of similar Mg(Al)O compounds and found that increasing it from 500 to 700ºC decreased the surface area by 20%.

The morphologies of the as-prepared material and the reduced FeNi/Mg(Al)O catalyst are shown in Figure 3.2. In the TEM mode (Figure3.2a, c), the contrast of catalyst particles and the Mg(Al)O support is relatively weak. However, it clearly shows that the Mg(Al)O support is made up of loosely sintered nanocrystals with particle sizes of the order of 10-20 nm size, in rough agreement with the value estimated from the XRD line broadening using the Debye-Scherrer equation. After the catalyst was reduced at 700°C for 2 h in H_2, some sintering of the support can be seen (Figure

3.2c). In the STEM mode, (Figure 3.2d), metallic FeNi catalyst particles having a broad size distribution ranging from small nanoparticles (~10 nm) to relatively large particles (20-40 nm) are clearly observed. No distinct Fe or Ni oxide particles are observed on the as-prepared catalyst (Figure 3.2b), which indicates that Fe and Ni are well and evenly dispersed prior to reduction. The Ni/Mg(Al)O catalyst shows similar results.

Figure 3.3 shows the Ni K-edge X-ray absorption near edge structure (XANES) spectrum and the Fourier transform (FT) of the k^3-weighted extended X-ray absorption fine structure (EXAFS) of the as-prepared Ni/Mg(Al)O catalyst. The corresponding spectra of NiO and NiMgO (Ni:Mg=1:1, atomic ratio) solid solution are also shown for reference. The XANES spectrum of the as-prepared Ni/Mg(Al)O resembles that of NiMgO in the white-line region. Both the spectra of the as-prepared Ni/Mg(Al)O and NiMgO solid solution have more intense white lines than that of NiO. The peaks at around 8360 eV and 8400 eV, marked by arrows in Figure 3.3, shift to lower energy with reduced Ni content and become narrower compared to those of pure NiO.

The radial structure function (RSF) resulting from Fourier transform of the k^3-weighted EXAFS in the range of 3-13 Å^{-1} of the as-prepared Ni/Mg(Al)O catalyst is also shown in Figure 3.3 (bottom). The first peak at ~1.5 Å is due to the backscattering by the nearest oxygen shell, and the second peak is due to backscattering by Ni next nearest neighbors in the second coordination shell in pure NiO or by (Mg, Ni) neighbors in Ni/Mg(Al)O catalyst and the NiMgO solid solution. The intensity of the second peak of as-prepared Ni/Mg(Al)O catalyst is much lower than that of NiMgO solid solution, which is likely due to the dilution of Ni in the Mg(Al)O support. Yoshida et al. [78] conducted an in-depth study of the NiO-MgO system by XAFS. It was concluded that a solid solution was formed by impregnation of MgO powder with an aqueous solution of $Ni(NO_3)_2$ followed by calcination at 500ºC over the entire range of Ni concentration. Here, the RSF spectra of the as-prepared Ni/Mg(Al)O catalyst and NiMgO solid solution closely match those of

$Ni_xMg_{1-x}O$ compounds with x equal to 0.02 and 0.48, respectively, as observed by Yoshida et al. [78] This similarity indicates that all the Ni in the as-prepared Ni/Mg(Al)O catalyst is incorporated into octahedral sites in the Mg(Al)O lattice. To confirm this conclusion, FEFF EXAFS analysis was performed in R-space over the range of 1-3 Å, which includes only the first two coordination shells. The combined coordination number for the Ni-M next nearest shell was constrained to equal twice that of the Ni-O nearest shell. The RSF and the back Fourier transform spectrum (q-space) of the first two shells of the as-prepared Ni/Mg(Al)O and the fitting data are shown in Figure 3.4 and Table 3.2. Agreement in both R and q space for the as-prepared Ni catalyst was obtained with a two-shell fit, including Ni-O for the first shell and a second shell consisting of separate Ni-Ni and Ni-Mg contributions. The latter contribution was derived using ATOMS and FEFF6 procedures for 5% Ni in MgO. [79-81] Therefore, it can be concluded that all Ni species are present in octahedral sites in the Mg(Al)O lattice, forming a solid solution. The coordination number of Ni atoms in the next nearest shell is much less than the number of Mg atoms, but is consistent with the anticipated composition for a random solid solution of 5% Ni in MgO, which should result in 0.6 Ni and 11.4 Mg next nearest neighbors.

The Ni K-edge XANES spectrum and the RSF from Fourier transformation of the k^3-weighed EXAFS of Ni/Mg(Al)O after reduction in H_2 and after dehydrogenation of ethane for 2 h at 500ºC, together with the corresponding spectral data for a Ni foil, are shown in Figure 3.5. The RSFs of the reduced Ni/Mg(Al)O and the reacted catalyst are similar to those of Ni foil, but the intensities of the first Ni-Ni shell in the RSFs of the catalyst samples are much lower, indicating the presence of some oxidized Ni in the catalysts. To quantify the degree of reduction, least squares fitting of the XANES spectra of reduced and reacted Ni/Mg(Al)O was conducted by using SixPACK software. The fitting components include the XANES spectra for Ni foil, NiO, and the as-prepared catalyst, representing respectively metallic nickel in the catalyst particles, re-oxidized Ni on their surfaces, and unreduced Ni in the Mg(Al)O lattice. The fitting results are shown in Figure 3.6 and Table 3.3, which lists results for alternative fits as well as for the optimum fit. The catalyst after 2 h of ethane dehydrogenation shows somewhat more metallic Ni (~75%) than the as-reduced catalyst (~65%). However, the amount of re-oxidized Ni in the reacted catalyst is much less significant, which suggests that the formation of CNTs after ethane dehydrogenation reaction may protect Ni particles from reoxidation due to exposure to air. There is no evidence of the formation of nickel carbide after 2 h of the ethane dehydrogenation reaction [20, 82].

Mössbauer spectra were collected at room temperature for the FeNi/Mg(Al)O catalyst as-prepared, after reduction at 700ºC for 2 h, and after ethane dehydrogenation at 650°C for 8 h. The spectra are shown in Figure 3.7. The Mössbauer parameters and the contributions of the various iron species identified by least squares analysis of the spectra are summarized in Table 3.4. The spectrum recorded the as-prepared catalyst consists of two quadrupole doublets, indicating two distinct ferric iron species. The doublet with the smaller quadrupole splitting is attributed to Fe^{3+} incorporated into the Mg(Al)O lattice, forming a Mg-Ni-Al-Fe-O complex with Fe^{3+} in an asymmetric environment [83-86]. The doublet with the larger QS value is attributed to formation of Fe^{3+} clusters on the surface of support [84].

After reduction, only about 20% of the iron in the FeNi/Mg(Al)O catalyst is present in metallic form. The broad magnetic sextet is derived from the formation of a magnetic Fe-Ni (bcc) alloy (13%), while the sharp single peak indicates the formation of an austenitic Fe-Ni-C (fcc) alloy phase (7%). A significant percentage of the Fe remains as ferric oxide, although the component with the larger QS may contain a small admixture of Fe^{2+}.

After the ethane dehydrogenation reaction, the Mössbauer spectrum consists of two broad magnetic sextets derived from an Fe-Ni martensitic (bcc) alloy (33%) and a sharp single peak from an Fe-Ni-C (fcc) austenitic alloy (19%). The sextet with the smallest magnetic hyperfine field (H_0 = 193 kG) can be assigned to Fe(Ni) carbide (19%). The remaining absorption (29%), which has been fitted as two very broad (width = 1.9 mm/s) quadrupole components, most likely results from superparamagnetic (spm) FeNi oxide with a spin relaxation time close to that of the Larmor precession time [87]. In view of the small FeNi particle size (10-40 nm), much of this oxide may have formed spontaneously on removing the catalyst from the reactor and exposing it to air. These broad quadrupole components may also obscure an absorption doublet associated with the austenite phase due to Fe atoms in the metal that have carbon nearest neighbors. It is likely that the Fe-Ni-C austenite and the Fe-Ni martensite phases are both active metallic phases for ethane dehydrogenation and CNTs formation. Catalyst deactivation may be due to the formation of the carbide phase.

3.3.2 Ethane Dehydrogenation

Ethane dehydrogenation was conducted over Ni/Mg(Al)O and FeNi/Mg(Al)O catalysts at temperatures of 500, 650 and 700ºC with undiluted ethane flowing with a space velocity of 600 $ml\cdot h^{-1}g^{-1}$. During noncatalytic thermal cracking, ethane does not decompose at all at 500ºC, and decomposes to 22.5 vol.% H_2, 10 vol.% CH_4, 19.5 vol.% ethene, and 48 vol.% unreacted ethane at 650ºC. Based on the product distribution, a possible reaction pathway for thermal cracking of ethane is proposed as follows: ethane first cracks to ethene and H_2, then ethene further decomposes to methane and carbon. Some of the carbon can react with H_2 to produce more methane.

$$C_2H_6 \rightarrow C_2H_4 + H_2 \qquad (3\text{-}2)$$

$$C_2H_4 \rightarrow CH_4 + C \qquad (3\text{-}3)$$

$$C + 2H_2 \rightarrow CH_4 \qquad (3\text{-}4)$$

The generally accepted reaction pathways for catalytic ethane dehydrogenation to hydrogen, methane, and surface deposited carbon (C_S) are provided by the following equations:

$$C_2H_6 \rightarrow CH_4+C_S+H_2 \qquad (3\text{-}5)$$

$$C_2H_6 \rightarrow 2C_S+3H_2 \qquad (3\text{-}6)$$

The following reaction is reversible (methane cracking or methanation) depending on the reaction temperature and the catalyst used.

$$C_s+2H_2 \longleftrightarrow CH_4 \qquad (3\text{-}7)$$

There is an additional step, the formation of filamentous carbon (C_f), including both fibers and nanotubes (CNTs), from surface deposited carbon (C_S), determined by the carbon diffusion rate through or around the catalyst particles [28, 88, 89].

$$C_s \longrightarrow C_f \qquad (3\text{-}8)$$

Figure 3.8 shows the time-on-stream (TOS) product distribution from ethane decomposition over the Ni/Mg(Al)O catalyst at 500 and 650ºC. At 500ºC, Ni/Mg(Al)O exhibits good catalytic performance. It maintains catalytic activity for over 16 h with almost 100% ethane conversion to ~ 20 vol.% H_2 and 80 vol.% of methane. Given that three times more methane than H_2 is produced at 500ºC, the dominant reaction is reaction (3-5), producing equal molar C_S, methane, and H_2. Nearly 1/3 of C_S further reacts with H_2 to yield more methane, and the remainder becomes CNTs. As discussed later, the CNTs produced in this reaction have a stacked-cone nanotube (SCNT) structure. Therefore, the overall reaction of ethane dehydrogenation over Ni/Mg(Al)O catalyst at 500ºC can be expressed as:

$$3C_2H_6 \rightarrow 4CH_4+H_2+2C_f \qquad (3\text{-}9)$$

The chemical reaction rate is in equilibrium with the carbon consumption rate from the catalyst surface, including the methanation reaction and C_S diffusion to form SCNTs, which allows the catalyst to maintain its activity. After 16.7 h, the available active metal surface of the Ni catalyst particles becomes enclosed in the SCNTs and the catalyst then gradually deactivates.

On further increasing the temperature to 650ºC, methane cracking becomes dominant over the methanation reaction, increasing the H_2 yield. Moreover, build-up of carbon occurs on the surfaces of catalyst particles since the deposition rate of carbon at the surface is greater than the rate of its removal by diffusion through the catalyst particle.

Hence the catalyst particles become saturated with carbon resulting in loss of catalytic activity and ethane decomposition diminishes to the level of thermal cracking. Ethene is increasingly detected as a product as the catalyst loses its activity at 650ºC.

Figure 3.9 shows the time on stream (TOS) product distribution from ethane decomposition over a bimetallic FeNi/Mg(Al)O catalyst at reaction temperatures of 500 and 650ºC. At 500ºC, the FeNi/Mg(Al)O catalyst shows less activity than that of the Ni/Mg(Al)O catalyst. At the beginning of reaction, it converts ethane completely to 20 vol.% H_2 and 80 vol.% of methane, just as the Ni catalyst does. However, it gradually deactivates to a new equilibrium level of 7.5 vol.% of H_2, with unreacted ethane as the balance of the product gas.

On increasing the reaction temperature to 650ºC, the FeNi/Mg(Al)O catalyst exhibits a dramatic increase in H_2 production (over 65 vol.% H_2 and 10 vol.% methane) and maintains its activity for over 5 h before gradually declining to the thermal cracking level. On comparing these data with those of the monometallic Ni/Mg(Al)O catalyst, it is evident that the rate of diffusion of carbon through the FeNi alloy catalyst at 650ºC must be enhanced relative to that for the pure Ni catalyst.

The driving force for carbon diffusion inside the catalyst particles and the formation of filamentous carbon is due to the carbon concentration gradient, arising from the difference in carbon solubility at the gas/catalyst particle surface and CNT/catalyst particle surface [88, 90]. At steady state, the rates of the ethane decomposition reaction, net surface reaction, and carbon diffusion through the catalyst particle are equal. At 650ºC, the carbon diffusion rate in bimetallic FeNi/Mg(Al)O is apparently much faster than that in monometallic Ni/Mg(Al)O catalyst. Thus, the former can maintain steady state operation for a reasonable period of time, but the latter deactivates quickly during reaction. Hence, inclusion of the second metal to form a metal alloy can significantly change the carbon diffusivity or solubility inside the catalyst particles at elevated temperatures, prolonging catalyst life-time [91]. Catalyst deactivation after a period of steady state operation may be due to the formation of a new phase, metal carbide, which lowers the solubility of carbon at the gas/catalyst particle surface or the diffusion coefficient of carbon atom through the catalyst particle. For example, the diffusion coefficient of carbon through Fe_3C is 10^4 times lower than that through austenite [38], which significantly lowers the driving force for carbon diffusion. Additionally, gas access to the catalyst particles is gradually reduced by enclosure within CNTs, as noted earlier.

Figure 3.10 summarizes the TOS H_2 production over the Ni/Mg(Al)O and bimetallic FeNi/Mg(Al)O catalysts at 500, 650 and 700ºC. The Ni/Mg(Al)O catalyst has the longest lifetime at 500ºC. It maintains catalytic activity for 16.7 h with 100% ethane conversion, but the H_2 selectivity is only 25%, and the net gain of hydrogen (the total hydrogen production subtracts the hydrogen consumption for the reduction of the catalyst) during this period of time is 3316 mL/g catalyst. At 650 and 700ºC, the monometallic Ni catalyst deactivates quickly. The bimetallic FeNi/Mg(Al)O catalyst shows high H_2 selectivity and activity at 650ºC, at which temperature H_2 generation is ~65 vol. % and is maintained for over 5 h. The net gain of hydrogen until deactivation at 470 min is about 4418 mL/g catalyst. At 700ºC, both the Ni catalyst and the FeNi catalyst deactivate very quickly, but the FeNi catalyst exhibits a higher H_2 yield.

3.3.3 TEM Characterization of CNTs

The morphology of the CNTs produced over Mg(Al)O supported catalysts was investigated using high resolution transmission electron microscopy (HRTEM). Figure 3.11 shows the CNT structures produced by ethane decomposition over FeNi/Mg(Al)O catalyst at reaction temperatures of 525 and 650ºC, respectively. The structure of CNTs is very sensitive to reaction temperature. At 525ºC, the CNTs have a stacked-cone nanotube structure (SCNT), and at 650ºC, they are predominantly concentric parallel-walled MWNTs. Figure 3.12 shows the structure of CNTs produced over the Ni/Mg(Al)O catalyst at temperatures of 500 and 650ºC. At 500ºC, the CNTs are essentially all SCNTs. However, at 650ºC, onion-like structured carbon soot is formed together with filamentous carbon. The formation of the onion-like carbon soot was also observed by Nolan et al. [92] on supported Ni and Co particles at 600ºC for the CO disproportionation reaction.

The formation of MWNTs and SCNTs over bimetallic Fe-M (Ni, Mo, Pd) catalysts supported on γ-Al_2O_3 was discussed previously. [45] The CNT nanostructures grow away from the surfaces of the binary catalyst particles because the catalyst particles are anchored to the alumina support by the formation of hercynite ($FeAl_2O_4$). However, the catalyst particles supported on Mg(Al)O exhibit a tip growth mechanism of CNT formation. This is illustrated by Figure 3.13, which shows metal catalyst particles at the tips of CNTs formed by ethane dehydrogenation over Ni/Mg(Al)O and FeNi/Mg(Al)O catalysts at 500ºC. Such structures have also been observed, for example, by Dai et al. [93] using a patterned catalyst array. It is generally agreed that formation of CNTs by CCVD involves three steps, consisting of the formation of surface carbon C_S, the dissolution and diffusion of the C_S through the catalyst particle, and the nucleation of carbon filaments. [94] Because of different interactions between catalyst metal particles and the support, the catalyst particles either move forward to the tips of the nanotubes while the CNTs are generated on the rear (tip growth mechanism) or remain attached to the support while the CNTs grow away from the anchored particles (base growth mechanism). Tip growth would appear to have advantages for our application, which is focused on producing large quantities of hydrogen and nanotubes. The metal particles move away from the support and form a loosely connected aggregate of CNTs inside the reactor. Moreover, it favors the formation of CNTs with open ends, making the CNTs produced easier to clean.

3.3.4 CNTs Purification

The carbon product from ethane decomposition was collected after reaction and treated in 6M HNO_3 to remove the catalyst. The reaction was carried out either at room temperature for 2 h or in hot 6M HNO_3 solution under reflux for 2 h. Figure 3.14 shows the XRD patterns of the CNTs as-prepared after 40 h reaction at 500ºC on Ni/Mg(Al)O, the CNTs after HNO_3 treatment, and carbon black for reference. The as-prepared CNTs show a large graphite peak at $2\theta = 26^\circ$ (marked with a triangle) and peaks from the Mg(Al)O support (marked with a star). After treatment in 6M HNO_3 solution, the XRD patterns show only the graphitic peaks as indexed, [95] establishing that high purity CNTs can be obtained by this mild acid treatment. Figure 3.15 shows typical TEM images of purified SCNTs (by cold HNO_3 solution) produced by ethane dehydrogenation at 500ºC over a Ni/Mg(Al)O catalyst and MWNTs prepared over an FeNi/Mg(Al)O catalyst at 650ºC. No catalyst particles are observed and the nanotubes exhibit open ends, typical of CNTs formed by the tip growth mechanism, which leaves the metal catalyst particles accessible to the acid solution. Thermal gravimetric analysis shown in Figure 3.16 establishes that the residue of as-prepared SCNTs is 17.2 wt.% and that of the as-prepared MWNTs is 36.2 wt.%, while the residues of the purified SCNTs and MWNTs are both close to 0. The major weight loss occurs over the temperature range from 450 to 650ºC for all samples. After cooling the samples to room temperature, the purities of purified CNTs could be determined more accurately by weight loss and were found to be 99.5% for the SCNTs and 99.6% for the MWNTs.

3.4 Summary and Conclusions

Mg(Al)O supports prepared by calcination of Mg-Al hydrotalcite with a Mg/Al molar ratio of 5 consist of Mg-Al-O nanocrystal agglomerates with large surface areas. Ni and FeNi catalysts were dispersed onto the Mg(Al)O support by an incipient wetness method followed by calcination at 550ºC for 5 h. The catalysts were first reduced in hydrogen at 700ºC for 2 h, and then reacted with undiluted ethane. Catalytic dehydrogenation of ethane was carried out at temperatures ranging from 500 to 650ºC over both types of catalyst. The principal results are summarized below:

1. At 500ºC, the Ni/Mg(Al)O catalyst was highly active and very stable with 100% conversion of ethane to 20 vol.% H_2 and 80 vol.% methane. It exhibited no loss of activity for over 16.7 h at a space velocity of 600 $mL\cdot h^{-1}g^{-1}$ of undiluted ethane. The CNTs were all in the form of SCNT.

2. The FeNi/Mg(Al)O exhibited its best catalytic behavior at 650ºC, at which temperature it was active for over 5 h, yielding 65 vol.% H_2, 10 vol.% CH_4, and 25 vol. % unreacted ethane.

3. At 500ºC, the CNTs produced over the Ni/Mg(Al)O catalyst were predominantly SCNTs. Increasing the temperature to 650ºC led to an onion soot/fiber mixture that rapidly deactivated the catalyst.

4. The CNTs formed over the FeNi/Mg(Al)O catalyst changed with temperature from SCNTs (525ºC) to parallel-walled MWNTs (650ºC).

5. TEM and STEM established that the reduced catalysts consisted of metallic nanoparticles 8-40 nm in size dispersed on the Mg(Al)O. XAFS and Mössbauer spectroscopy established that the active phases were metallic Ni and FeNi alloys, although significant oxide phases were also present. Both austenitic Fe-Ni-C and martensitic Fe-Ni alloy phases were observed in the Fe-Ni catalyst after reaction.

6. The presence of Ni and Fe oxides after reduction and reaction is due to incomplete reduction and/or re-oxidation on exposure to air. The oxides were identified by Ni XAFS spectroscopy and ^{57}Fe Mössbauer spectroscopy.

7. The CNTs were formed by a tip growth mechanism over the Mg(Al)O supported catalysts and were easily purified by a one-step 6M nitric acid treatment.

Table 3.1. Surface areas of the Mg(Al)O support and the Ni/Mg(Al)O and FeNi/Mg(Al)O catalysts in as-prepared and reduced states (under 50 mL/min H_2 at 700ºC for 2 h).

Sample	BET area* (m^2/g)	External surface area* (m^2/g)
Mg(Al)O support	154	167
Ni/Mg(Al)O as-prepared	114	130
Ni/Mg(Al)O reduced	101	114
FeNi/Mg(Al)O as-prepared	122	137
FeNi/MgAlO reduced	84	94

*Note: The error is within 1%.

Table 3.2. Curve fitting results for the as-prepared Ni/Mg(Al)O catalyst.

Shell	R, Å	N	E_0	σ^2, $Å^2$
Ni-O	2.09±0.01	6	-4.3±2.0	0.006±0.001
Ni-Ni	2.96±0.06	1±1	-25.6±19.3	0.006±0.003
Ni-Mg	2.96±0.06	11±1	-3.8±3.0	0.022±0.006

Table 3.3. Results of least squares fitting of Ni XANES spectra of Ni/Mg(Al)O catalysts.

Items	Ni foil	As-prepared Mg(Ni)O	NiO	Reduced Chi Squared
Reduced	0.65	0.21	0.13	1.9×10-4
	0.69	0.31	-	2.6×10-4
	0.68	-	0.32	3.8×10-4
	1	-	-	15.3×10-4
After 2 h reaction	0.74	0.20	0.06	3.1×10-4
	0.75	0.25	-	3.2×10-4
	0.76	-	0.24	4.8×10-4
	1.0	-	-	11.4×10-4

Table 3.4. Mössbauer parameters of FeNi/Mg(Al)O catalyst as-prepared, reduced, and after reaction. (Spectra collected at room temperature)

Catalyst	IS mm/s	QS mm/s	H_0 kGauss	width mm/s	%Fe	ID
Fresh	0.33	0.66	--	0.49	71	Fe^{3+} in oxide
	0.30	1.15	--	0.49	29	Fe^{3+} in oxide
After reduction at 700ºC for 2 h	0.38	0.65	--	0.60	30	Fe^{3+} in oxide
	0.52	1.07	--	1.40	50	$Fe^{3+}(Fe^{2+}?)$ in oxide
	0.05	--	285	1.16	13	Fe-Ni (bcc) alloy
	-0.08	--	--	0.30	7	Fe-Ni (fcc) alloy
After reaction at 650ºC for 8 h	0.34	0.58	--	1.90	29	Fe^{3+} oxide (spm)
	0.01	--	303	0.79	23	Fe-Ni (bcc) alloy
	0.00	--	265	0.62	10	Fe-Ni (bcc) alloy
	0.15	--	193	0.65	19	Fe(Ni)-C carbide
	-0.07	--	--	0.34	19	Ni-Fe(C) (fcc) alloy

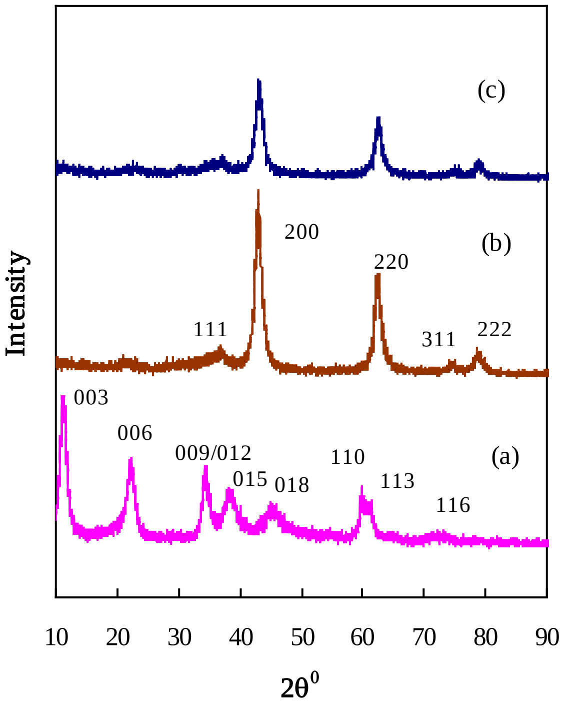

Figure 3.1. X-ray diffraction patterns of (a) HTL as-prepared, indexed according to JCPDS Card No. 22-700; (b) Mg(Al)O support after calcination of HTL at 550°C for 5 h, indexed according to JCPDS Card No. 45-0946; (c) FeNi/Mg(Al)O catalyst as-prepared.

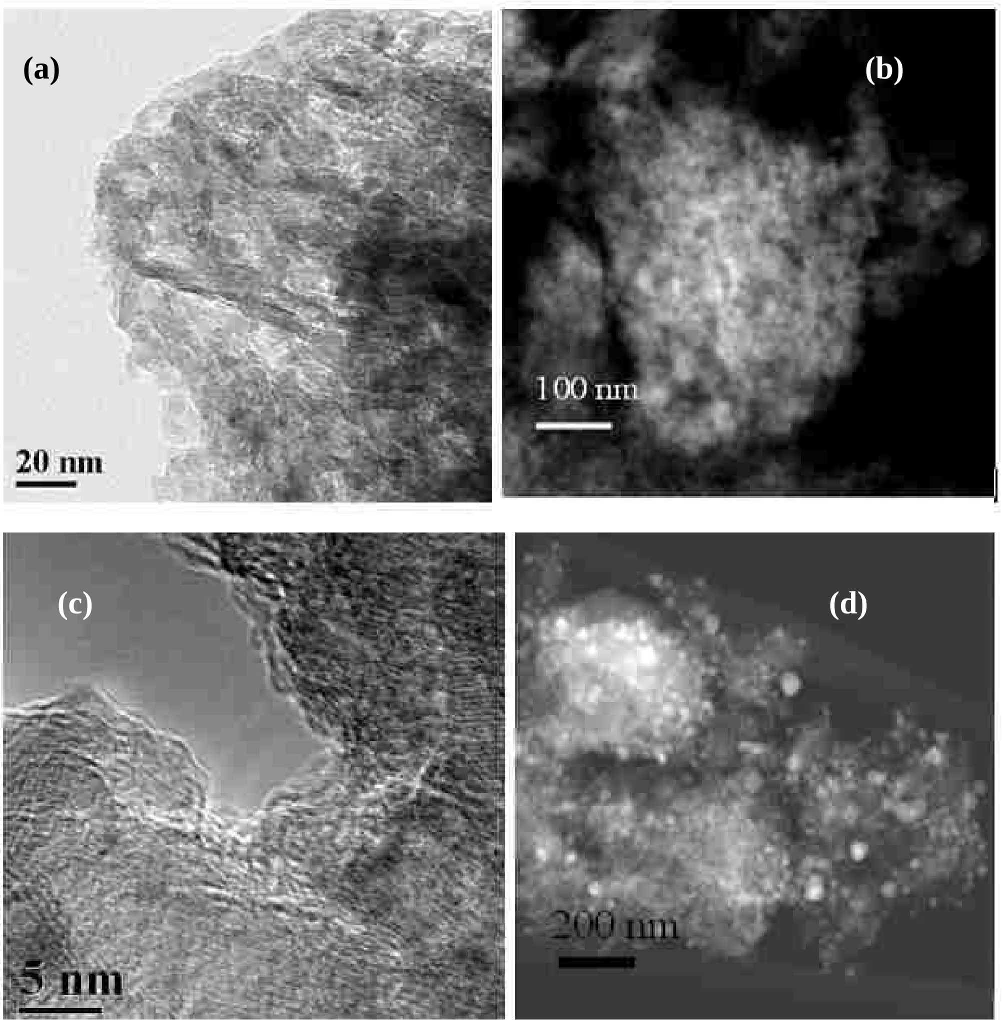

Figure 3.2. Micrographs of FeNi/Mg(Al)O catalyst: (a) TEM image of the as-prepared catalyst; (b) STEM image of as-prepared catalyst; (c) TEM image of catalyst reduced at 700°C for 2 h; (d) STEM image of reduced catalyst.

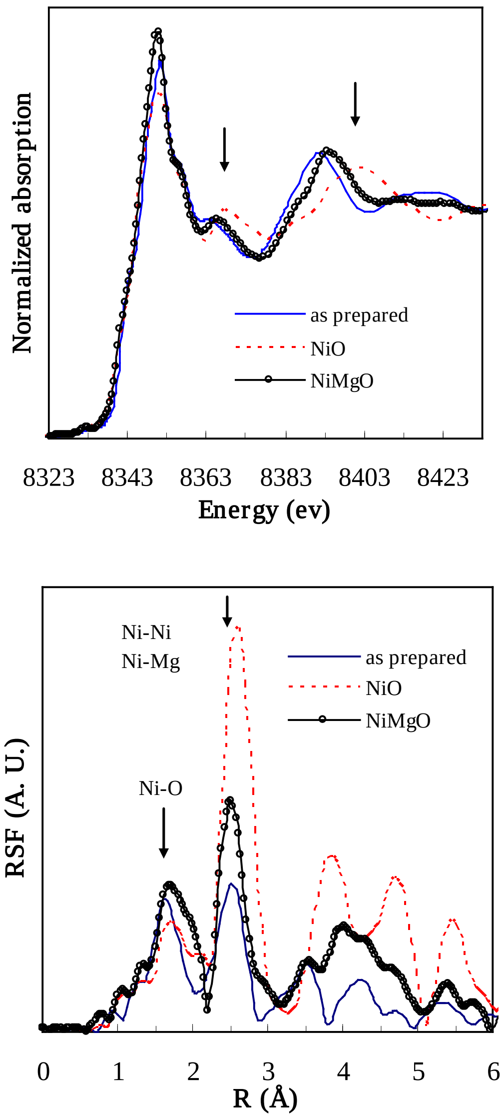

Figure 3.3. Ni K-edge XANES spectra (top) and Fourier transforms of k^3-weighted Ni K-edge EXAFS (bottom) of the as-prepared Ni/Mg(Al)O catalyst, NiO, and NiMgO solid solution.

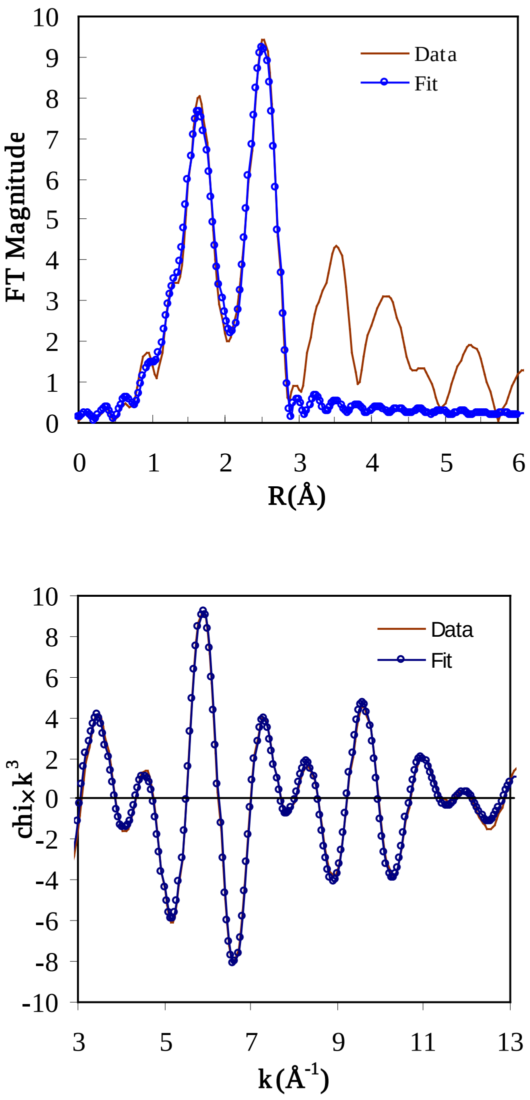

Figure 3.4. EXAFS spectrum for as-prepared Ni/Mg(Al)O: Radial structure function (top) and the back FT (q) spectrum for the first two shells (bottom), using the FEFF least-squares analysis.

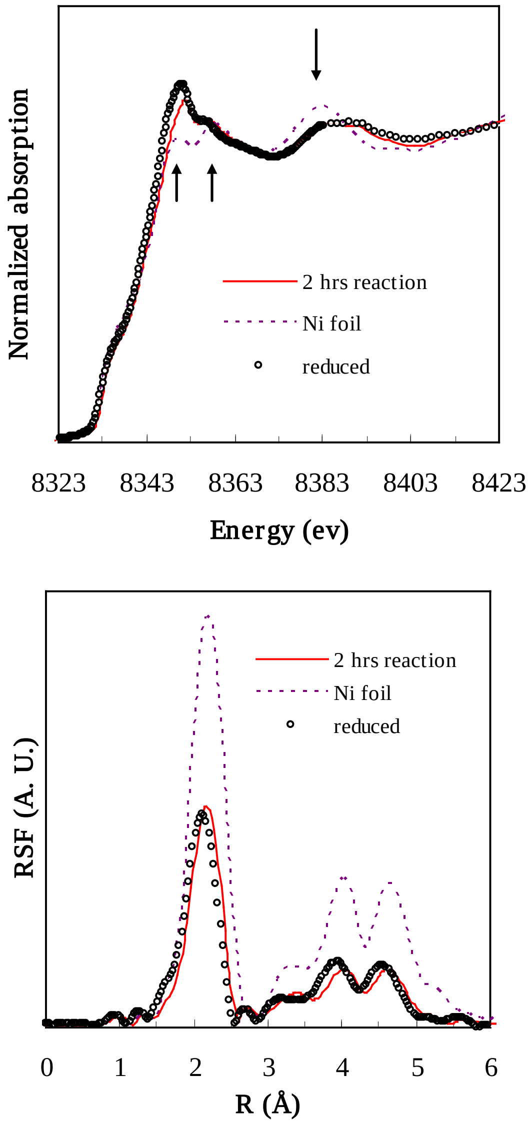

Figure 3.5. Ni K-edge XANES spectra (top) and RSF (bottom) of Ni/Mg(Al)O catalyst reduced and after 2 h of reaction, with Ni foil as a reference.

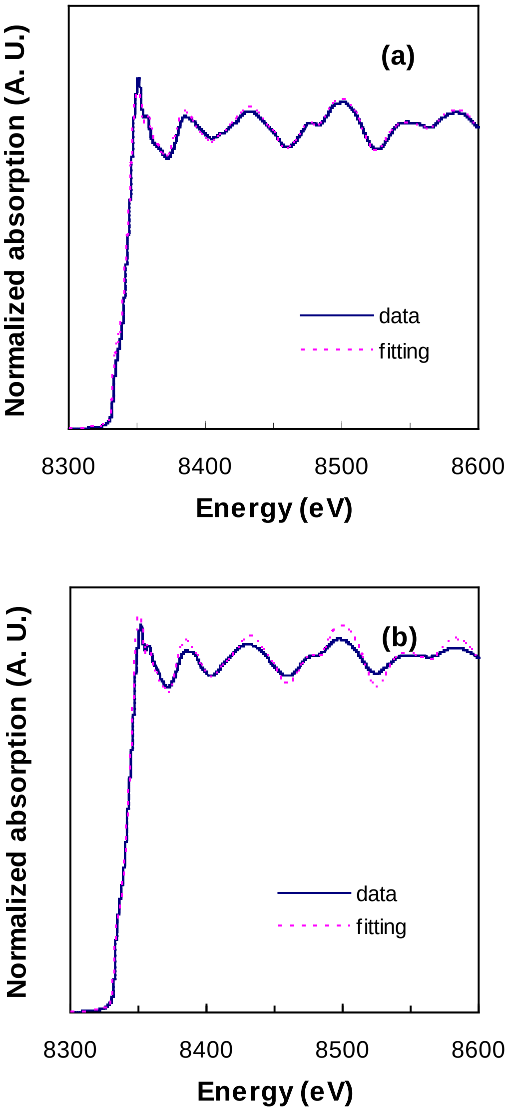

Figure 3.6. Least squares fitting of x-ray absorption spectra of Ni/Mg(Al)O catalyst: (a) reduced at 700 ºC for 4 h; (b) after 2 h reaction at 500°C. The fitting components include Ni foil, NiO and the as-prepared Ni/Mg(Al)O catalyst as illustrated in text.

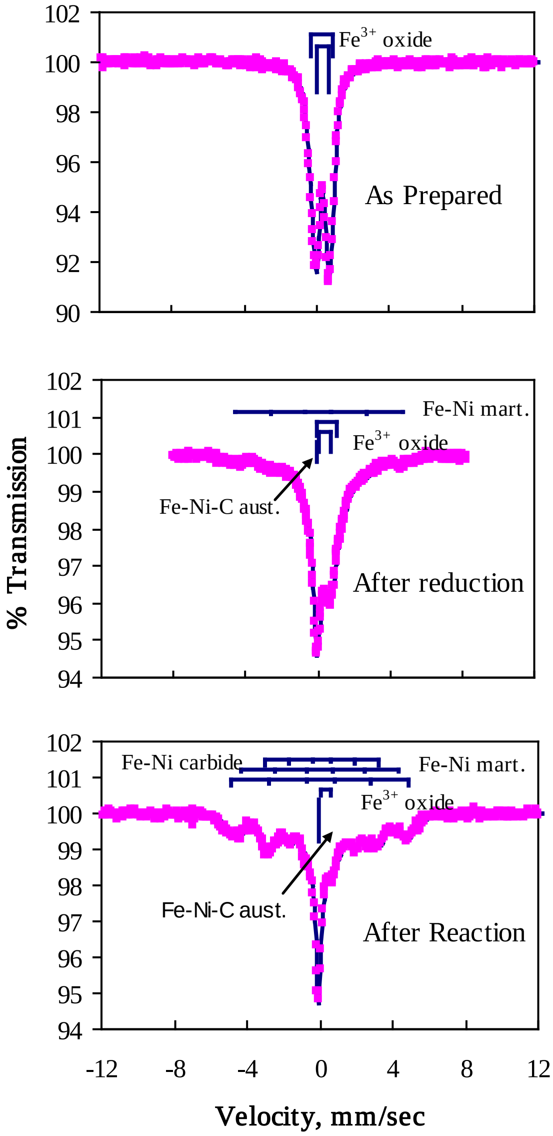

Figure 3.7. Mössbauer spectra of the FeNi/Mg(Al)O catalyst: as-prepared; after reduction at 700°C for 2 h; after the ethane dehydrogenation reaction at 650ºC for 8 h.

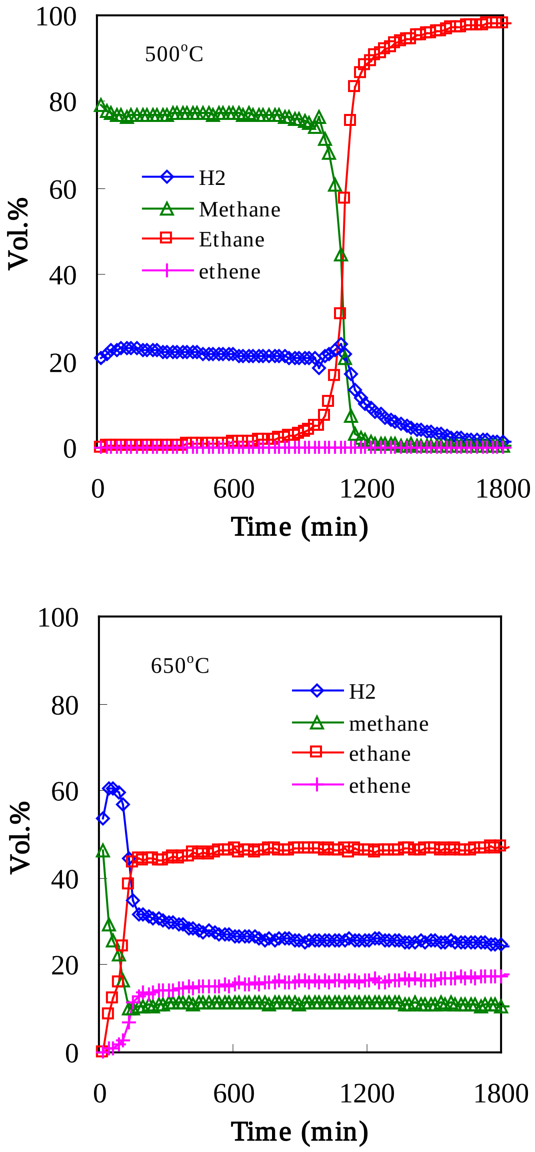

Figure 3.8. TOS product distribution of ethane dehydrogenation over Ni/Mg(Al)O catalyst at 500°C (top) and 650°C (bottom) temperatures.

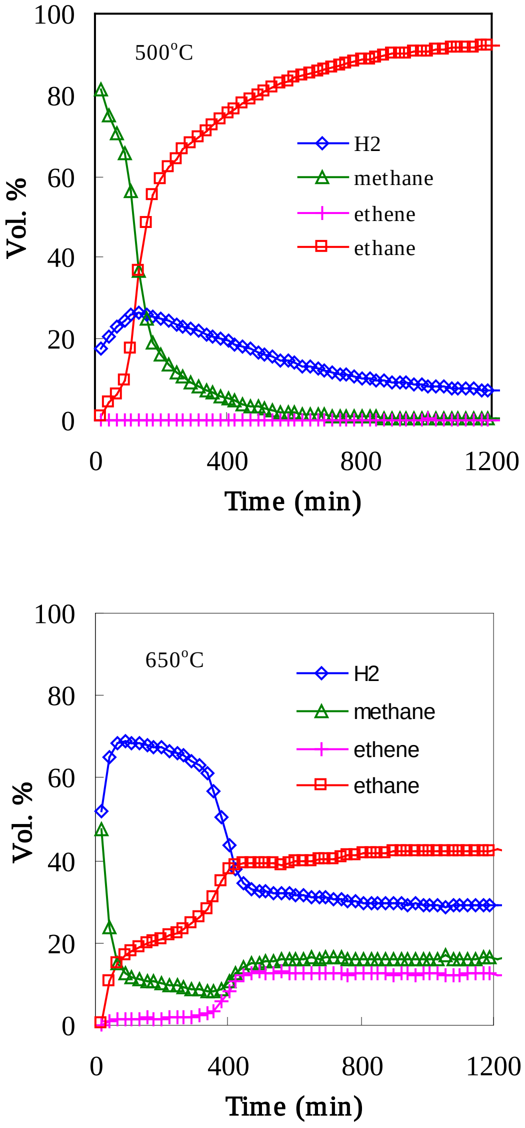

Figure 3.9. Time-on-stream product distribution for ethane dehydrogenation on FeNi/Mg(Al)O catalyst (Fe:Ni=65:35) at 500°C (top) and 650°C (bottom) temperatures.

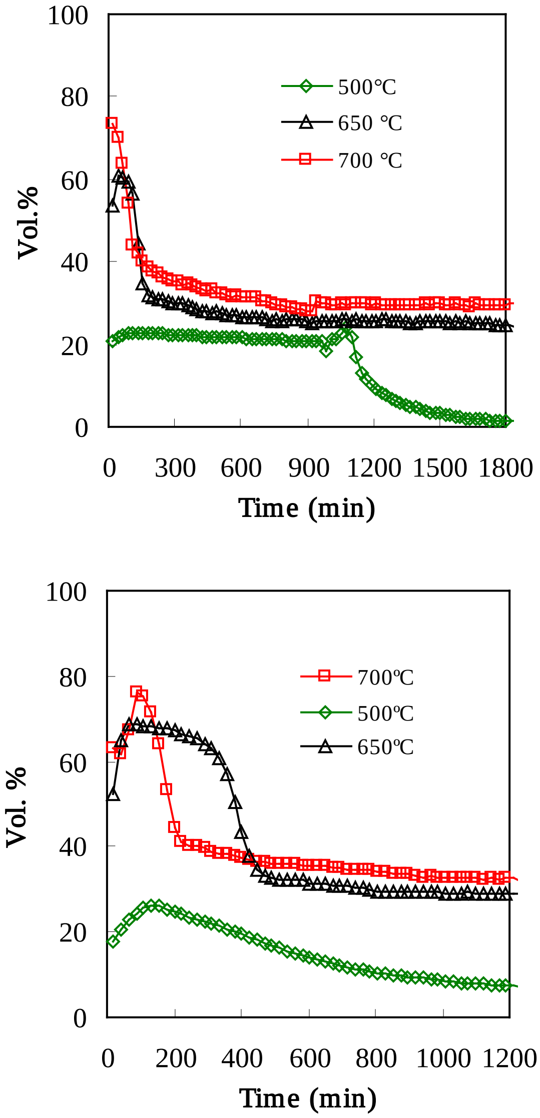

Figure 3.10. Time-on-stream hydrogen production by ethane dehydrogenation over Ni/Mg(Al)O (top) and FeNi/Mg(Al)O (bottom) catalysts at different temperatures.

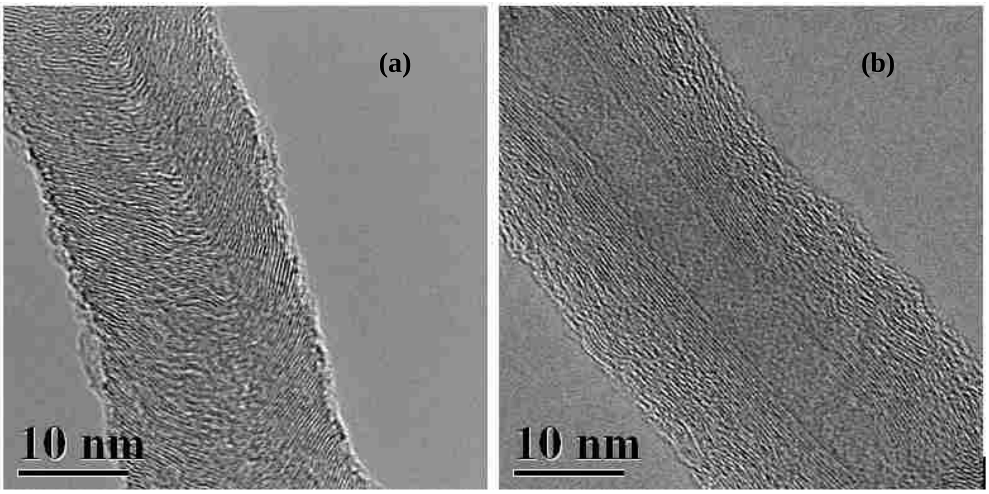

Figure 3.11. HRTEM images of CNTs deposited on FeNi/Mg(Al)O catalyst by ethane dehydrogenation. Reaction temperature: (a) 525ºC; (b) 650ºC.

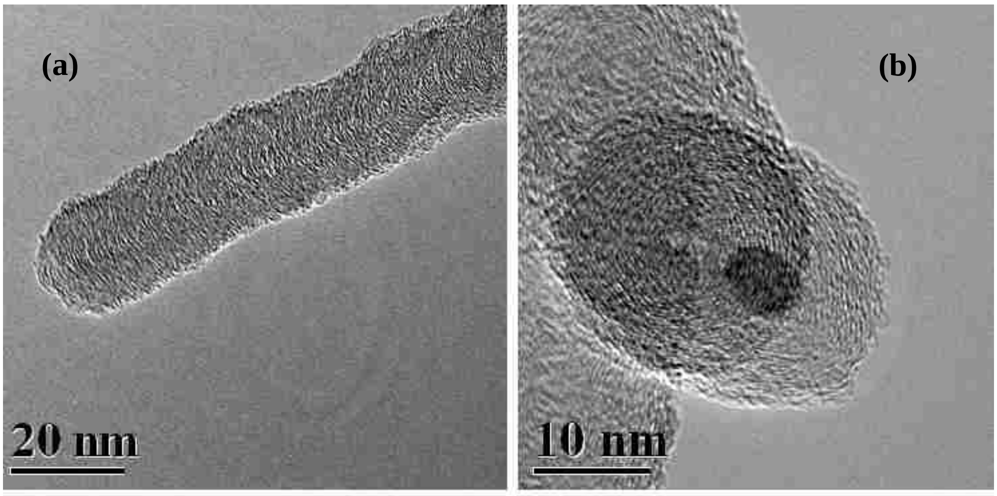

Figure 3.12. HRTEM images of CNTs deposited on Ni/Mg(Al)O catalyst by ethane dehydrogenation. Reaction temperature: (a) 500ºC; (b) 650ºC.

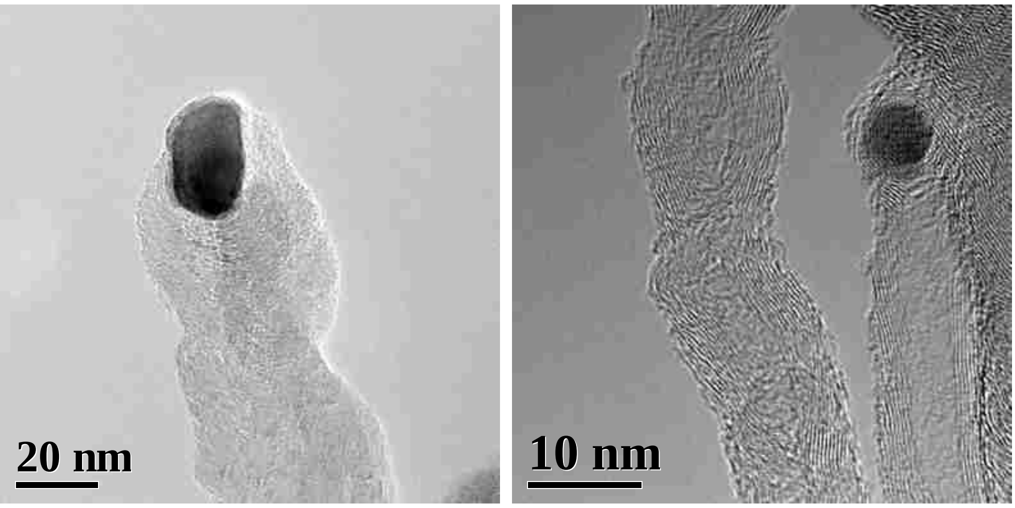

Ni/Mg(Al)O FeNi/Mg(Al)O

Figure 3.13. HRTEM images illustrating the tip growth mechanism of CNT formation. Catalyst particle size determines the diameter of formed CNTs. Reaction temperature: 500ºC.

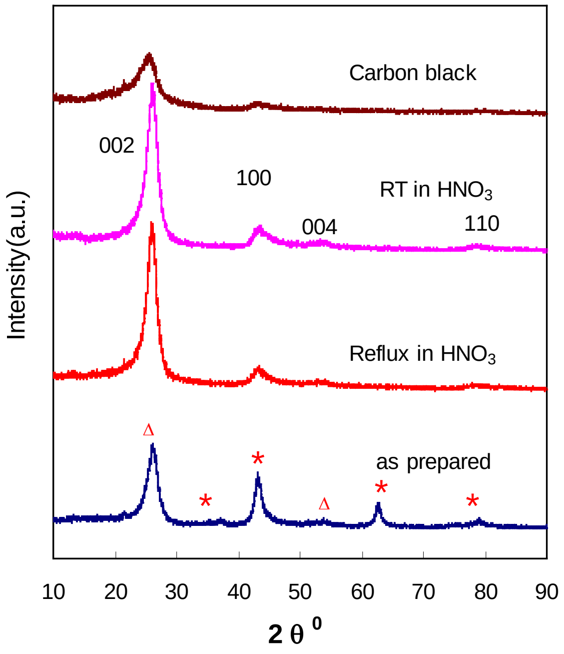

Figure 3.14. XRD patterns of the CNTs as-prepared and purified both at room temperature and reflux condition. The XRD pattern of carbon black is shown as a reference.

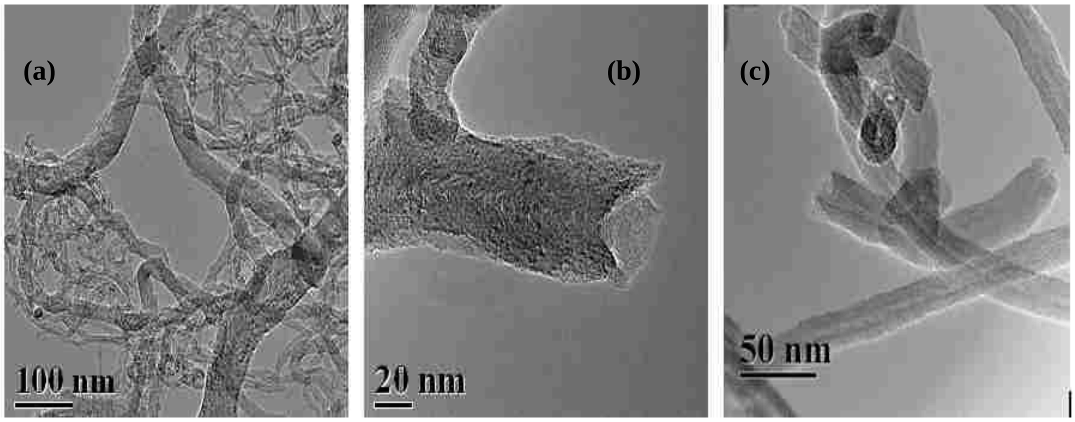

Figure 3.15. TEM images of (a), (b) purified SCNTs produced by ethane decomposition using the Ni/Mg(Al)O catalyst (500ºC, 40 h) and (c) purified MWNTs produced by using the FeNi/Mg(Al)O catalyst (650ºC, 8 h).

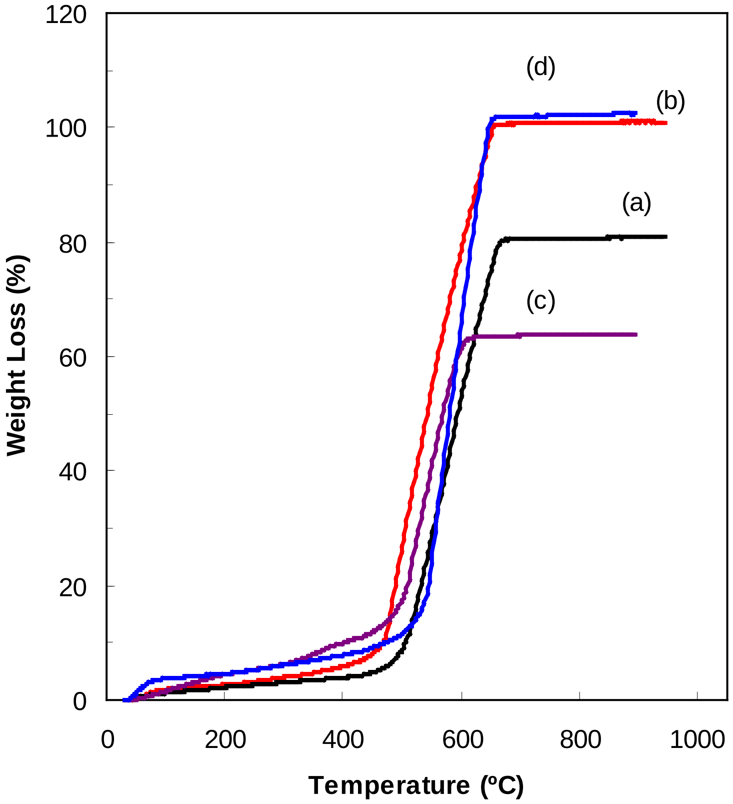

Figure 3.16. Thermal gravimetric analysis of the SCNTs and MWNTs as-prepared and purified in 6M HNO_3 for 2 h under reflux condition: (a) as-prepared SCNTs; (b) purified SCNTs; (c) as-prepared MWNTs; (d) purified MWNTs.

Chapter 4. Novel FeNi Nanoparticle Catalyst for the Production of CO and CO_2-free H_2 and Carbon Nanotubes by Non-oxidative Dehydrogenation of Methane

This Chapter is based on work published as: W. Shen, F.E. Huggins, N. Shah, G. Jacobs, Y. Wang, X. Shi, G. P. Huffman, “Novel FeNi nanopartice catalyst for the production of COx-free H_2 and carbon nanotubes by non-oxidative deyhydrogenation of methane”, *Applied catalysis A: General*, 2008, 351, 102-110. Copyright 2008 Elsevier Ltd.

4.1 Introduction

Hydrogen is envisioned as an ultra-clean energy carrier of the future. Direct, non-oxidative dehydrogenation of hydrocarbons into hydrogen and carbon is an attractive single-step alternation for the producing pure hydrogen and sequestering carbon in the form of a potentially valuable CNTs by-product. In previous work [45, 46, 65], Fe-M (M=Pd, Mo, Ni) bimetallic catalysts on γ-Al_2O_3 supports prepared by traditional incipient wetness method could be used for methane catalytic decomposition. The catalysts lowered the decomposition temperature of methane by 400-500 ºC and achieved ~70-90% conversion of undiluted methane into pure hydrogen and multi-walled carbon nanotubes at 650-800 ºC with a space velocity of 600 $mL\cdot hr^{-1}g^{-1}$. However, the CNTs were very difficult to clean because of the limited solubility of alumina and the strong binding of the CNTs to the support due to the formation of $FeAl_2O_4$ during the reaction. To circumvent this problem, a basic Mg(Al)O support, prepared by calcination of a Mg-Al hydrotalcite-like compound (Mg/Al ratio of 5), was developed as an alternative catalyst support to produce easily purified CNTs and CO and CO_2-free H_2 as described in chapter 3. Ethane dehydrogenation was conducted over a monometallic Ni/Mg(Al)O and a bimetallic FeNi/Mg(Al)O catalyst at three temperatures, 500, 650 and 700ºC. At all temperatures, the carbon was in the form of CNTs and could be easily purified by dilute nitric acid; the purity of the cleaned CNTs is more than 99.5 % [96].

In this research, the catalyst has been further improved by preparing FeNi bimetallic nanoparticles of approximately uniform size and depositing them on the Mg(Al)O support. As discussed below, the FeNi nanoparticles were prepared using thermal decomposition of a mixed metal-surfactant complex in the presence of surfactants and a new nanoparticle impregnation method was used to disperse the FeNi nanoparticles onto the Mg(Al)O support. The resulting nanoparticle catalyst (FeNi np/Mg(Al)O) exhibited significantly higher activity and better time on stream (TOS) behavior than those prepared by the incipient wetness method (FeNi IW/Mg(Al)O).

Much of the interest in nanoscale materials in catalysis is due to the fact that the decrease in the particle size to the nanometer scale generally increases specific surface area and thereby increases the number of active sites and improves the performance of the catalyst. Nanoparticles can be produced either by so-called “top down methods”, i.e. by the mechanical grinding of bulk materials, or via “bottom up methods”, by wet chemistry. Nanoparticles or nanocrystals, due to their very high surface energy, are usually thermodynamically unstable and tend to agglomerate or aggregate to grow in size. In order to form a stable “colloidal metal”, a variety of stabilizers, such as ligands, polymers, copolymers, dendrimers and surfactants, are used to control the growth of particles and prevent them from agglomeration. Many applications of the transition nanometal colloids as homogeneous catalysts have been published and reviewed [97-101]. And they could also be applied to prepare supported heterogeneous catalysts by the nanoparticle impregnation method. The obvious advantage of this novel approach compared with conventional incipient wetness method is that both the size and the composition of the catalyst particle can be pre-adjusted for the specific applications. Researchers in Dr. Bönnemann’s group have developed colloidal Rh/charcoal for hydrogenation and selective partial hydrogenation[102-105], colloidal Pd-Ru/C for methanol oxidation [106] and fuel cell application [107]. These novel catalysts generally showed much better performance compared to conventional catalysts and commercialized catalysts.

With the development of colloidal chemical synthesis over the past decade, uniform-sized and monodispersed nanoparticles (nanocrystals) can be relatively easily obtained by a variety of synthetic methods [108-113] and the cost has been greatly reduced, thus, opening new opportunities for making well-defined nanoscale catalysts. Bae et al.[114] used a reverse micelle technique to first prepare monodispersed Pd nanoparticles, and then combined it with a sol-gel process to prepare a Pd/SiO_2 nanocomposite. Niesz et al. [115] incorporated monodisperse Pt nanoparticles into ordered channels of the high surface area mesoporous oxides such as SiO_2, Al_2O_3 and Ta_2O_5 to form three-dimensional model catalysts. Massard et al. [116] used synthesized core-shell Pd-Ni bimetallic nanoparticles on alumina for selective hydrogenation of 1,3-butadiene. Iijima et al. [117] produced size-controlled Co, Co-Mo, and Fe-Mo nanoparticles by the reverse micelle method and used them as “floating catalysts” for the gas-phase pyrolysis synthesis of single-walled carbon nanotubes (SWCNTs). Monodispersed iron nanoparticles with average diameters of 3 nm, 9 nm, and 13 nm were prepared by thermal decomposition of $Fe(CO)_5$ under the protection of surfactant in octyl ether solution by Cheung et al. [118]. These iron nanoparticles were deposited on the surfaces of oxidized silicon to form substrate-supported nanoparticle catalysts for the production of CNTs. The same approach was also used by Liu et al. [119] for the CVD synthesis of CNTs using monodisperse Fe-Mo bimetallic nanoparticles.

Although there are some applications of nanoparticles in catalysis, the use of supported nanoparticle catalysts as non-oxidative dehydrogenation catalysts to produce H_2 and CNTs has not been reported yet. Here, monodispersed and relatively uniformly-sized $Ni_{35}(Fe_{65})O$ nanoparticles were firstly prepared and well dispersed onto a synthetic Mg(Al)O support to form a novel catalyst, FeNi np/Mg(Al)O. This novel catalyst is evaluated, along with a conventional FeNi IW/Mg(Al)O catalyst prepared by incipient wetness, by various microscopic and spectroscopic techniques, and catalytic performance.

4.2 Experimental

4.2.1 Catalyst Preparation

The preparation of the Mg(Al)O support (Mg/Al = 5) and FeNi IW/Mg(Al)O incipient wetness catalyst, which had an approximate Fe/Ni ratio of 65/35, was described previously in chapter 3. In current work, the monodispersed FeNi oxide nanoparticles were prepared by thermal decomposition of Fe-oleate and Ni-oleate complexes in octadecene under reflux, using method developed by Hyeon's group [120-122] and by Sun and co-workers [123]. In a typical synthesis, 6.5 mmol Fe-oleate complex, 3.5 mmol Ni-oleate complex and 4.4 mmol oleic acid (1/6 equivalent normality of Fe-oleate/Ni-oleate) were mixed with 50 g octadecene. The mixture was first heated to 200ºC for 1 h and then to close to the boiling point of octadecene (thermal meter showed 323°C) for 30 min. The resulting solution was cooled to room temperature and 100 mL propanol was added to precipitate the nanoparticles, which were separated by centrifugation, and then redispersed in 40 mL hexane. Next, the hexane solution was centrifuged again to removal any remaining precipitates. The resulting colloidal mixture of nanoparticles in hexane is highly stable, and the nanoparticles could be separated by addition of ethanol and followed by centrifugation. After thoroughly washed by using ethanol for at least 3 times by adding 10 mL ethanol, the resulting wax-like black precipitate was slowly dried at room temperature for 2 days, weighed and redispersed in hexane for future use.

Fe-oleate and Ni-oleate complex were prepared by iron exchange reaction of $FeCl_3·6H_2O$ and $NiCl_2·6H_2O$ with sodium oleate. In a typical procedure, such as preparation of Fe-oleate, 40 mmol $FeCl_3·6H_2O$ and 120 mmol sodium oleate was added into a mixture of 80 mL ethanol, 60 mL distilled water, 140 mL hexane with vigorous stir for 2 h at room temperature. The mixture has a phase separation and the metal-oleate complex in hexane on the top layer could be easily separated from ethanol and water mixture by using a separation funnel. The resulting metal-oleate in hexane solution was further cleaned by using distilled water for 3 times. After slowly evaporated the hexane and water, the waxy metal-oleate was ready for use.

To prepare the Mg(Al)O supported $Fe_{65}Ni_{35}$ nanoparticle catalyst (FeNi np/Mg(Al)O), the FeNi nanoparticles in hexane were first subject to an ultrasonic homogenization (Omni-Ruptor 250-OMNI International Inc.) for 30 min and the appropriate amount of Mg(Al)O catalyst support powder (<100 mesh) to achieve 5 wt.% metal loading was added to the colloid solution, after which the resulting mixture was ultrasonicated for another 30 min. The FeNi nanoparticles became incorporated into the Mg(Al)O support and the FeNi np/Mg(Al)O catalyst settled on the bottom of beaker. The clear hexane layer was then removed by decanting and slow evaporation at room temperature over one or two days. The resulting catalyst was further dried in an oven at 100°C overnight. This is the as-prepared FeNi np/Mg(Al)O catalyst, with FeNi nanoparticle in the form of an FeNi oxide.

4.2.2 Methane Dehydrogenation Reaction

Methane dehydrogenation was performed with both FeNi np/Mg(Al)O and FeNi IW/Mg(Al)O catalysts in a fixed-bed plug-flow reactor. The reaction chamber was a quartz tube with an inner diameter of 22.5 mm and length of 45 cm. The catalyst was placed at the center of the reactor to form a thin layer of catalyst bed on top of a quartz wool plug. Both catalysts were pre-reduced in situ in 60 mL/min flowing hydrogen; the FeNi IW/Mg(Al)O at 700°C for 2 h, the FeNi nanoparticle catalyst at 600°C for 1 h, with a ramping rate of 10°C/min. The H_2 consumption is about 26.2 mL/gram FeNi IW/ Mg(Al)O and 28.4 mL/ gram FeNi np/Mg(Al)O, assuming idea gas. After reduction, methane dehydrogenation was conducted at 600, 650 and 700°C in undiluted methane at a flow rate of 10 mL/min. The inlet gas flow was controlled by a mass flow controller and the effluent was monitored by a bubble flow meter and analyzed by online gas chromatography (GC) with a thermal conductivity detector (TCD). The solid product was collected after reaction. The gas product was quantified as volume percentage of the total gaseous effluent.

4.2.3 Characterization

X-ray absorption fine structure (XAFS) spectroscopy was conducted at beamline X-19A of National Synchrotron Light Source (NSLS) at Brookhaven National

Laboratory (BNL), Upton, New York. Fe K-edge (7112 eV) and Ni K-edge (8333 eV) XAFS spectra were collected at room temperature in fluorescence mode using a Lytle detector. XAFS data analysis was carried out following well established procedures by means of PC-based XAFS analysis package. XAFS spectra were obtained for the as-prepared FeNi nanoparticles and the FeNi np/Mg(Al)O catalyst in 5 conditions: “reduced/passivated”, “after reaction at 600ºC for 5 h and 48 h, respectively”, “after reaction at 650°C for 5 h”, and “after reaction at 700°C for 5 h”.

Mössbauer spectroscopy was carried out at room temperature using a ^{57}Co(Rh) source. A Halder drive was operated in triangular function mode to scan a ±12 mm/s velocity range. The Mössbauer data for FeNi np/Mg(Al)O catalyst in different conditions as reduced/passivated and after reaction at 600ºC for 2 h, 5 h and 48 h were recorded at room temperature. The Mössbauer spectra were analyzed by least-squares fitting using a computer routine that fits individual iron components as single peak, quadrupole doublets or magnetic sextets. The reduced samples were passivated at room temperature in 1 vol. % O_2 and balance N_2 with a flow rate of 100 mL/min to avoid re-oxidation of FeNi catalyst particle after exposure to air.

Temperature programmed reduction was conducted on both the as prepared FeNi IW catalyst and the FeNi np catalyst in a Zeton-Altamira AMI-200 unit with a thermal conductivity detector (TCD). Argon was used as the reference gas, and 10% H_2 (balance Ar) was flowed at 30 mL/min as the temperature was increased from room temperature to 1100 °C at a ramp rate of 10°C /min. TPR data for the pre-reduced FeNi np/Mg(Al)O catalyst (at 600°C for 1 h with ramping of 10°C /min in 70 vol.% H_2 and 30 vol.% Ar with a flow rate of 50 mL/min) were also recorded from 600°C to 1100°C at a ramp rate of 10 K/min.

High resolution transmission electron microscopy (HRTEM), scanning transmission electron microscopy (STEM), and energy dispersive x-ray spectroscopy (EDS) elemental mapping were conducted using a JEOL 2010F TEM at an accelerating voltage of 200 kV. To prepare the monodispersed FeNi nanoparticle TEM sample, one drop of a dilute FeNi np hexane solution after ultrasonication for 30 min was dropped onto the surface of a carbon coated Cu grid. Hexane was slowly evaporated from the Cu grid by a glass cover. The procedures for preparation of catalysts sample and CNTs sample for microscopy studies are described in detail in chapter 2 and reference [96].

4.3 Results and Discussion

4.3.1 Characterization of the Synthesized FeNi oxide Nanoparticles

Figure 4.1 (a) and (b) present the TEM, HRTEM images of the synthesized FeNi oxide nanoparticles. The nanoparticles are monodispersed and have a very narrow size distribution. The HRTEM image clearly shows that the nanoparticles are single crystal with well-ordered crystal structure. Fe/Ni composition (iron content mol. % of 90, 80, 65, 50, 20, 0) was varied by mixture of Fe-oleate and Ni-oleate with different molar ratio in octadecene. The monodispersed single crystal with uniform size could be synthesized up to the Ni content of 35 mol. %. Further increasing the Ni content to 50 mol. % resulted very sticky precipitate, which could not be redispersed in hexane. The effort was also devoted to synthesize monometallic Ni nanoparticles by this approach. Different solvent was used such as hexadecane (Boiling point (BP) 289°C), octyl ether (BP 302°C) and octadecene (BP 323°C). None of them could generated good Ni particles with relatively uniform size distribution. It may be due to the fact that single surfactant oleic acid alone could not provide strong enough binding to prevent the agglomeration of Ni nanoparticles during the growth step [124, 125]. Ni nanoparticles have a much active surface than Fe nanopartices. However, less content of Ni incorporated into Fe lattice could be stabilized in this system. Adding more oleic acid up to equivalent normality of Fe-oleate/Ni-oleate and the combination of oleic acid (equivalent normality) and oleylamine (equivalent normality) have no effect on tuning both particle size and particle shape of FeNi oxide nanopartices (See figure 4.1(c) and (d)). Figure 4.2 presents the particle size distribution (PSD) which was obtained based on several hundreds of particles. The PSD is tightly clustered around a mean particle size of 9 nm.

Figure 4.3 shows the XRD pattern of the synthesized FeNi nanoparticle as well as the XRD patterns of standard fcc-structured NiO, FeO and the calculated $Ni_{35}(Fe)_{65}O$ by using a PC-based software of Atoms. The calculation was based on the assumption that the Ni and Fe with molar ratio of 35:65 were randomly distributed into the octahedral sites of face-centered cubic metal oxide (MO). It is seen that the synthesized FeNi nanoparticle contains a single phase with fcc structure and the pattern matches well the calculated $Ni_{35}(Fe)_{65}O$, not only the position of reflection peaks, but also the ratio of the peak height. The average particle size calculated from principle reflection peaks (face 200, 220) by using Debye-Sherrer equation is close to 9 nm, consistent with the TEM observation. The k^3-weighted EXAFS and the Fourier transformation of the k^3-weighted EXAFS (radial structure function (RSF)) of the synthesized FeNi nanoparticles in both Fe K-edge and Ni-K-edge are shown in figure 4.4. The results of nickel oxide are also included as reference. Except for the discrepancy of the intensity, Fe k-edge and Ni k-edge spectra of k^3-weighted EXAFS and RSF of the synthesized FeNi nanoparticles are very similar, indicating a similar coordination environment like in the fcc-structured NiO. Room-temperature Mössbauer spectrum in figure 4.5 of the synthesized FeNi oxide nanoparticle exhibits that irons are in the ferrous and ferric state. The fitting parameters are listed in table 4.1. From the above characterizations, it is concluded that the synthesized FeNi nanoparticles have fcc structure with ordered vacancies. It is a non-stoichiometric FeNi oxide with formula:

$$(Fe_{0.14}^{2+}Ni_{0.28}^{2+})(Fe_{0.40}^{3+}V_{0.18})O$$

Where, V is the vacancy.

4.3.2 Microscopic Studies of FeNi Bimetallic Catalysts

Figure 4.6 shows the STEM images of the as-prepared FeNi nanoparticle catalyst. The FeNi nanoparticles were evenly distributed onto the surface of the Mg(Al)O support by nanoparticle impregnation method. However, there are no obvious particles observed in the as-prepared FeNi incipient catalyst as seen in chapter 3. Most of Fe and Ni are cooperated into the Mg(Al)O support lattice.

Figure 4.7 emphasizes the differences between the reduced FeNi IW/Mg(Al)O catalyst and the reduced FeNi np/Mg(Al)O nanoparticle catalyst observed in STEM and TEM studies. The FeNi IW/Mg(Al)O was reduced at 700°C for 2 h and the FeNi np/Mg(Al)O catalyst was reduced at 600°C for 1 hr, both in undiluted hydrogen at a flow rate of 60 mL/min; the temperature ramping rate was 10 K/min. The TEM results for the FeNi IW/Mg(Al)O were reported in chapter 3. The Mg(Al)O support of the FeNi IW/Mg(Al)O catalyst reduced at 700ºC for 2 h has experienced significantly more sintering than the support for the FeNi np/Mg(Al)O catalyst reduced at 600ºC for 1 h. This is confirmed by the BET surface areas of the reduced IW catalyst (84 m^2/g), the as-prepared Mg(Al)O support (154 m^2/g), and the reduced nanoparticle catalyst (146 m^2/g). The STEM image of the reduced FeNi IW/Mg(Al)O in Figure 4.7a shows considerably larger metallic nanoparticles than those in the reduced FeNi np/Mg(Al)O catalyst in figure 4.7b. The FeNi catalyst nanoparticles, which are prepared in advance with uniform size, are more evenly dispersed on the Mg(Al)O support and show less agglomeration or sintering after thermal treatment in the H_2 atmosphere. In contrast, the FeNi IW/Mg(Al)O catalyst exhibits a broad size distribution, from very tiny particles less than 8 nm in size to large particles about 50 nm. The TEM image in figure 4.7c shows the FeNi nanoparticles dispersed on Mg(Al)O nanocrystals of about 9 nm size, but it is difficult to distinguish the catalyst particles from the support particles. The high magnification HRTEM image of figure 4.7d shows the lattice fringe arising from the catalyst support and/or the FeNi nanoparticles.

Figure 4.8 shows STEM image and corresponding EDS x-ray elemental mapping of Fe and Ni over the reduced FeNi IW/Mg(Al)O and FeNi np/Mg(Al)O catalysts. It is seen that the FeNi alloy composition with the FeNi IW/Mg(Al)O catalyst derived from its normal 65/35 Fe/Ni ratio, ranging from Fe rich to Ni rich, indicated in figure

4.8a.This results are consistent with ^{57}Fe Mössbauer results reported in chapter 3. In contrast, Fe and Ni location coincide with the reduced FeNi np/Mg(Al)O catalyst as shown in figure 4.8b, confirming the formation of an FeNi alloy. The Fe/Ni EDS peak height ratio in any selected area is always close to 65/35, indicating that FeNi nanoparticle maintain their original composition after reduction.

4.3.3 Temperature Programmed Reduction

Figure 4.9 shows the TPR profiles for the as-prepared FeNi IW/Mg(Al)O, the FeNi np/Mg(Al)O, and the pre-reduced FeNi np/Mg(Al)O catalysts. The TPR profile for the FeNi IW/Mg(Al)O catalyst (curve “c” in figure 4.9) has two broad peaks, one ranging from 360°C to 580°C and the second from 750°C to 1100°C, indicating two distinct metal-support interactions in the IW catalyst. The broad, low-temperature peak with less hydrogen consumption may be caused by the reduction of the FeNi oxide on the surface of the catalyst. The broad reduction peak at higher temperatures indicates a stronger metal-support interaction, consistent with Fe and/or Ni that are well dispersed in the Mg(Al)O lattice, as documented in chapter 3. The experimental reduction conditions (700°C for 2 h) are not sufficient to reduce all the iron as only 20% of the Fe is in metallic form with the rest bound to the Mg(Al)O support by means of oxygen anions.

The TPR profile for the as-prepared FeNi np/Mg(Al)O catalyst (curve “a” in figure 4.9) is clearly different from that of the IW catalyst. This profile combines the reduction of the FeNi nanoparticles and the release of the protective surfactant shell around nanoparticles at elevated temperatures. The formation of an organic shell surrounding synthetic nanoparticles has been previously recognized and accepted widely. This shell provides chemical stability to reactive transition metals and acts as a tunable spacer to prevent magnetic coupling between adjacent particles. Thermal decomposition of surfactant coatings on Co and Ni nanocrystals was studied by Pérez-Dieste et al. Two processes were involved: partial desorption of the surfactant at about 200°C (the boiling point of oleic acid is 194-195ºC) and dehydrogenation at higher temperatures around 400°C. From the TPR profile of the FeNi nanoparticle catalyst, it seems that FeNi nanoparticles start to reduce at 300°C and complete at the temperature of around 750°C, even though they may be protected by the organic coating. The onset of the drop at around 400°C coincides with the temperature of dehydrogenation of the surfactant coating. No signal change was observed below 300°C in our TPR condition, which may be due to the fact that partially desorbed surfactant shell was captured by a liquid N_2 trap before the TCD detector. There is no extra reduction peak shown up for the pre-reduced FeNi np/Mg(Al)O catalyst (curve “b” in figure 4.9), indicating that the catalyst was fully reduced under the experimental reduction conditions.

In order to better understand the reduction process, the same reduction (600ºC for 1 h at a ramp rate of 10ºC/min) was conducted with the FeNi nanoparticles deposited on a carbon coated Cu grid. The TEM images of these reduced FeNi nanoparticles are shown in figure 4.10. The hexane dispersed FeNi nanoparticle deposition on carbon surface generates a thin organic film, where the FeNi nanoparticles self-assemble in the film to form a monolayer. Figure 4.10a shows the clear boundary of the film, where FeNi nanoparticles are self-assembled inside the boundary. Figure 4.10b shows the nanoparticles are stabilized and separated by the surfactant film, even after H_2 treatment at 600°C. Careful examination reveals the formation of a shell on the monodispersed nanopartices in figure 4.10c, which may due to the re-oxidization of reduced FeNi nanopartices after exposure to air.

4.3.4 Methane Dehydrogenation

Methane is the most abundant gaseous alkane, containing 25% by weight of hydrogen, the highest H/C ratio of hydrocarbons. Methane dehydrogenation (4-1) is a mildly endothermic reaction and favored at high temperature above ~600ºC to achieve a reasonable conversion.

$$CH_4 \rightarrow C + 2H_2 + 74.5 kJ/mol \qquad (4\text{-}1)$$

The equilibrium conversion of methane was calculated by Ogihara et al. [40] based on the assumption that all carbons formed are graphite. At 700, 650 and 600ºC the equilibrium conversion of methane is ~75%, ~65% and ~60%, respectively. And the methane conversion could be calculated based on the amount of H_2 generated as equation 4.2:

$$C_{CH_4} = \frac{H_2 vol.\%}{200 - H_2 vol.\%} \times 100\% \qquad (4\text{-}2)$$

Where C_{CH_4} is methane conversion and H_2 vol.% is the hydrogen volume percentage in the gas effluent.

Methane dehydrogenation was conducted in a fixed-bed plug flow reactor with a methane flow rate of 10 mL/min. Before reaction, both the FeNi IW/Mg(Al)O and FeNi np/Mg(Al)O catalysts were activated by programmed reduction in hydrogen. The methane dehydrogenation performance of these two pre-reduced catalysts is compared in figure 4.11. Figure 4.11a shows the time-on-stream (TOS) H_2 production over the novel FeNi np/Mg(Al)O catalysts at three temperatures, 600, 650 and 700ºC, with total catalyst loading of 0.2 gram. At 600ºC, the catalyst maintained its catalytic activity for at least 5 h, yielding over 50 vol.% of H_2 in effluent gas. Upon increasing the temperature to 650ºC, the H_2 volume percentage in effluent increases to 66%. The catalyst maintained its activity over 2 h, then gradually deactivates. Further increasing the temperature to 700ºC, methane conversion is not improved and the catalyst deactivates rapidly. It should be noted that non-catalytic methane decomposition begins at approximately 900ºC does not reach a level of 50% untill the temperature approaches 1100ºC. Figure 4.11b exhibits the catalytic behavior of FeNi IW/Mg(Al)O catalysts at 600, 650 and 700ºC with total catalyst loading of 1 gram, 5 times that of the novel catalysts. The FeNi IW/Mg(Al)O catalyst exhibits hydrogen yield of about 30 vol.% at 600ºC and is fairly stable. At 650ºC, the hydrogen concentration in effluent starts at 50 vol.% and decreases steadily over a period of 6 h to 25 vol.%. At 700ºC, the activity and the stability of the FeNi IW/Mg(Al)O catalyst are similar to those of FeNi np/Mg(Al)O catalyst, decreasing rapidly from about 60 vol.% of hydrogen to a low level. The TOS methane conversion trends for the two catalysts at 600ºC and 650ºC is shown in Figure 4.12. It is clearly seen that FeNi np/Mg(Al)O catalyst shows much higher methane conversion at both reaction temperature than that of FeNi IW/Mg(Al)O catalyst despite of the much less catalyst loading. The net H_2 production within 5 h reaction over FeNi np/Mg(Al)O and FeNi IW/Mg(Al)O based on 0.2 gram of catalyst loading at the reaction temperatures of 600, 650 and 700ºC is 2289 mL, 1694 mL, 348 mL and 226 mL, 332 mL, 162 mL, respectively.

Methane dehydrogenation reaction to produce CO_x-free H_2 and filamentous carbon has been well documented over supported Ni catalyst. However, Ni catalysts for this reaction can not bear the higher temperature above 600ºC [19, 20, 23, 126]. At a low reaction temperature, the methane conversion can not be expected to be high, even though the Ni-based catalyst has a relatively longer life time compared with the monometallic Fe catalysts, which could be used at high temperatures above 1000ºC. But the main difficulty posed by the Fe-based catalysts is the short life-time. Addition of Ni to Fe can improve the performance of the catalyst at a higher temperature. Here, both bimetallic FeNi catalysts can keep certain activity for a reasonable time, especially for the nanoparticle catalyst, it can keep high methane conversion for 2 h in a steady-state operation at 650ºC. However, the FeNi catalyst with Fe to Ni of 65 to 35 seems not to behave well above 700ºC as both incipient catalyst and nanoparticle catalyst deactivate very quickly. Therefore, the FeNi bimetallic catalyst over the Mg(Al)O support are suitable for methane dehydrogenation at moderate temperatures.

The improved stability of the FeNi np/Mg(Al)O catalyst is better illustrated by figure 4.13, which shows the TOS hydrogen production for 0.5 g loading of the FeNi np/Mg(Al)O catalyst at 600ºC. At this 2.5 times higher catalyst loading, hydrogen production is fairly steady for the first 12 h, declining very slowly from about 58 to 50 vol.% (0.67 % / (hr•g catalyst)) and somewhat more rapidly (1.7 % / (hr•g-catalyst)) in the next 36 h.

4.3.5 TEM Studies of the Reacted FeNi np/Mg(Al)O Catalyst

The carbon products were collected after reaction and studied by TEM. Figure 4.14 shows the morphologies of the CNTs generated at 600ºC from methane dehydrogenation over FeNi np/Mg(Al)O catalyst. The carbon products are in the form of bamboo-like multiwalled carbon nanotube (B-MWNT), with mm-scale length, tangling together, forming a very sinuous material with BET surface area of approximate 400 m^2/g. The generated CNTs have a relatively uniform outer diameter of ~15 nm and an inner diameter of 6-8 nm, this latter dimension is just slightly smaller than the mean size determined for the catalyst nanoparticles. The interplanar distance of the concentric graphite sheets of the MWNTs is 0.34-0.35nm. Numerous nanoparticles are observed inside the CNTs, often at the tips of CNTs with the coverage of two or three layers of graphite sheets, indicating a tip growth mechanism. The carbon yield is 285 mol carbon/mol FeNi at 600ºC and 216 mol carbon/mol FeNi at 650ºC. However, the carbon yield at 700ºC is very low, only 32 mol carbon/mol FeNi. At 650ºC and 700ºC, the structure of CNTs is also in the form of B-MWNT with same outer diameter. However, the CNTs generated at 700ºC are very short compared with those at lower temperatures. It is widely accepted that the diameters of carbon filament (CNTs or carbon nanofibers (CNFs)) are strongly dependent on the size of catalyst particles [118, 127]. The approximately monosized FeNi nanoparticles of the novel FeNi np/Mg(Al)O catalyst lead to a relatively narrow size distribution of the generated CNTs, while the carbon product from methane dehydrogenation over FeNi IW/Mg(Al)O catalyst exhibits a broad size distribution because of the broader distribution of catalyst particle size. The carbon yield at 600ºC over the FeNi IW/Mg(Al)O catalyst is 106 mol C/mol FeNi, which is much lower than that of FeNi np/Mg(Al)O catalyst at the same reaction conditions.

Figure 4.15 shows the morphologies of the FeNi nanoparticles after reaction for 5 h at 600 and 700ºC, respectively. No sintering or agglomeration of the FeNi nanoparticles is observed at either reaction temperatures. Each nanoparticle serves as an active site for growing CNTs. Deactivation likely occurs because the active FeNi nanoparticles become increasingly encapsulated by graphitic carbon. Some FeNi nanoparticles are extruded along the inner walls of the CNTs (Figure 4.15b) and may function as active sites for the formation of longer MWNT. The deformation observed for some of the nanoparticles within the nanotubes may be caused by diffusion of carbon in the FeNi nanocrystals [35, 128].

The nucleation and formation of graphite requires catalytic active sites. Since the nanoparticle catalyst contains individual reduced FeNi nanoparticles as catalytic active sites, stabilized by surfactant film after reduction at 600ºC, it facilitates the nucleation of carbon, whereas, promotes the methane dehydrogenation reaction. On the other hand, the FeNi IW/Mg(Al)O catalyst can be only partially reduced and the reduced IW catalyst may generate larger FeNi particles size, some in the range of 20-40 nm. Moreover, the catalyst experienced significant sintering during the pre-reduction and the methane dehydrogenation reaction because only the metal-support interaction without the protection of surfactant can not stabilize the FeNi particles at high operating temperatures. Compared with the FeNi IW/Mg(Al)O catalyst, the FeNi np/Mg(Al)O catalyst has much more catalytic active sites with the same FeNi loading, thus contributing to the longer lifetimes and higher methane conversion.

4.3.6 Mössbauer, XAFS spectroscopic Characterization

Figure 4.16 shows the Mössbauer spectra collected at room temperature for FeNi np/Mg(Al)O catalyst in the as reduced/passivated state and after reaction at 600ºC for 2 h, 5 h and 48 h. The spectra change significantly with TOS of methane dehydrogenation reaction. The reduced/passivated sample shows a doublet with an isomer shift (IS) of 0.32 mm/s and a quadrupole splitting (QS) of 0.84 mm/s, a magnetic sextet with an IS of 0.01 mm/s and a hyperfine splitting H_0 of 275 kG, and an ill-defined absorption with an IS of 0.24 mm/s and QS of 3.91 mm/s. The first doublet can be assigned to superparamagnetic nanoparticle ferric oxide formed on the surfaces of the reduced catalyst particles after they were exposed to air. Even though, it is possible that the complete reduction to the metallic state may not have been achieved in the reduction step, all of the iron should have been reduced at least to the ferrous state. Consequently, the observed ferric iron must present re-oxidized iron. The magnetic component can be attributed to the fcc structured $Fe_{65}Ni_{35}$ nanoparticles, which likely form an invar-like alloy with coexisting ferromagnetic and superparamagnetic regions [129-132]. These latter regions would give rise to the third absorption feature; however, the superparamagnetic ferric oxide particle may also contribute to this feature as well. The spectra became more complicated after the FeNi alloy particles are reacted with methane and carbon is introduced into the Fe-Ni alloy lattice. The ferric oxide still constitutes about 25 – 30% of the iron. However, the magnetic component increases in intensity and is better ordered magnetically (smaller superparamagnetic component) presumably due to the incorporation of significant amounts of interstitial carbon in the fcc Fe-Ni-C alloy resulting in concomitant recrystallization and some crystal growth. The deactivated catalyst shows a very different spectrum from the catalytically active samples. It exhibits a sharp singlet and a doublet with an IS of 0.19 mm/s, which we assign to paramagnetic Fe-Ni-C austenite and a broad sextet due to remnant Fe-Ni-C invar alloy. The doublet due to superparamagnetic ferric oxide is now absent presumably because the Fe-Ni-C nanoparticles have become encased in the nanotubes, which prevents oxidation at the particle surfaces after the reaction. As suggested above, carbon encapsulation may prevent methane access to the nanoparticle catalysts, resulting in deactivation.

The conclusions regarding the catalyst structure reached from the Mössbauer data are supported by results from Fe and Ni K-edge x-ray absorption fine structure (XAFS) spectroscopy. Figure 4.17 shows the Fe and Ni K edge x-ray absorption near edge structure (XANES) spectra for the FeNi np/Mg(Al)O catalyst as reduced/passivated and reacted conditions labeled as: (a) Fe stainless steel (SS) foil or Ni foil as references, (b) the reduced sample, (c), (d) are the reacted catalysts at 600ºC after 5 h, but still active and 48 h, completely deactivated. The references Fe SS foil and Ni foil have typical fcc structure. Fe SS foil has a pre-edge peak at 7117 eV, two small peak at 7130 eV and 7137eV, and a broad peak at 7160eV. Ni foil has three remarkable peaks at 8350 eV, 8358 eV and 8383 eV, respectively, and a pre-edge peak at 8336 eV, reassembling that of fcc structured Fe SS foil. The deactivated catalyst (d) both in Fe K-edge and Ni K-edge XANES spectra reassemble that of fcc structured metal foil. The XANES spectra seem identical for all the deactivated catalyst samples after reaction at 600ºC, 650ºC and 700ºC. In the Fe K edge XANES spectrum, the reduced catalyst (b) and used catalyst (c) show only a broad peak at 7134 eV instead of two split peaks at 7130 eV and 7137 eV of Fe SS foil and the totally deactivated catalyst (d). But the third broad peaks at 7162 eV are present in all the samples despite of the lower intensity of (b) and (c) compared with the deactivated samples. The same result is also observed in the Ni K edge XANES spectrum. The reduced sample has a white line at 8353 eV, a shoulder at 8358 eV and a broad low intense peak at 8383 eV. The used sample (c) still has these features, but the white line has already split into two obvious peaks. The differences between the reduced/passivated catalyst (b), the used but still active catalyst (c) and the totally deactivated catalyst (d) indicate some degrees of oxidation existed in the catalytically active catalyst samples, in agreement with the results from Mössbauer spectroscopy. In both the Fe K-edge and Ni K-edge XANES spectra, the intensity of two low energy peaks is much lower than that of metal foil, which may be due to the small catalyst particle size [133]. And, the third broad peak in all catalyst samples slight shifts to the higher energy level of 7162 eV in Fe XANES spectra and lower energy level of 8352 eV in Ni XANES spectra, which may be caused by the formation of FeNi fcc structured alloy.

The Fourier transforms (FT) of k^3-weighted extended X-ray absorption fine structure (EXAFS) spectra (k in the range of 3 to 15 $Å^{-1}$) of reduced and reacted FeNi np/Mg(Al)O catalysts are shown in figure 4.18 and compared with those obtained from a stainless steel foil and a Ni foil. The FT of the catalyst samples are similar, exhibiting four well-defined shells of at 2.2 Å, 3.3 Å, 4.0 Å and 4.7 Å, and thereby confirm the fcc structure of the metallic alloy phase. However, the peaks derived from the more distant neighbor shells (above 3.3 Å) are significantly weaker relative to the nearest neighbor peak than the corresponding peaks observed in the FT of the Fe SS or Ni foil. This is especially true for the catalytically active samples (b) and (c). Such effects may result from the mixture of Fe and Ni next-nearest neighbors in the alloy phase, or from small-particle size phenomena, or from a combination of both factors.

In order to understand the local structure of the FeNi catalyst particle, a least squares fitting of the first neighbor shell of reduced and used catalyst samples was conducted by using FEFF EXAFS method available in the SixPack software package [79, 80]. The fitting was performed over the range 1-3Å in R space and 3-13$Å^{-1}$ in k space, using a Kaiser-Bessel FT window. Since γ-Fe and Ni have similar local structures, lattice parameters (Fe: 3.59Å and Ni: 3.52Å) and atomic numbers, XAFS can not differentiate the Ni-Ni bond from the Ni-Fe bond in the first shell fitting. Here, we used the Ni FEFF parameter and γ-Fe FEFF parameter generated by ATOM and FEFF 6 in IFEFFIT software package to fit for the Fe and Ni FTs of EXAFS spectra, respectively and get fitting parameters of the Ni-M and Fe-M bond in the first shell as was done elsewhere [134, 135]. For the active catalyst (b) and (c), the single scattering FEFF parameter of NiO and Fe_2O_3 were also added to extract the coordination number (CN) of Ni-O and Fe-O. Before starting the fitting procedure, the scattering amplitude factor, So^2, was estimated from the first shell fitting of Ni foil collected at the same experimental conditions by fixing the CN to 12. This value of So^2 ($CN \times So^2 = 0.85$) was used in analysis to determine the first metal shell of the catalyst samples. The RSF of the reduced and used nanoparticle catalyst samples and the first shell fitting in both Fe K-edge and Ni K-edge are shown in figure 4.19. The fitting parameters for the first shells in the Fe-Ni-C invar and austenitic alloy and the oxide surface coating are presented in Table 4.2.

The first shell radial distance, R, of Ni-M (M=Fe or Ni) and Fe-M is 2.53Å and 2.50Å, respectively. These results are consistent with those reported in a published study of Fe-Ni alloy films of similar composition [37]. The Debye-Waller factor (σ^2) values are in the range of $6\text{-}7\times10^{-4}$ ($Å^2$), close to values reported in the literature [136, 137]. The deactivated catalyst sample (d) shows the same CN of Ni-M and Fe-M bond in the first shell, indicating the random distribution of Ni and Fe in the catalyst particles[134], in agreement with the elemental distribution maps of the reduced FeNi np/Mg(Al)O catalyst shown in figure 4.8. The first shell M-M CN determined from both the Ni and Fe EXAFS fitting is ~9.5, which is significantly smaller than that, 12, of the bulk material. This difference in CN could be due to either small-particle effects or self-absorption phenomena or a combination of both factors.

In addition to the M-M shells, the spectra for sample (b) and sample (c) also exhibit small M-O peaks, presumably due to surface oxide formed by exposure of the FeNi nanoparticles to air after the reduction and dehydrogenation experiments. The FEFF-derived Ni-O distance is ~2.05Å, close to that of NiO at 2.08Å, and the distance for Fe-O is ~1.93 Å, similar to a typical Fe-O distance in Fe_2O_3 of 1.94Å. The formation of iron oxide instead of nickel ferrite by high-temperature oxidation of Fe-Ni alloy film (Fe 64%, Ni 36%) was confirmed by Tomellini et al. [138] by using in-situ XAS. Here, the separate formation of Fe_2O_3 and NiO after exposure the reduced FeNi nanoparticles are consistent with that report. In sample (b), the CN of Fe-M is smaller than that of Ni-M, meanwhile, the CN of Fe-O is larger than Ni-O, indicating that Fe is easier to be re-oxidized than Ni after exposure to air. Furthermore, the NiO or Fe_2O_3 are formed only on the surface of Fe-Ni alloy particles because both have a very small coordination number, ~3 versus standard 6. This is consistent with the previous TEM observation of core-shell structured nanoparticles formed after reduced/passivated on C coated Cu grid. There is no significant metal-oxide observed in the deactivated samples, d, indicating that FeNi particles are likely encapsulated by carbon generated during methane dehydrogenation, preventing exposure of O_2 to the surface of FeNi particles. This is consistent with the conclusion based on TEM and Mössbauer results that the deactivation of the FeNi nanoparticle catalyst during methane dehydrogenation is due mainly to carbon encapsulation.

There is much discussion on the role of metal carbide in the growth of CNTs. On the one hand, metal carbides, such as Fe_3C, have 10^4 times lower diffusion coefficient of carbon than austenite [139], slowing the diffusion of carbon through catalyst particle, thereby, halting the reaction. On the other hand, the formation of carbide, especially meta-stable carbides, is able to enrich carbon on the surface of catalyst particle, which in turn, increases the driving force for the carbon diffusion, promoting the reaction [89]. Apparently, the catalyst deactivation is due to the loss of catalytic surface by encapsulation of carbon. What the reason might be for the cessation of carbon precipitation to form CNTs, instead, accumulates on the catalyst surface is still debateable. It may be caused by the formation of some forms of stable carbide due to the oversaturated carbon in solution [38]. The observation of austenitic Fe-Ni-C alloy in the deactivated catalysts may be explained by slowly cooling the oversaturated carbon in Fe-Ni solid solution to room temperature [38]. However, Baker et al. [140, 141] presented another deactivation mechanism in their study of the Fe-Ni (Ni-rich) alloy powder for carbon product by using ethylene-H_2 or CO-H_2. At the reduction condition, Ni preferentially segregated onto the surface of FeNi alloy at elevated temperature above 700ºC. Because Ni catalyst can only bear a relatively low temperature, the catalyst lost its catalytic activity very quickly. However, when lowered the reaction temperature, the excess Ni on the surface migrated back into bulk. Therefore, the deactivated catalyst could recover its catalytic activity. Since the segregation of Fe-Ni alloy is a dynamic and equilibrium process, depending on the temperature and reaction time, we can not observe this segregation by ex-situ EXAFS data at room temperature. But, this definitely could become another possible reason for the deactivation, especially when the catalytic performance at higher temperature 700ºC was considered over this novel catalyst, which shows a very quick deactivation. In the future, an in-situ EXAFS experiment is necessary to be designed in order to get more information of the deactivation mechanism.

4. 4. Summary and Conclusions

An FeNi nanoparticle catalyst supported on Mg(Al)O has been prepared by a novel nanoparticle impregnation method. Thermal decomposition of a metal-surfactant complex was initially used to prepare approximately monosized FeNi oxide nanoparticles with a mean size of 9 nm. These nanoparticles were then dispersed onto a high surface area Mg(Al)O support and reduced in hydrogen at 600ºC for 1 h. The resulting FeNi np/Mg(Al)O catalyst exhibited significantly better activity and stability than a similar catalyst with the same metal loading (5 wt.%) prepared by a conventional incipient wetness method (FeNi IW/Mg(Al)O) for catalytic dehydrogenation of methane at moderate temperatures of 600-650ºC. TEM studies showed that the monodisperse FeNi nanoparticles were well dispersed on the surface of the Mg(Al)O support with the particles maintaining a size close to 9 nm. Energy-dispersive X-ray spectra and X-ray mapping indicated a uniform concentrations of Fe and Ni in the particles, with an Fe:Ni ratio of approximately 65:35.

Analysis of XAFS spectra and Mössbauer spectra established that the reduced nanoparticles are fcc structured FeNi alloys with a random distribution of Ni and Fe. During reaction with methane at 600-650ºC, the nanoparticles are converted to an fcc Fe-Ni-C alloy of the invar type that is active for dehydrogenation and formation of CNTs. TEM studies indicated that each nanoparticle functioned as an active site for methane dehydrogenation and CNTs growth in a tip growth mode. The resulting CNTs generated were in the form of bamboo-structured multi-walled nanotubes (B-MWNT) with a narrow size distribution, reflecting the tight size distribution of the FeNi nanoparticles. Deactivation of the catalyst likely results from encapsulation of the nanoparticle catalysts in the MWNTs that prevents access of the methane to catalyst particle surfaces. The associated transformation of the active invar Fe-Ni-C phase to an austenitic phase observed by the Mössbauer spectra collected at room temperature may also be contributing to deactivation.

Table 4.1. Mössbauer Parameters of the as-prepared FeNi nanoparticle and the FeNi np/Mg(Al)O catalysts in their reduced/passivated and used states.

Items	I. S. mm/s	Q. S. mm/s	Width mm/s	H_0 KGauss	%Fe	ID
As-prepared FeNi nanoparticle	0.34	0.63	0.53		73.5	Fe^{3+} oxide
	0.9	1.08	0.73		24	Fe^{2+} oxide
	0.84	1.99	0.27		2	Fe^{2+} oxide
			FeNi np/Mg(Al)O			
Reduced/passivated	-0.57		0.41		2	??
	0.32	0.84	0.82		31	Fe^{3+} oxide
	0.24	3.91	3.58		45	Fe^{3+} oxide (SPM)
	0.01		0.97	275	22	Fe-Ni alloy
2 h reaction at 600ºC	0.24	0.89	0.92		27	Fe^{3+} oxide
	0.05	1.51	0.23		2	Fe-Ni
	0,07	4.64	1.91		22	Fe-Ni
	0.01	0	1.16	277	49	Fe-Ni
5 h reaction at 600ºC	0.3	0.79	0.77		30	Fe^{3+} oxide
	0.43	2.39	0.77		7	Fe^{3+} oxide
	0.05	0	0.73	292	31	Fe-Ni
	0.09		1.13	261	32	Fe-Ni
48 h reaction at 600ºC	-0.08		0.31		18	Fe-Ni (austenite)
	0.19	0.82	0.97		37	Fe-Ni-C
	0	1.03	0.76	288	45	Fe-Ni

Table 4.2. Structural parameters of the FeNi np/Mg(Al)O catalyst with different conditions obtained by FEFF6 fitting of Fe K edge and Ni Kedge FT of EXAFS spectra.

Item	Bond type	N	R (Å)	σ^2(Å^2)
		Ni K edge		
600ºC				
(b) t=0 h	Ni-M	7.7±0.3	2.53±0.00	0.0071±0.0002
	Ni-O	2.6±0.7	2.05±0.05	0.004±0.002
(c) t=5 h	Ni-M	9.0±0.5	2.53±0.00	0.0068±0.0004
	Ni-O	2.9±0.7	2.04±0.03	0.008±0.002
(d) t=48 h	Ni-M	9.5±0.4	2.53±0.00	0.0064±0.0003
		Fe K edge		
600ºC				
(b) t=0 h	Fe-M	5.9±0.6	2.51±0.01	0.0070±0.0007
	Fe-O	3.5±1.2	1.93±0.03	0.0070±0.0004
(c) t=5 h	Fe-M	7.8±0.5	2.50±0.00	0.0070±0.0004
	Fe-O	3.3±0.4	1.93±0.01	0.0020±0.0003
(d) t=48	Fe_M	9.6±0.5	2.50±0.00	0.0065±0.0004

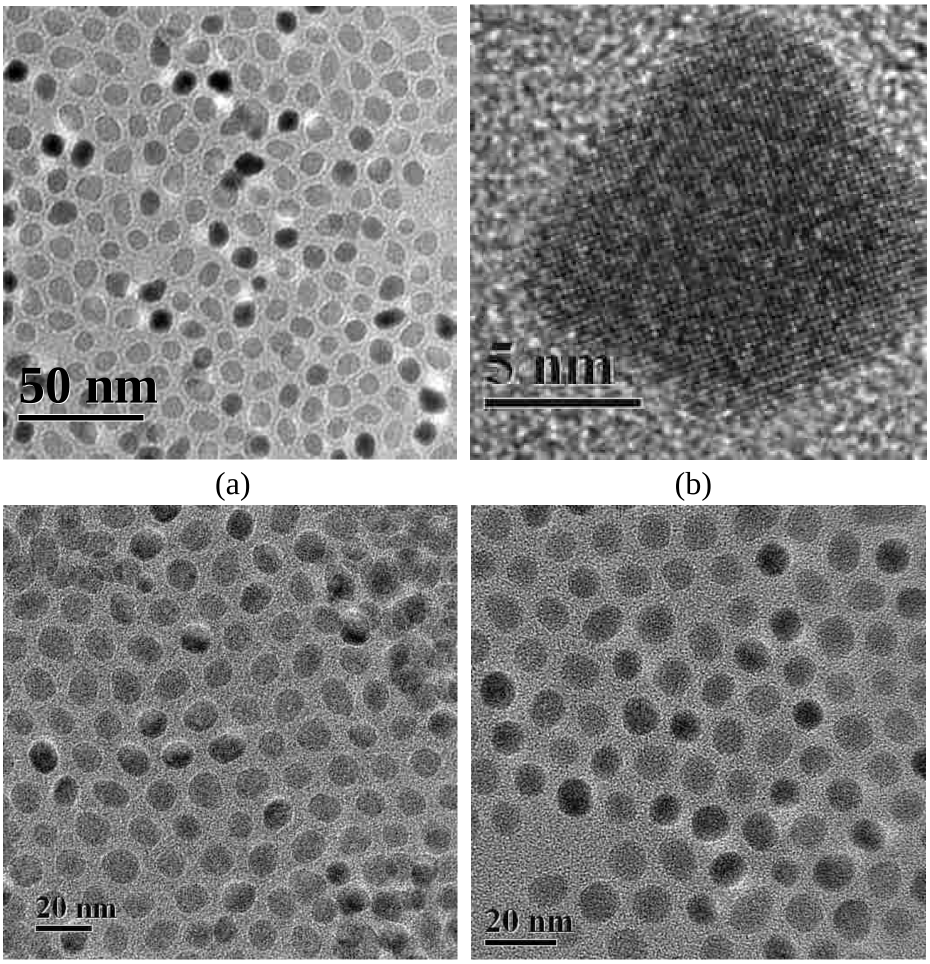

(a) (b)

(c) (d)

Figure 4.1. TEM (a) and HRTEM (b) images of approximately mono-sized FeNi bimetallic nanoparticles prepared by using 1/6 equivalent normality of oleic acid; (c) equivalent normality of oleic acid; (d) combination of equivalent normality of oleic acid and equivalent normality of oleylamine.

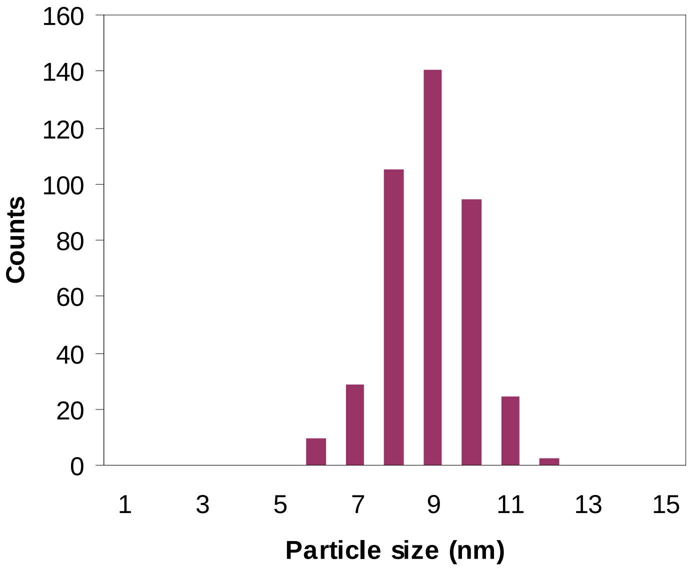

Figure 4.2. Particle size distribution (PSD) of synthesized FeNi bimetallic nanoparticles

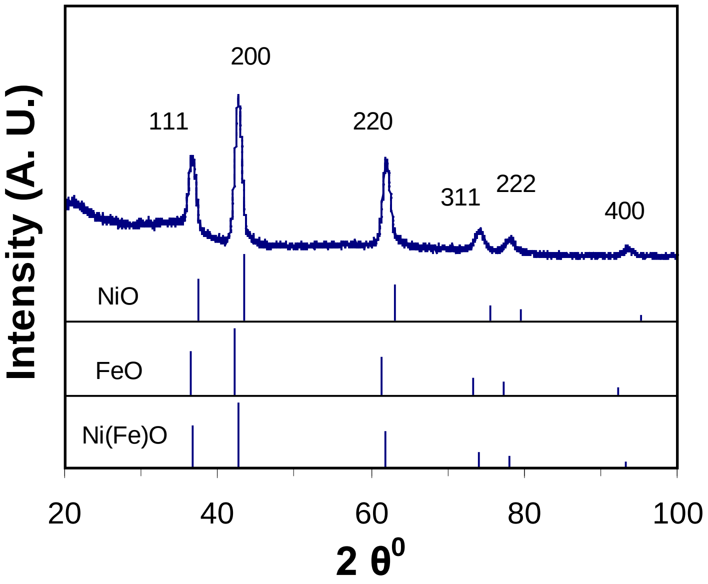

Figure 4.3. X-ray diffraction pattern of the synthesized FeNi nanoparticle, NiO, FeO and Ni(Fe)O as references.

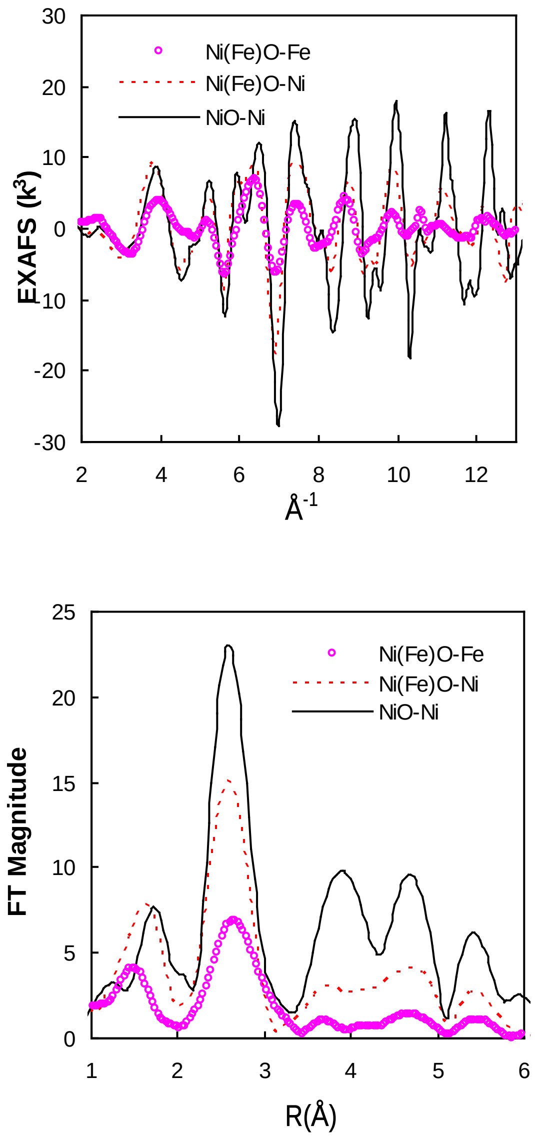

Figure 4.4. K^3-weighted EXAFS and radium structure function (RSF) of synthesized bimetallic FeNi nanoparticles both at Fe K-edge and Ni K-edge

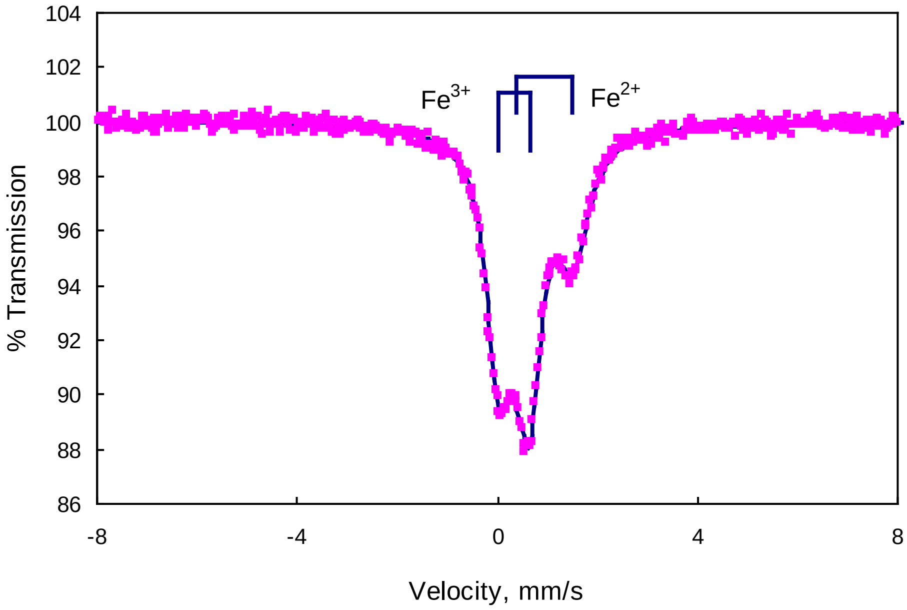

Figure 4.5. Room-temperature Mössbauer spectrum of the synthesized FeNi nanoparticle

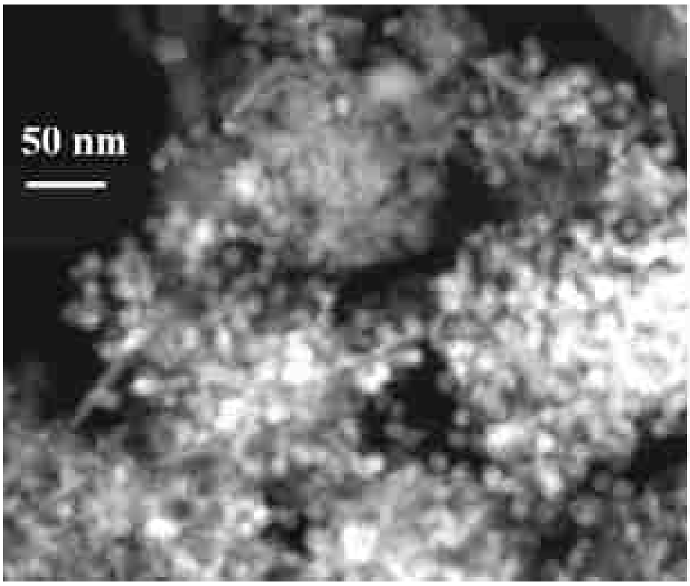

Figure 4.6. STEM image of the as-prepared FeNi nanoparticle catalyst

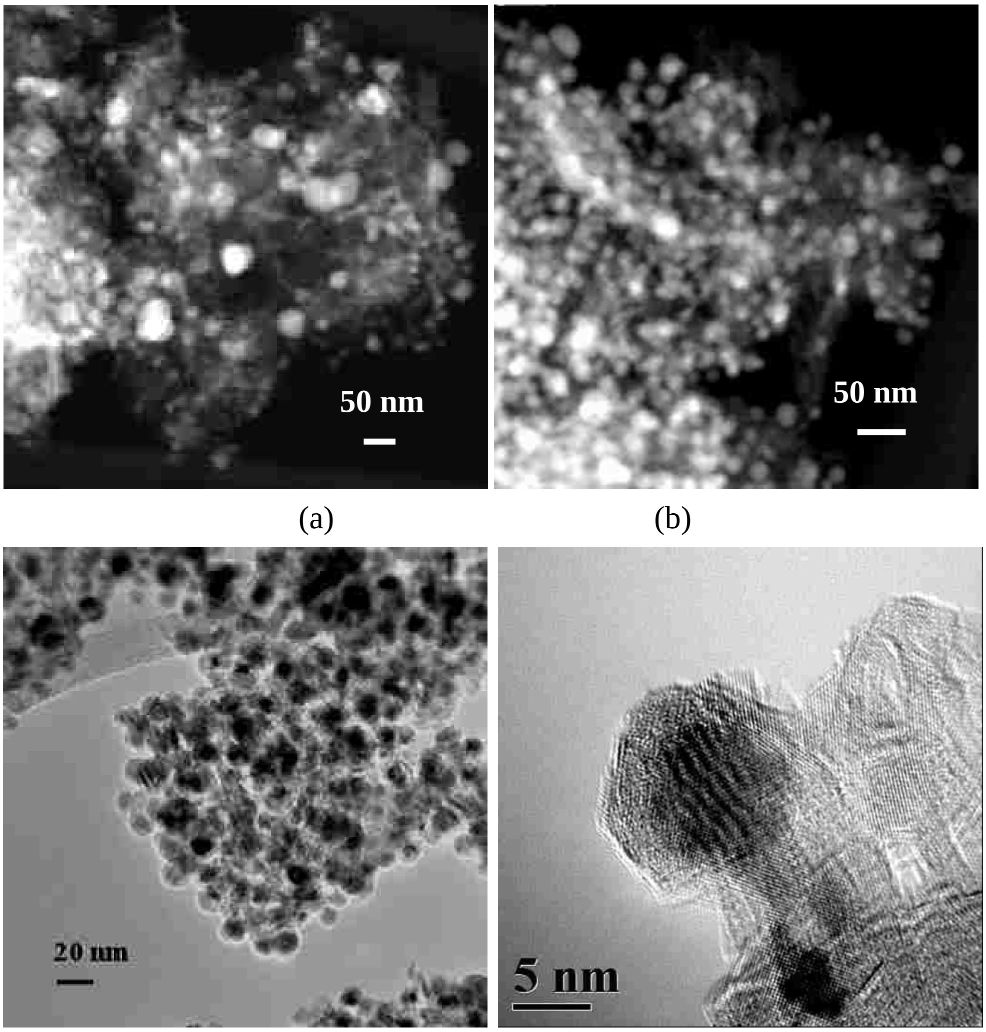

(a) (b)

(c) (d)

Figure 4.7. Microscopic images of (a) STEM image of FeNi IW/Mg(Al)O reduced at 700 C for 2 h; (b) STEM image of FeNi np/Mg(Al)O reduced at 600 C for 1 h; (c) TEM image of reduced FeNi np/Mg(Al)O; (d) HRTEM image of FeNi np/Mg(Al)O.

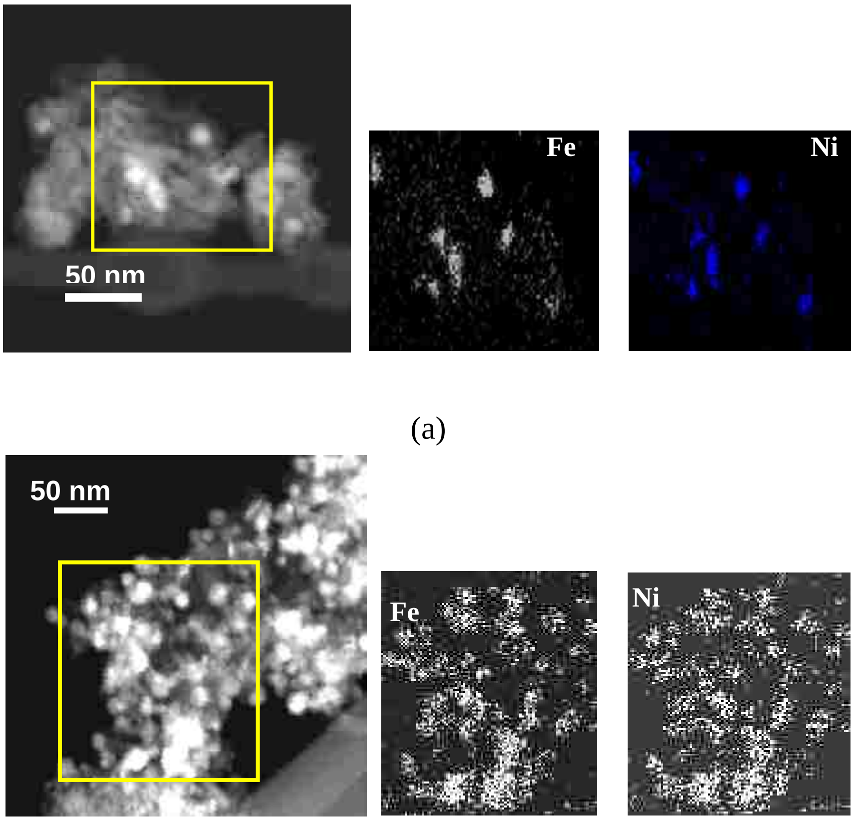

(a)

(b)

Figure 4.8. EDS Element map of: (a) FeNi IW/Mg(Al)O and (b) FeNi np/Mg(Al)O catalyst.

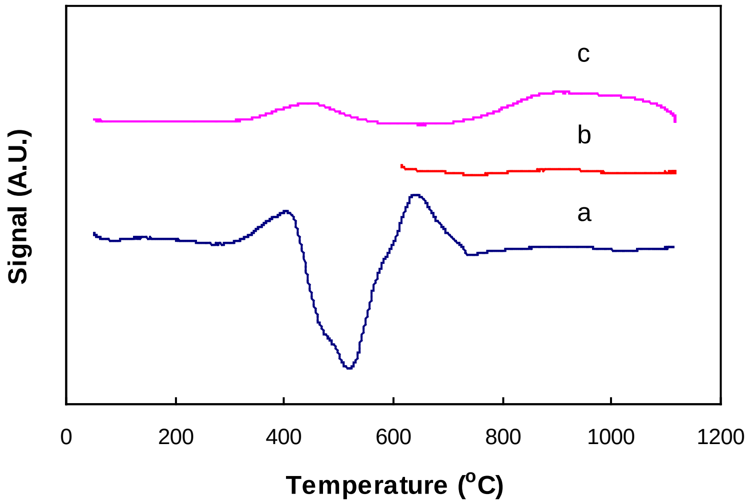

Figure 4.9. Temperature programmed reduction over: (a) FeNi np/MgAlO as-prepared (b) Pre-reduced FeNi np/MgAlO ; (c) FeNi IW/MgAlO as-prepared.

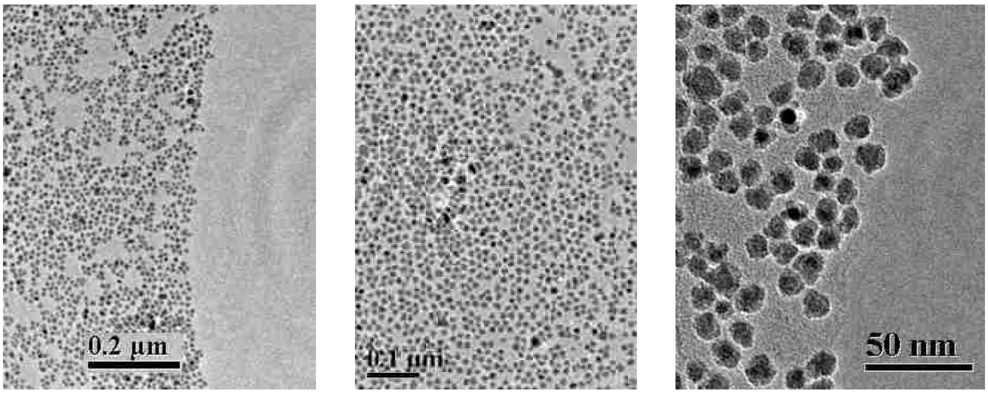

(a) **(b)** **(c)**

Figure 4.10. TEM images of FeNi nanoparticles on carbon coated Cu grid, sample treated in H_2 flow at 600°C for 1 h.

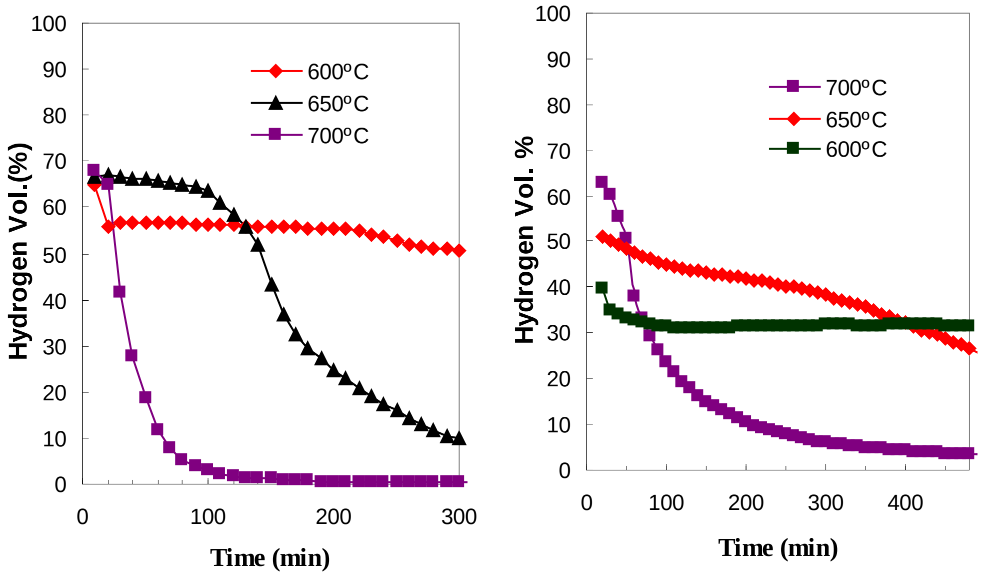

Figure 4.11. Time-on-stream (TOS) H_2 production over: (a) FeNi np/Mg(Al)O (0.2 g loading); (b) FeNi IW /Mg(Al)O (1.0 g loading). The balance of the product stream is unreacted methane.

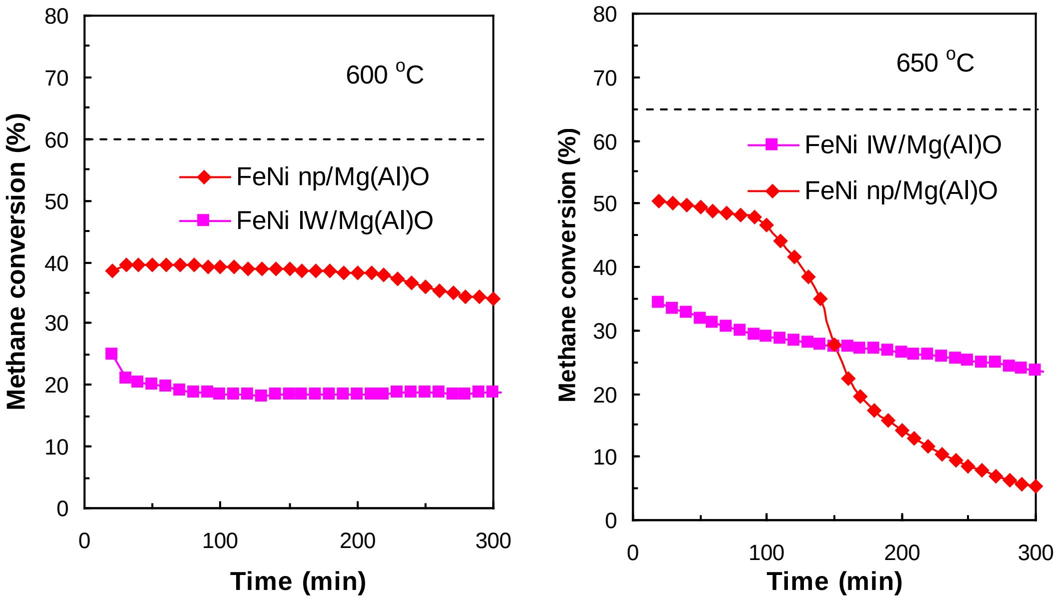

Figure 4.12. TOS methane conversion over FeNi np/Mg(Al)O (0.2 g loading) and FeNi IW/Mg(Al)O (1.0 g loading) catalysts at 600ºC and 650ºC. The dashed line shows the equilibrium conversion.

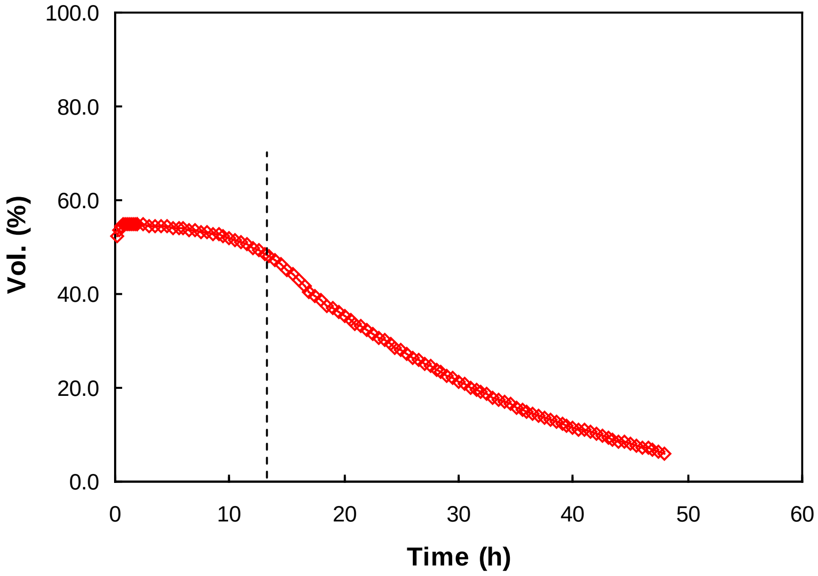

Figure 4.13. TOS hydrogen production from methane dehydrogenation at 600ºC using an FeNi np/Mg(Al)O catalyst with catalyst loading of 0.5 g.

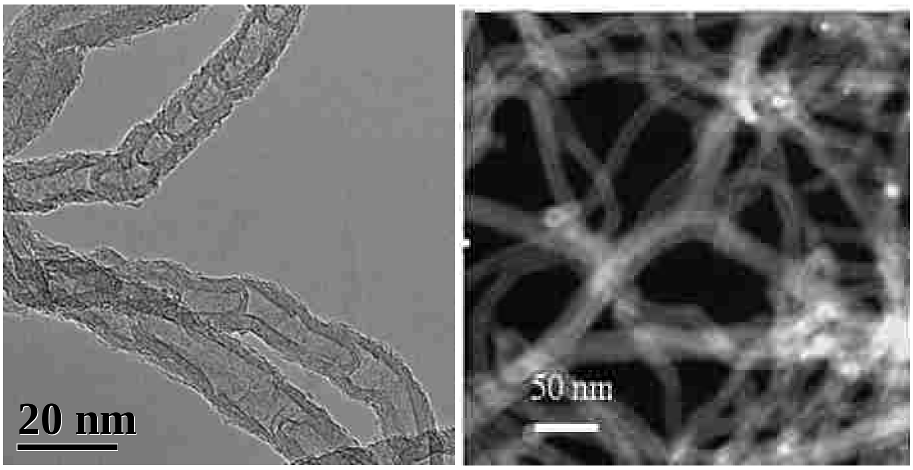

(a) (b)

Figure 4.14. The morphologies of CNTs produced over FeNi np/Mg(Al)O at 600ºC: (a) HRTEM image; (b) STEM image

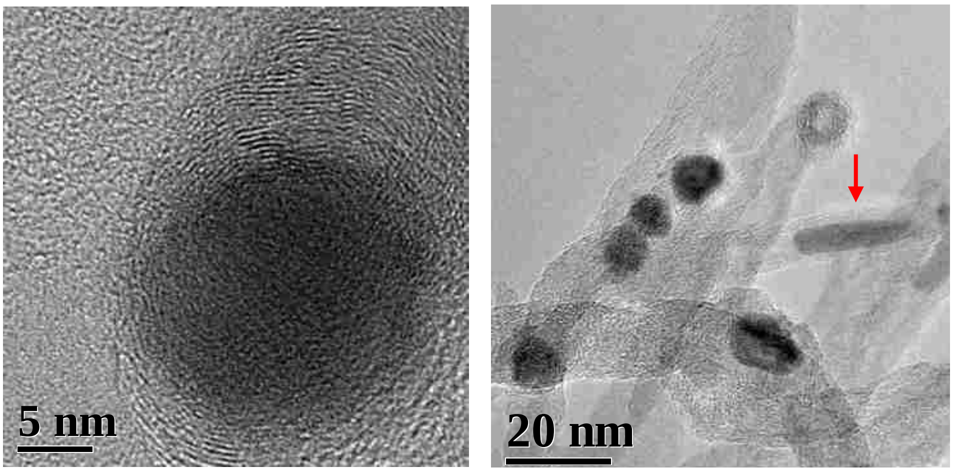

(a) (b)

Figure 4.15. The morphologies of FeNi nps after 5 h reaction at: (a) 600ºC and (b) 700ºC.

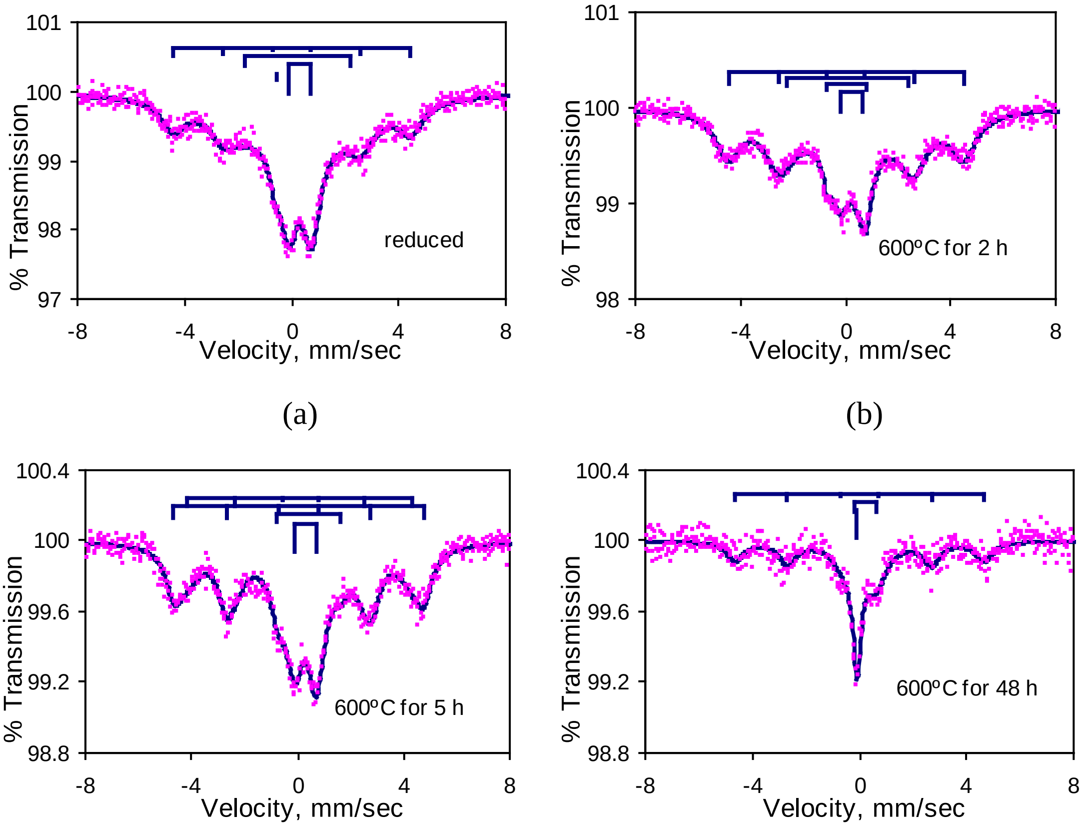

(a) (b)

(c) (d)

Figure 4.16. Mössbauer spectra of FeNi np/Mg(Al)O catalyst at different conditions: (a) reduced /passivated; (b) (c) (d) after reaction at 600ºC for 2 h, 5 h and 48 h

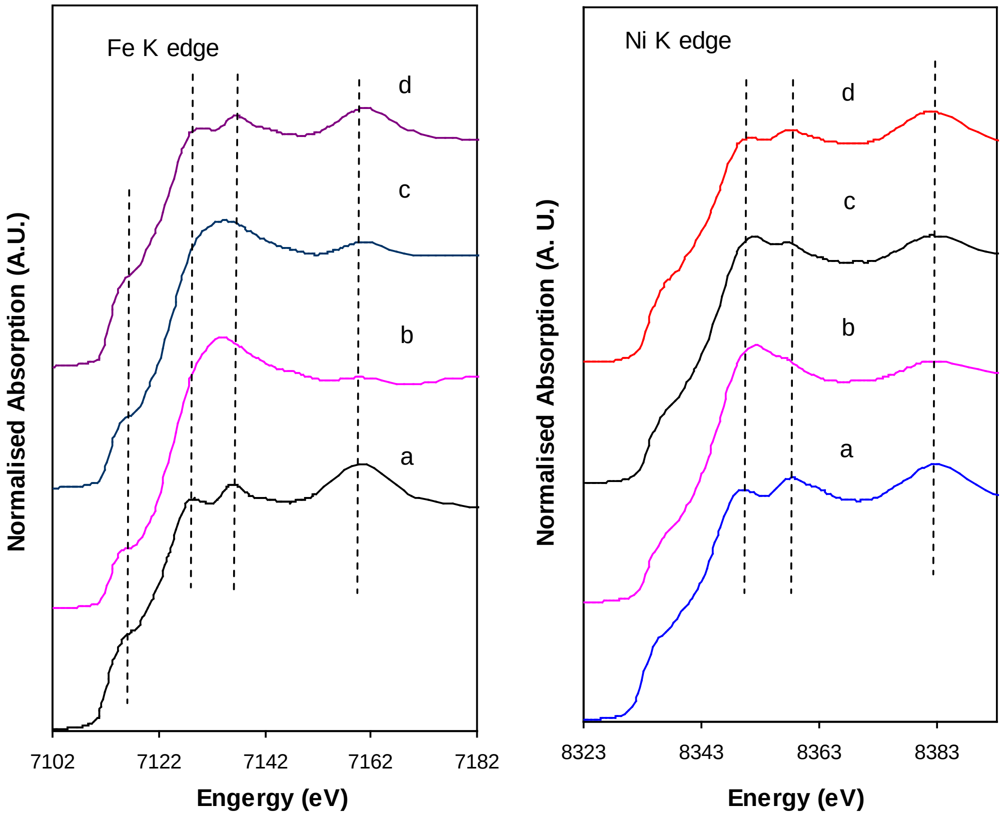

Figure 4.17. Fe K edge (Left) and Ni K edge (Right) XANES spectra of FeNi np/Mg(Al)O catalyst at different conditions: (a) Fe foil or Ni foil as reference; (b) reduced/passivated catalyst; (c) after reaction at 600ºC for 5 h; (d) deactivated catalysts after reaction at 600ºC for 48 h.

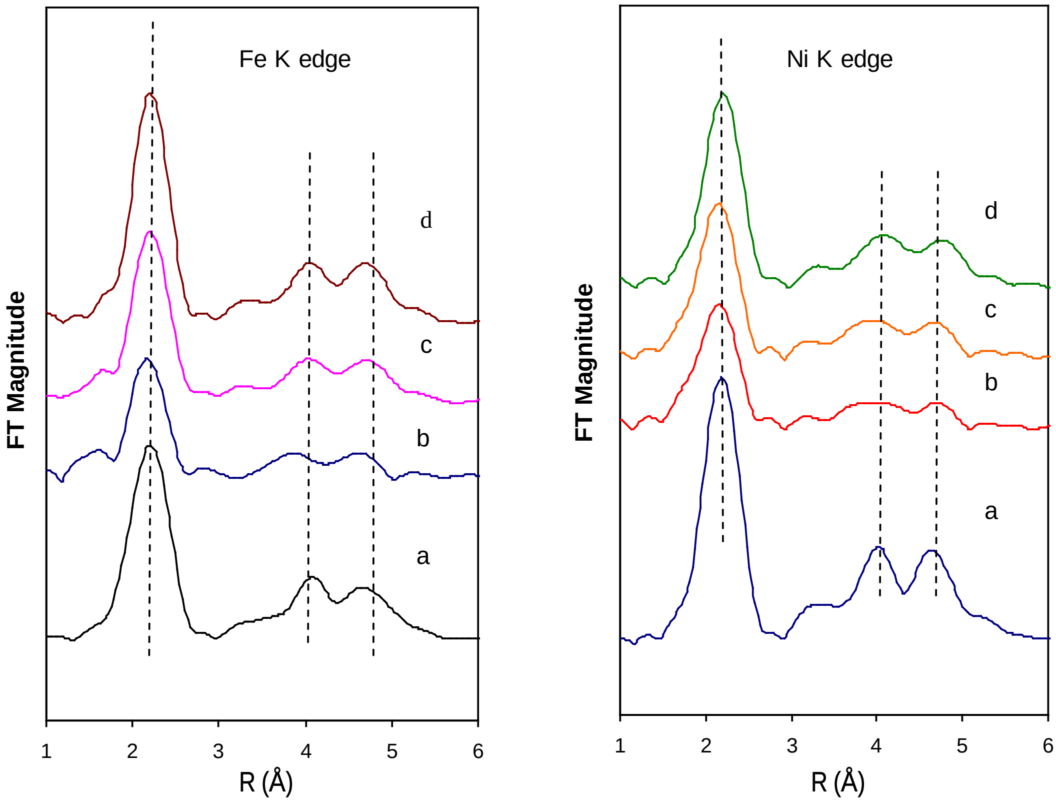

Figure 4.18. Fourier transform EXAFS spectra of Fe K edge (Left) and Ni K edge (Right) of FeNi np/Mg(Al)O catalysts at different conditions: : (a) Fe foil or Ni foil as reference; (b) reduced/passivated catalyst; (c) after reaction at 600ºC for 5 h; (d) deactivated catalysts after reaction at 600ºC for 48 h.

FeNi np/Mg(Al)O Fe K edge

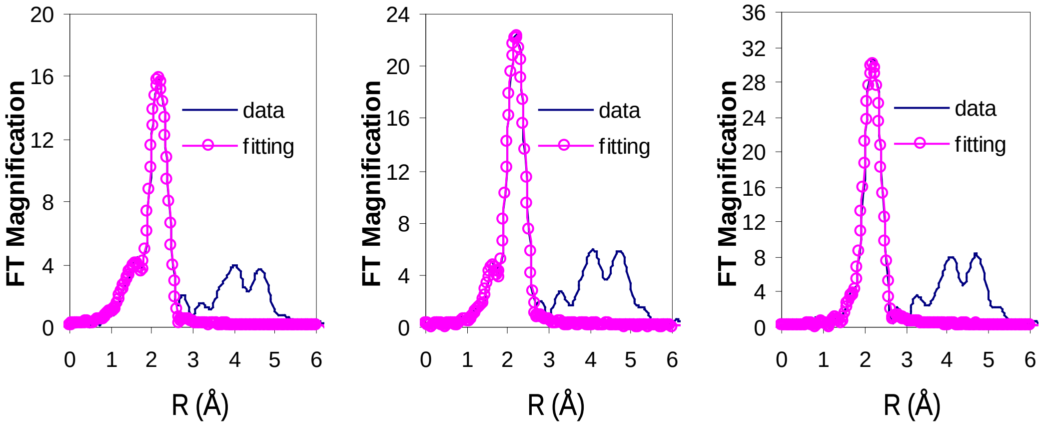

(a) (b) (c)

FeNi np/Mg(Al)O Ni K edge

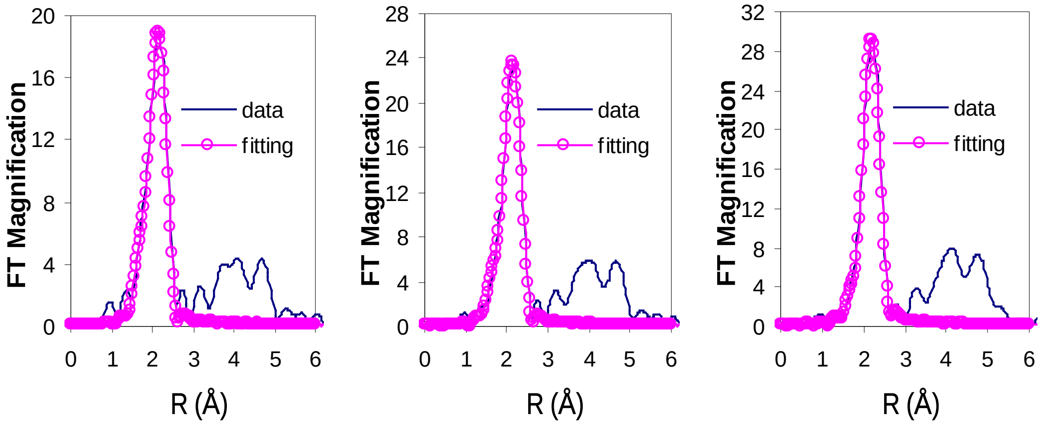

(a) (b) (c)

Figure 4.19. Radial structure function and the first shell fitting of the FeNi np/Mg(Al)O catalyst in the reduced/passivated state (a), and used at 600ºC for 5 h (b) and 48 h (c). Top: Fe K edge and bottom: Ni K edge. The fitting Parameters are listed in Table 3.2.

Chapter 5. Non-oxidative Methane Dehydrogenation over Novel Supported Fe/Mg(Al)O Nanoparticle Catalysts: Particle Size Effect

5.1 Introduction

The interest in nanoscale materials derives from the unusual properties they exhibit because of their small size, resulting in many novel applications in optical, electronic, magnetic materials, and nano-biotechnology. In heterogeneous catalysis, the decrease in the catalyst particle size to the nanometer scale normally increases the ratio of surface area to volume, thereby increasing the number of available catalytically active sites on the surface and improving catalyst performance. Moreover, in addition to the reduction in particle size, the electronic band structure may be significantly altered, as well as the interaction with the support, which may also lead to different catalytic activity [142]. The dependence of catalytic activity on particle size been reported for gold catalysts, which are inert in bulk form, but, once the size is reduced to between 3 and 5 nm, show good activity for CO oxidation. However, when the particle size is reduced to less than 2 nm, the gold nanoparticles lose their ability to absorb CO at their surfaces [143, 144]. Similarly, monodisperse Pt nanoparticles with a narrow size distribution were prepared and loaded onto Vulcan XC-72 carbon support by nanoparticle impregnation method for use as fuel cell electrocatalysts [145]. Results for this catalyst system indicated that 3.5 nm and 4 nm Pt particles had a much higher intrinsic activity for methanol oxidation but a lower tolerance for CO poison compared with 6.0 nm, 9.5 nm, and 11.5 nm size particles. Furthermore, Pt particles larger than 10 nm and smaller than 3 nm lost their efficiency for methanol oxidation [146]. Catalyst particle size effects on the performance of Fischer-Tropsch synthesis were also investigated by using Co catalysts in the range of 2.6 to 27 nm supported on carbon nanofibers (CNF) prepared by precipitation, incipient wetness and ion-adsorption methods with different metal loading. The result showed that the optimum particle size was between 6 and 8 nm [147]. Ermakova et al. [148] used a Ni/SiO_2 catalyst with 90 wt.% Ni loading for methane decomposition to grow filamentous carbon. However, a catalyst with an initial particle size of 30 to 60 nm had the longest life time. Yu et al. [149] prepared Fe catalysts on silica by different approaches to obtain varying Fe particle size distributions for carbon nanotubes (CNTs) growth from CO disproportionation. A particle size in the range of 13 to 15 nm resulted in the maximum CNTs growth rate. Baker et al. [150] reported the preparation of carbon nanofibers and nanotubes from a C_2H_4-CO-He gas mixture at 600ºC using an Fe catalyst supported on carbon. The results showed that CNFs were obtained from Fe particles larger than 20 nm, while the CNTs were formed from the smaller Fe particles less than 20 nm. Takenaka et al. [21] found that Fe_2O_3 crystallites on alumina smaller than 30 nm in fresh catalysts were transformed to α-Fe and cementite while those with larger size particles were transformed into austenite after exposure to methane at 800ºC for filamentous carbon production.

As the size of nanoparticle catalysts may play an important role in their catalytic behavior, it is meaningful to design catalysts with the optimum size to achieve the best performance. Precise control of catalyst particle size is the art of nanotechnology. With the development of organometallic based strategies for nanoparticle synthesis, monodisperse transition-metal nanoparticles with narrow size distribution can be easily prepared, thus opening new avenues to develop catalysts with tunable size and providing insights into catalysis at the nanometer scale. Recently, our research group developed catalysts for non-oxidative dehydrogenation of hydrocarbons to produce CO_x-free hydrogen and easily purified carbon nanotubes (CNTs) as potential valuable by product [65, 96]. A novel FeNi nanoparticle catalyst was prepared by a nanoparticle impregnation method. Monodisperse FeNi nanoparticles with a 9 nm mean particle size were homogeneously distributed onto a basic Mg(Al)O support by ultrasonication in hexane. The as-prepared FeNi nanoparticle catalyst could be easily reduced at 600°C in hydrogen and showed a much higher activity and longer life-time for methane dehydrogenation at 600-650°C than a similar catalyst prepared by incipient wetness. There was little or no sintering or agglomeration of the FeNi nanoparticle after reduction or during methane dehydrogenation [151]. Based on this research, monodisperse iron oxide nanoparticles with average particle sizes of 5, 10, 15 nm were synthesized and loaded onto the Mg(Al)O support. The catalytic performance for methane non-oxidative dehydrogenation was evaluated with these Fe nanoparticle catalysts, along with a related Fe/Mg(Al)O catalyst prepared by incipient wetness method, to discern the optimum particle size for methane non-oxidative dehydrogenation. Fe catalysts on various catalyst supports have been extensively studied for CNTs production. However, the optimum particle size and the role that Fe played were quite contradictory from each research due to the variability of the catalysts prepared by different methods. Furthermore, there was little or no emphasis on optimization of H_2 production in these previous studies with Fe-based catalysts. Hence, this study designed to gain insight into the role of catalyst particle size in non-oxidative methane dehydrogenation to produce both CO_x-free hydrogen and CNTs.

5.2 Experimental

5.2.1 Preparation of Monodisperse Iron Oxide Nanoparticles by Seeded Growth

Monodisperse iron-oxide nanoparticles with different mean particle sizes of 5, 10, 15 nm were prepared by thermal decomposition of iron (III) acetylacetonate ($Fe(acac)_3$) in the presence of 1,2 hexadecanediol, oleic acid and oleylamine, followed by a seeded growth [123].

To synthesize the 5 nm iron oxide nanoparticles, 4 mmol (1.42 g) $Fe(acac)_3$, 20 mmol (5.74 g) 1,2-hexadecanediol, 12 mmol (3.76 g) oleic acid, 12 mmol (4.58 g) oleylamine, and 40 mL phenyl ether were mixed and magnetically stirred under a flow of Ar. The mixture was heated to 200ºC for 30 minutes and then heated to the reflux temperature of 267 ºC for another 30 minutes. The resulting mixture was cooled to room temperature. 80 mL ethanol was added to precipitate the nanoparticles, which were then separated by centrifuge. The resulting precipitate was redispersed in 40 mL hexane in the presence of 0.1 mL oleic acid and 0.1 mL oleylamine. The mixture was ultrasonicated for 10 minutes, then, centrifuged to discard any residue that could not disperse in hexane. The nanoparticles in hexane could be separated by adding 40 mL ethanol and centrifugation. Excess ethanol was added to wash the nanoparticles three times. Then, the product was dispersed in hexane for future use.

To synthesize the 10 nm iron oxide nanoparticles, the reaction was started with 4 mmol Fe(acac)$_3$ (1.42 g), 20 mmol 1,2-hexadecanediol (5.74 g), 4 mmol oleic acid (1.26 g), 4 mmol oleylamine (1.52 g) and 40 mL phenyl ether, slowly heated to 200 ºC and kept at that temperature for 2 h and then heated to the reflux temperature of 267 ºC for 1h under the protection of Ar. The resulting nanoparticles were separated, cleaned according to the procedure above, and dispersed in 10 mL hexane. Using these nanoparticles in hexane as seeds, additional 4 mmol Fe(acac)$_3$ (1.42 g), 20 mmol 1,2-hexadecanediol (5.74 g), 4 mmol oleic acid (1.26 g), 4 mmol oleylamine (1.52 g) and 40 mL phenyl ether were added to form a mixture. The mixture was heated to 100 ºC to evaporate all hexane, then heated to 200 ºC and held for 1 h, before being heated to reflux for 1 h. After cooling down to room temperature, separated and purified, 8 mmol of nanoparticles were obtained with relatively larger size. 2 mmol of the above generated nanoparticles were used as seeds to grow 4 mmol of bigger particles. By repeating the procedure once more, 8 mmol of nanoparticles with an average particle size of 10 nm were synthesized.

To synthesize the 15 nm iron oxide nanoparticles, the same seeded growth mechanism was used, but a higher boiling point and a longer chain solvent, octyl ether (303ºC) was used instead of phenyl ether. In a typical synthesis, 2 mmol Fe(acac)$_3$ (0.71 g), 10 mmol 1,2 hexadecanediol, 6 mmol oleic acid, 6 mmol oleylamine and 20 mL octyl ether were mixed, heated to 200 ºC for 2 h, next, heated to reflux temperature (303 ºC) for 1 h. The resulting nanoparticles in hexane were used as seeds, together with another 2 mmol Fe(acac)$_3$, 10 mmol 1,2-hexadecanediol, 2 mmol oleic acid, 2 mmol oleyamine, and 20 mL octyl ether to grow yet bigger nanoparticles. The produced nanoparticles were separated and purified by regular procedures and dispersed in 10 mL hexane. 2 mL ethanol was added to size-sort the nanoparticles. The superanant with small particles was discarded, and the precipitate was redispersed in hexane as synthetic Fe-15 nm nanoparticles.

5.2.2 Preparation of Catalysts

Details of the preparation of the Mg(Al)O support (Mg/Al=5) have been described in chapter 3. The Fe nanoparticle catalysts were prepared by a nanoparticle impregnation method. The details were reported in chapter 4 and elsewhere [151], and involved the incorporation of Fe nanoparticles dispersed in hexane onto the Mg(Al)O support under ultrasonication. The resulting catalysts were first dried slowly at room temperature and then further dried in an oven at 100ºC overnight. This is the so-called as-prepared Fe nanoparticle catalyst. The procedure to prepare a similar Fe catalyst on a Mg(Al)O supported by incipient wetness method was also described previously [96]. Briefly, $Fe(NO)_3 \cdot 9H_2O$ was dissolved in de-ionized water based on the total Fe loading of 5 wt.% and dropped into the Mg(Al)O powder. The mixture was then thouroughly mixed, dried at 100ºC, calcined at 500ºC for 5 h to yield the as-prepared Fe IW/Mg(Al)O catalyst.

5.2.3 Methane Dehydrogenation Reaction

Dehydrogenation of methane was conducted in a fixed-bed plug-flow reactor. The reactor chamber was a quartz tube with an inner diameter of 22.5 mm. In a typical reaction, 0.2 gram of catalyst was loaded at the center of the reactor to form a thin layer of catalyst bed supported by quartz wool. Before contact with catalyst, the inlet gas was distributed by a quartz wool plug and preheated. The Fe nanoparticle catalysts were activated in a flow of H_2 at 50 mL/min at 600ºC for 2 h with a ramping rate of 10 K/min, whereas the Fe IW catalyst was activated in the H_2 atmosphere at a higher temperature of 700ºC for 4 h due to the much stronger metal support interaction. After reduction, the reactor was cooled to 350ºC, the H_2 flow was shut down, and 10 mL/min methane was introduced to the reactor to flush all residual H_2 from the reactor. Next, the reaction zone in the quartz tube was heated to the reaction temperature within 3 minutes. The methane dehydrogenation reaction was conducted at 600, 650 and 700ºC. The inlet gas flow was controlled by a mass flow controller and the effluent was monitored by a bubble flow meter and analyzed by an online gas chromatograph (GC) with a built-in thermal conductivity detector (TCD). The gas products were quantified as a volume percentage of the total gas effluent. The solid carbon product was collected after reaction. Methane conversion was calculated based on the H_2 volume percentage in the effluent as shown in chapter 4.

5.2.4 Characterization

The size distributions of the as-prepared Fe nanoparticles were determined by transmission electron microscopy (TEM) using a JEOL 2010F instrument operating at 200 kV. The size distributions were based on analysis of 400 to 500 individual nanoparticles. To prepare the Fe nanoparticle samples for the TEM, a drop of very dilute hexane-dispersed nanoparticle sample was deposited onto a carbon coated Cu grid and the hexane was slowly evaporated at room temperature under a glass cover. The distributions of the Fe nanoparticles in the as-prepared catalysts were studied by scanning transmission electron microscopy (STEM). The samples were prepared by slightly crushing the catalysts, dispersing them in acetone by ultrasonication, then loading a drop of the suspension onto a lacey carbon coated Cu grid, and drying at room temperature. The used catalysts with CNTs were also characterized by TEM. The samples were prepared by the same procedure as the as-prepared Fe catalyst samples. The iron content of each catalyst was analyzed by Inductively Coupled Argon Plasma Spectrometry (ICP) by Kentucky Geological Survey Laboratory Services. To prepare samples for the ICP test, the catalysts were dissolved in 50 mL 6M HNO_3. X-ray diffraction was conducted on the synthesized nanoparticles using a Siemens 5000 diffractometer, Ni-filtered Cu Kα radiation, and a scanning rate of 0.05^{o} 2θ/min . Mössbauer spectroscopy was carried out at room temperature to characterize the Fe nanoparticle catalysts in their as-prepared and after-reaction states using Halder GmbH drive and control system with a ^{57}Co (Rh) source of 14.4 keV γ--rays. The spectra were analyzed by least-squares fitting using a computer routine that fits individual Fe components as single peaks, quadrupole doublets, or magnetic sextets based on Lorentzian line profile. All isomer shifts are given relative to metallic α-Fe at room temperature (293 K).

5.3 Results and Discussion

5.3.1 Characterization of Synthetic Nanoparticles and Nanoparticle catalysts

Figure 5.1 shows the TEM micrographs of synthesized iron oxide nanoparticles with average particle sizes of 5, 10, and 15 nm and the corresponding particle size distributions. The nanoparticles are monodispersed in all three cases due to the protection of surfactants (oleic acid and oleylamine). As shown in figure 5.1 (a) and (b), thermal decomposition of $Fe(acac)_3$ in the presence of surfactant in phenyl ether, followed by seeded growth, can be successfully used to prepare monodisperse iron oxide nanoparticles with a relatively narrow size distribution. However, by using a long chain solvent with a higher boiling point such as octyl ether, the synthesized nanoparticle seeds showed a less regular shape with average particle size about 10 nm. After the seeded growth, the particles had a broad size distribution within two regions: very small particles < 2-3 nm and larger particles > 10 nm. The smaller particles could be easily separated by a size-sorting procedure, in which ethanol was dropped into the hexane dispersed nanoparticle suspension to precipitate the larger particles. After this size-sorting, the particle size distribution (PSD) of the synthetic 15 nm nanoparticles is shown in figure 5.1 (c); it ranges from 10 nm, has a very sharp maximum at about 15 nm and extends to a few nanoparticles larger than 20 nm. Even though there exists minor size overlap in certain regions of synthetic nanoparticles, the mean sizes of the particles are very different for the three materials. These synthetic nanoparticles were then loaded onto the Mg(Al)O support to complete the preparation of Fe nanoparticle catalysts for methane dehydrogenation.

The iron loading in the catalysts as determined by ICP analysis is listed in table 5.1. The Fe-5 nm/Mg(Al)O and Fe-10 nm/Mg(Al)O catalysts have the same Fe loading of about 3.2 wt.%, while the Fe-15 nm/Mg(Al)O catalyst contains 4.2 wt.% Fe and the Fe IW/Mg(Al)O catalyst has the highest loading of 5 wt.%.

Figure 5.2 shows the X-ray diffraction patterns of synthesized iron-oxide nanoparticles with average particle sizes of 10 and 15 nm, respectively. The synthetic nanoparticles are single phase with a cubic structure. Maghemite and magnetite have very similar XRD patterns and therefore it is difficult to distinguish them by XRD. However, the synthesized nanoparticles appear to be maghemite (γ - Fe_2O_3) because of the yellowish-brown color observed in diluted hexane solution instead of the black color of magnetite (Fe_3O_4). Sun et al. [123] reported the formation of magnetite nanoparticles by high temperature solution phase reaction of $Fe(acac)_3$ with 1,2 hexadcanediol in the presence of oleic acid and oleylamine. These magnetite nanoparticles were then further oxidized to maghemite under O_2 at 250ºC for 2 h. The maghemite nanoparticles were obtained here without needing the extra oxidation procedure.

Mössbauer spectroscopy provides a clearer indication that maghemite instead of magnetite has been formed. Room temperature Mössbauer spectra of the as-prepared Fe catalysts are shown in Figure 5.3 and the derived fitting parameters are given in table 5.2. The spectrum of the as-prepared Fe IW/Mg(Al)O is best represented by three ferric iron doublets with approximately the same isomer shift (IS), 0.32 ± 0.02 mm/s, and individual quadrupole splittings (QS) of 0.53, 0.93 and 1.45 mm/s. This composite absorption arises from ferric ions in a non-magnetic oxide phase. There is no asymmetry in the spectrum to suggest that any Fe^{2+} might be present. The first two doublets are the major component (about 92% Fe), attributed to Fe^{3+} dispersed in Mg(Al)O solid solution formed by calcination of a Mg-Al-(Fe) hydrotalcite like compound (HTLs) [83]. The doublet with higher QS of 1.45 mm/s indicates a highly asymmetric environment and is attributed to cluster-type Fe^{3+} oxide formed on the surface of Mg(Al)O support [83, 84].

The room-temperature Mössbauer spectra of the nanoparticle iron catalysts are much more complex and appear to derive from both non-magnetic and superparamagnetic ferric oxides. A relatively sharp doublet, with an IS of 0.32 mm/s and a QS of 0.65 mm/s, was fitted for the Fe-5 nm/Mg(Al)O catalyst that closely corresponds to the overall non-magnetic absorption observed for the Fe IW catalyst. However, it only contributes about 16% of the total absorption; the remainder of the absorption is attributed to superparamagnetic iron oxides. For the Fe-10 nm/Mg(Al)O and Fe-15 nm/Mg(Al)O catalysts, the non-magnetic component is more or less absent and the spectra derive entirely from superparamagnetic effects in the iron oxides. For the Fe-15 nm/Mg(Al)O catalyst, the superparamagnetism is beginning to give way to magnetic ordering as evidenced by the broad magnetic peaks occurring at about -8 and +8 mm/s in the spectrum. Like the IW catalyst, there is no significant absorption that can be attributed to the presence of Fe^{2+} in any of these nanoparticle catalysts. This lack of any Fe^{2+} is consistent with the iron oxide being maghemite.

A more detailed examination of the magnetism of these materials is currently in progress using both Mössbauer spectroscopy and SQUID magnetometry as a function of temperature. Preliminary results from low-temperature Mössbauer spectroscopy for the Fe-5 nm/Mg(Al)O catalyst indicate a relatively sharp magnetic transition over the temperature range 15 - 50 K, and a second much more diffuse superparamagnetic transition that extends over a much wider temperature range up to room temperature. We attribute the sharp transition at low-temperature to magnetic ordering effects between adjacent particles, whereas the broad transition is tentatively attributed to more distant interparticle array effects. The temperature of the magnetic transition at about ~30 K is consistent with the 5 nm average particle size.

Figure 5.4 shows the Mössbauer spectrum of the Fe-5 nm/Mg(Al)O catalyst collected at 16.5 K and the derived parameters are listed in table 5.2. The spectrum has been fit using two broad sextets with similar IS values of 0.40 and 0.45 mm/s and magnetic hyperfine splittings, H_0, of 489 and 440 kG and a single peak with an IS of 0.21 mm/s corresponding to SPM Fe^{3+}. Whereas magnetite has an inverse spinel structure with formula $(Fe^{3+})_A[Fe^{2+}Fe^{3+}]_BO^{2-}_4$, in which the tetrahedral A sites are occupied by Fe^{3+} and the octahedral B sites are occupied 50:50 by both Fe^{2+} and Fe^{3+}, maghemite has a defect inverse spinel structure and the formula can be written as $(Fe^{3+})_A[Fe^{3+}_{5/3}V_{1/3}]_BO^{2-}_4$, where V refers to the cation vacancy. For maghemite, both site A and B are occupied entirely by Fe^{3+}, which is consistent with the oxidation state of iron indicated by Mössbauer spectroscopy. The low temperature Mössbauer spectrum shown here confirms that the synthetic Fe nanoparticles consist only of maghemite.

Figure 5.5 presents the STEM images of the as-prepared nanoparticle catalysts. It can be seen that the synthesized iron oxide nanoparticles are evenly dispersed on the Mg(Al)O support by the nanoparticle impregnation method. The details about the synthesis of Mg(Al)O support and its properties have been described elsewhere [96]. Each nanoparticle lies on the surface of Mg(Al)O support, without significant agglomeration. There were no obvious differences in all three Fe nanoparticle catalysts except for the different particle size. In the as-prepared IW catalyst, no iron particles could be observed before high temperature reduction in H_2, consistent with the conclusion from the Mössbauer spectroscopic characterization that most of the iron has been dispersed due to reaction with Mg(Al)O support during calcinations at 500 ºC.

The Mössbauer and TEM results show that the as-prepared supported Fe np catalysts are significantly different to the Fe IW catalyst. Whereas the Fe IW catalyst appears to have reacted extensively with the support, presumably forming $Mg(Al,Fe^{3+})_2O_4$, the Fe np catalysts have resisted significant reaction with the support and remained predominantly as superparamagnetic maghemite. This difference is likely due in large part to the lack of calcination of the Fe np particles after being deposited on the support.

5.3.2 Methane Dehydrogenation

Figure 5.6 shows the time-on-stream (TOS) H_2 production distribution for methane dehydrogenation using undiluted CH_4 over the Fe-5 nm/Mg(Al)O, Fe-10 nm/ Mg(Al)O, Fe-15 nm/Mg(Al)O and Fe IW/Mg(Al)O catalysts at 600, 650 and 700ºC. The methane flow rate was kept at 10 mL/min and the catalyst was tested with a space velocity of 3000 $mL \cdot h^{-1} \cdot g^{-1}$ catalyst. At 600ºC, the Fe-5 nm/Mg(Al)O and Fe-10 nm/Mg(Al)O catalysts were able to maintain a relatively higher methane conversion with only a slight deactivation during the reaction. The H_2 volume percentage in the effluent increased to its highest level of 40 vol. % over the Fe-10 nm/Mg(Al)O catalyst within 15 minutes, and then decreased slightly to 35 vol.% after 5 h. The Fe-5 nm/Mg(Al)O catalyst showed a parallel trend. H_2 in the outlet slightly increased at the beginning of reaction to a maximum of 32 vol. %, then decreased slowly to 27 vol.% after 5 h. The deactivation rate of both catalysts was about 1 vol.% H_2/h. The Fe-15 nm/Mg(Al)O catalyst had a much faster deactivation rate. Initially, the H_2 content increased from 15 vol. % to 30 vol. % within 15 minutes then deactivated quickly to less than 1 vol. % in 4 h and was completely deactivated after 5 h. In contrast to the Fe nanoparticle catalysts, the Fe IW/Mg(Al)O catalyst showed a very short induction period at the beginning of the reaction. The catalyst then deactivated very fast over the first hour of reaction, as the vol.% H_2 reduced from 33 to 20 vol.% H_2 in the product gas, at which point the deactivation rate reduced to about the same rate as the Fe-5 nm and Fe-10 nm catalysts. The activity of methane dehydrogenation over the Fe IW catalyst is lower than that over the Fe-5 nm and Fe-10 nm catalysts. In all experiments, the Fe-10 nm/Mg(Al)O catalyst showed the highest activity.

Upon increasing the reaction temperature to 650ºC, differences between the Fe-10 nm catalyst and Fe-5 nm catalysts become apparent. Again, the Fe-10 nm catalyst showed the highest methane dehydrogenation activity of the four catalysts. The H_2 content in the outlet reached its highest value, about 59 vol. %, after about 10 minutes of reaction, and then decreased in two stages. For the first 4 h, the catalyst deactivated at an average rate of 4 vol. % H_2/h, from 59 vol. % to 43 vol. % H_2. After this point, the catalysts deactivated much faster and the H_2 content in the product gas dropped from 43 vol. % to 32 vol. % within 1 h. The Fe-5 nm catalyst also showed similar two-stage deactivation behavior. However, it deactivated much faster than the Fe-10 nm catalyst during both stages. After the first one and a half h, the H_2 content decreased from its highest value of 53 vol. % to 39 vol. %, at an average deactivation rate of 9.3 vol. %/h, compared with 4 vol. %/h with the Fe-10 nm catalyst. Then, the catalyst deactivated even more quickly and the H_2 content was reduced to only 2 vol. % after 5 h reaction. Both the Fe-15 nm catalyst and the Fe IW catalyst deactivated quickly immediately after the short induction period and completely lost their catalytic activity after about 3 and 5 h, respectively. The Fe IW catalyst had a relatively higher methane conversion initially, about 45 vol. % of H_2 in the outlet gas, compared with the Fe-15 nm catalyst with 34 vol. % of H_2 produced.

Upon further increasing the temperature to 700ºC, all the catalysts deactivated rapidly during reaction. However, the Fe-10 nm did show the highest initial methane conversion of 71 vol.% of the product as H_2 and the longest life-time. The performance of the Fe IW catalyst was in between that of the Fe-5 nm and Fe-15 nm catalysts. All the Fe-based catalysts exhibited a very short life-time at 700ºC, indicating that the synthesized catalysts on Mg(Al)O should only be used at temperatures well below 700ºC.

Figure 5.7 shows the relationship of the initial highest methane conversion over the synthesized nanoparticle catalyst versus the reaction temperature. The result for a FeNi-9 nm/Mg(Al)O catalyst is also included for comparison. Details about the methane dehydrogenation performances of this FeNi-9 nm/Mg(Al)O catalyst were reported in a previous study [151]. Methane conversion increased almost linearly with the increase of reaction temperature for all three Fe nanoparticle catalysts. However, the increases in rate for the Fe-5 nm and Fe-10 nm catalysts were much higher than for the Fe-15 nm catalyst, indicating that the catalyst may exhibit different reaction mechanisms despite experiencing the same operating conditions. This inference was supported by subsequent TEM analysis (see below). Methane conversion of the Fe-10 nm catalyst was about 5 % higher than that of the Fe-5 nm catalyst at all three temperatures, indicating a higher reaction rate over the Fe-10 nm catalyst. The FeNi-9nm catalyst had a higher methane conversion at 600 and 650ºC than all other Fe-based catalysts. But upon increasing the reaction temperature to 700ºC, methane conversion did not change much. Therefore, inclusion of a second metal forming a bimetallic FeNi alloy catalyst is only effective for increasing the catalytic activity of methane dehydrogenation at temperatures below 700ºC. At higher reaction temperatures, Ni may segregate onto the surface of the FeNi catalyst particles, which completely alters the reaction mechanism of methane dehydrogenation [140, 141].

The diffusion of carbon through the catalyst particle is considered the rate-determining step for catalytic growth of CNTs and the driving force for carbon diffusion is the carbon concentration gradient arising from the difference in carbon solubility at the gas/catalyst particle surface and CNT/catalyst particle surface. The diameter of the CNT is determined by the size of the catalytic particles. Numerical calculation showed that smaller diameter CNTs had higher carbon concentrations at the CNT/catalyst particle surface [149], thus leading to a smaller driving force. On the other hand, at the same catalyst loading, smaller catalyst particles possess a larger surface area and a shorter diffusion length, thus having higher carbon diffusion rates. The compromise between these competing processes causes the catalyst particle size plays a significant role in determining the reaction rate for carbon growth. In this work, 10 nm was found to be the optimum particle size for catalytic methane dehydrogenation at 600-700ºC by Fe nanoparticles on a Mg(Al)O support (Fe np/Mg(Al)O). Fe catalysts on the Mg(Al)O support with a smaller particle size of 5 nm or a larger particle size of 15 nm lead to slower carbon diffusion rates, respectively, and less catalytic activity. It was seen by the previous STEM observation that the catalyst particles prepared by a conventional incipient wetness method and followed a high temperature reduction in H_2 usually had a wide size distribution [151]. Based on the finding of current study, Fe particles over the Fe IW/Mg(Al)O catalyst with sizes larger than 15 nm showed less activity, while particles with sizes less than 10 nm were more active. Hence, the overall activity over the Fe IW/Mg(Al)O catalyst is therefore a combination of those of both small and large particles, that is between that of the Fe-5 nm/Mg(Al)O and Fe-15 nm/Mg(Al)O catalysts.

5.3.3 TEM Characterization of Fe Nanoparticle Catalysts after Reaction

The reacted Fe nanoparticle catalysts and the carbonaceous product were collected after methane dehydrogenation. Figures 5.8, 5.9 and 5.10 present the TEM and HRTEM images of the reacted Fe-5 nm, Fe-10 nm and Fe-15 nm catalysts after 5 h reaction at 600ºC and the morphologies of the related carbon product. For the Fe-5 nm/Mg(Al)O and Fe-10 nm/Mg(Al)O catalysts, the carbon products were in the form of multi-walled CNTs (MWNTs). However, the Fe-5 nm catalyst generated much thinner walled CNTs (only 2 or 3 graphite layers) compared with the Fe-10 nm catalyst, which produced regular MWNTs with up to 10 graphite layers. The resulting CNTs were several to 100 micrometer scale in length, tangling or weaving together to form a fluffy material with BET surface areas in excess of 360 m^2/g. There was no significant agglomeration or sintering of Fe nanoparticles observed after reaction. Each Fe nanoparticle may therefore serve as an active site. However, the Fe nanoparticles were mobile during the reaction. Many individual particles were found inside the CNTs or at the tips of CNTs, duplicating the earlier observation that methane dehydrogenation over FeNi np/Mg(Al)O catalyst follows a tip growth mechanism [151]. Additionally, as shown in the HRTEM images, the deformation and elongation of Fe nanoparticles were observed in the used Fe-5 nm and Fe-10 nm catalysts, in which the nanoparticles appeared to fill the inner cavities of the CNT, behaving like a ‘liquid’ metal. This phenomenon was especially noteworthy for the Fe-10 nm catalyst. There were no carbon fibers or tubes present in the used Fe-15 nm/Mg(Al)O catalyst sample. Carbon capsules (also called onion-structured carbon product) were observed instead. Some of them were empty, while others contained individual Fe nanoparticles. The carbon yield was very low using the Fe-15 nm catalyst and there was no obvious change of the Fe particles in either size or shape after reaction.

Fe-based catalysts have been mostly studied in the production of filamentous carbon from methane decomposition at very high temperatures and it was believed that the catalytically active phases for the growth of filamentous carbon were formed by transformation of carbon saturated iron species (ɣ-Fe) into a liquid state at temperatures above 1000ºC. Usually, H_2 was used as a co-feed in this system in order to suppress the rapid deactivation of catalysts by encapsulation of carbon [21, 152]. There are only a few literature references about methane decomposition at temperatures as low as 600-800ºC over Fe-based catalyst and the results differ greatly between the studies. Tibbets et al. [152] reported that the active phase for the formation of filamentous carbon was α-Fe supersaturated with carbon at temperatures below 912ºC. Ermakova et al. [35] further demonstrated that the threshold of formation of filamentous carbon on Fe_2O_3 or Fe/SiO_2 was around 680ºC, at which temperature iron carbide is in a metastable state and could be easily transformed into the catalytic active phase, α-Fe and graphite carbon. However, Takenaka et al. [21] showed in their research that the active phases could also be γ-Fe, depending on the iron catalyst particle size (borderline is 30 nm) at 800ºC. In this study, Fe nanoparticles supported on Mg(Al)O exhibit high activity for methane decomposition at 600ºC, which is consistent with our previous report that the threshold of formation of filamentous carbon on Fe/Al_2O_3 (5 wt.% Fe) could be as low as 500ºC, reaching a maximum conversion at 700ºC in the temperature range of 400-800ºC [65]. The reason for “fluidity” of an Fe catalyst at such temperatures far below the melting point of bulk Fe is most likely due to the diffusion of carbon through Fe particle, which can lead to the transition of iron from solid metal to a quasi-liquid state. Krivoruchko et al. [128] observed the transition of α-Fe metal to the quasi-liquid state at a temperature of ~640ºC by in-situ X-ray diffraction study, but there was no report on the iron particle size. Reduction of the Fe particle size to less than 10 nm may decrease the fluidity temperature to as low as 600ºC, as observed in this study. Meanwhile, there may be an optimum particle size for the transformation from iron metal to quasi-liquid state at the same reaction conditions. It was seen in this study that the Fe-10 nm particles were more prone to transform to quasi-liquid state than the Fe-5 nm particles. However, when the particle size increased to 15 nm, the fluidity of iron particles was not observed at 600ºC. This result coincides with the order of activity for methane dehydrogenation over these nanoparticle catalysts.

5.3.4 Mössbauer Spectroscopic Characterization of Fe-10 nm/Mg(Al)O after Reaction

The Fe-10 nm/Mg(Al)O catalyst after reaction at 600, 650 and 700ºC was studied by Mӧssbauer spectroscopy. The Mӧssbauer spectra collected at room temperature are shown in figure 5.11 and the fitting parameters are listed in table 5.3. The spectrum of the Fe-10 nm catalyst used at 600ºC for 5 h shows a quadrupole doublet with IS of 0.33 mm/s and QS of 0.74 mm/s, two sextets with IS of 0.01 mm/s, H_0 of 327 kG and IS of 0.2 mm/s, H_0 of 199 kG, attributed to Fe^{3+} oxide, Fe metal and Fe carbide, respectively. The used Fe-10 nm catalyst at 650ºC for 5 h displayed a similar trend, a doublet with IS of 0.31 mm/s and QS of 0.74 mm/s, a magnetic sextet with IS of -0.01 mm/s and H_0 of 326 mm/s and another sextet with IS of 0.25 mm/s and H_0 of 198 kG, which again correspond to Fe^{3+} oxide, Fe metal and Fe carbide. The spectrum of the completely deactivated Fe-10 nm catalyst after reaction at 700ºC for 5 h was fitted similarly, but with a single peak with IS of -0.12 mm/s, attributed to austenite. The contribution of each component in the reacted catalysts is listed in table 4.3. The non-magnetic Fe^{3+} oxide may be formed by re-oxidation after exposure of the catalyst to air. The content of this absorption feature decreases from about 71% for the Fe-10 nm catalyst at 600ºC, to 58% at 650ºC, to 25% at 700ºC, while the iron carbide increases in the same order from 5.5%, to 14%, to 36.5%. Interestingly enough, the iron metal contents in all three catalysts are almost identical at around 30%. Different from the still active catalyst, the totally deactivated catalyst also contained 8.5% austenite. Austenite was also detected as an extra phase in the totally deactivated FeNi bimetallic catalysts in our previous work [96, 151].

Based on the Mössbauer results, we propose the following reaction mechanism for methane dehydrogenation over Fe nanoparticle and similar catalysts. The catalytic active phases are iron metal and a metastable solution of carbon in Fe. Once the iron particles become saturated with carbon, the concentration gradient between the gas/CNT and CNT/metal particle surfaces diminishes. Therefore, carbon no longer diffuses through the particle. Instead, carbon builds up on the surface of catalyst particle, blocking the entrance of methane to the catalyst particle surface, and thereby deactivating the catalyst. The metastable Fe-C solution transforms to Fe metal and Fe carbide upon cooling to room temperature [38]. Austenite was identified as a specific phase in the deactivated catalyst, along with iron carbide, formed from the carbon-saturated iron solution.

5.4 Conclusions

Monodisperse maghemite nanoparticles have been synthesized with average particle sizes of 5 nm, 10 nm and 15 nm by thermal decomposition of $Fe(acac)_3$ in the presence of surfactants. These nanoparticles could be easily loaded onto a Mg(Al)O support by a nanoparticle impregnation method. They were then used for methane dehydrogenation to produce H_2 and CNTs. The catalytic performance was significantly better for the Fe-5 nm/Mg(Al)O and Fe-10 nm/Mg(Al)O catalysts compared to that for an Fe catalyst prepared by a conventional incipient wetness method. The Fe-15nm/Mg(Al)O catalyst showed less activity than the Fe IW catalyst. The optimum particle size for methane dehydrogenation at 600-650ºC was found to be 10 nm; the corresponding catalyst had both the highest methane conversion and longest life-times. The generated carbon product was in the form of multi-walled CNTs over the Fe-5 nm and Fe-10 nm catalyst, while it was in the form of carbon capsules over the Fe-15 nm catalyst. Mössbauer spectra for the used Fe-10 nm catalyst revealed that Fe metal and the metastable Fe-C solution were the catalytic active phase. Catalysts deactivation was due to supersaturation of iron with carbon.

Table 5.1. Fe loading of the as-prepared catalysts by ICP analysis

Fe-5 nm	Fe-10 nm	Fe-15 nm	Fe-IW
3.2 wt %	3.2 wt %	4.2 wt %	5.0 wt %

Table 5.2. Mӧssbauer parameters of as-prepared Fe catalysts on Mg(Al)O support

Catalyst As-prepared	**I. S. mm/s**	**Q. S. mm/s**	**Width Mm/s**	**H_0 KGauss**	**%Fe**	**ID**
Fe IW	0.33	0.53	0.46		55	Fe^{3+} oxide
	0.31	0.93	0.46		37	Fe^{3+} oxide
	0.3	1.45	0.46		8	Fe^{3+} oxide
Fe-5 nm	0.31	0.69	0.52		16	Fe^{3+} oxide (Paramagnetic)
	0.32		2.06		64	Fe^{3+} oxide (SPM)
	0.45		2.6	210	20	Fe^{3+} oxide (SPM)
Fe-10 nm	0.28	0.74	0.57		5	Fe^{3+} oxide (Paramagnetic)
	0.33		2.4		60	Fe^{3+} oxide (SPM)
	0.31		5.5	217	35	Fe3+ oxide (SPM)
Fe-15 nm	0.33	0.70	1.07		13	Fe^{3+} oxide (Paramagnetic)
	0.39		6.6		75	Fe^{3+} oxide (SPM)
	0.43	0	1.5	420	12	Fe^{3+} oxide (magnetic)
Fe-5 nm (16.5K)	0.27		1.09		6	Fe^{3+} oxide (SPM)
	0.45		1.16	489	54	Fe^{3+} in site A
	0.40		1.16	440	40	Fe^{3+} in site B

Note: SPM refers to superparamagnetism, in which the ferromagnetic clusters are so small that they can randomly change direction under thermal fluctuations. Thus, the material is not magnetized except in an externally applied magnetic field, behaving like paramagnetism [153].

Table 5.3. Mössbauer Parameters of the Fe-10 nm/Mg(Al)O catalyst after 5 h reaction at 600, 650 and 700ºC (spectra collected at room temperature)

Fe-10 nm/Mg(Al)O	**I. S. mm/s**	**Q. S. mm/s**	**Width mm/s**	**H_0 KGauss**	**%Fe**	**ID**
600ºC 5h	0.33	0.74	0.73		71	Fe^{3+} oxide
	0.01	0	0.33	327	28	Fe metal
	0.2	0	0.33	199	5.5	Fe carbide
650ºC 5h	0.31	0.74	0.74		58	Fe^{3+} oxide
	-0.01	0	0.44	326	28	Fe metal
	0.25	0.04	0.44	198	14	Fe carbide
700ºC 5h	-0.12		0.31		8.5	Austenite
	0.33	0.69	0.75		25	Fe^{3+} oxide
	-0.01	0	0.33	326	30	Fe metal
	0.19	0.02	0.49	198	36.5	Fe carbide

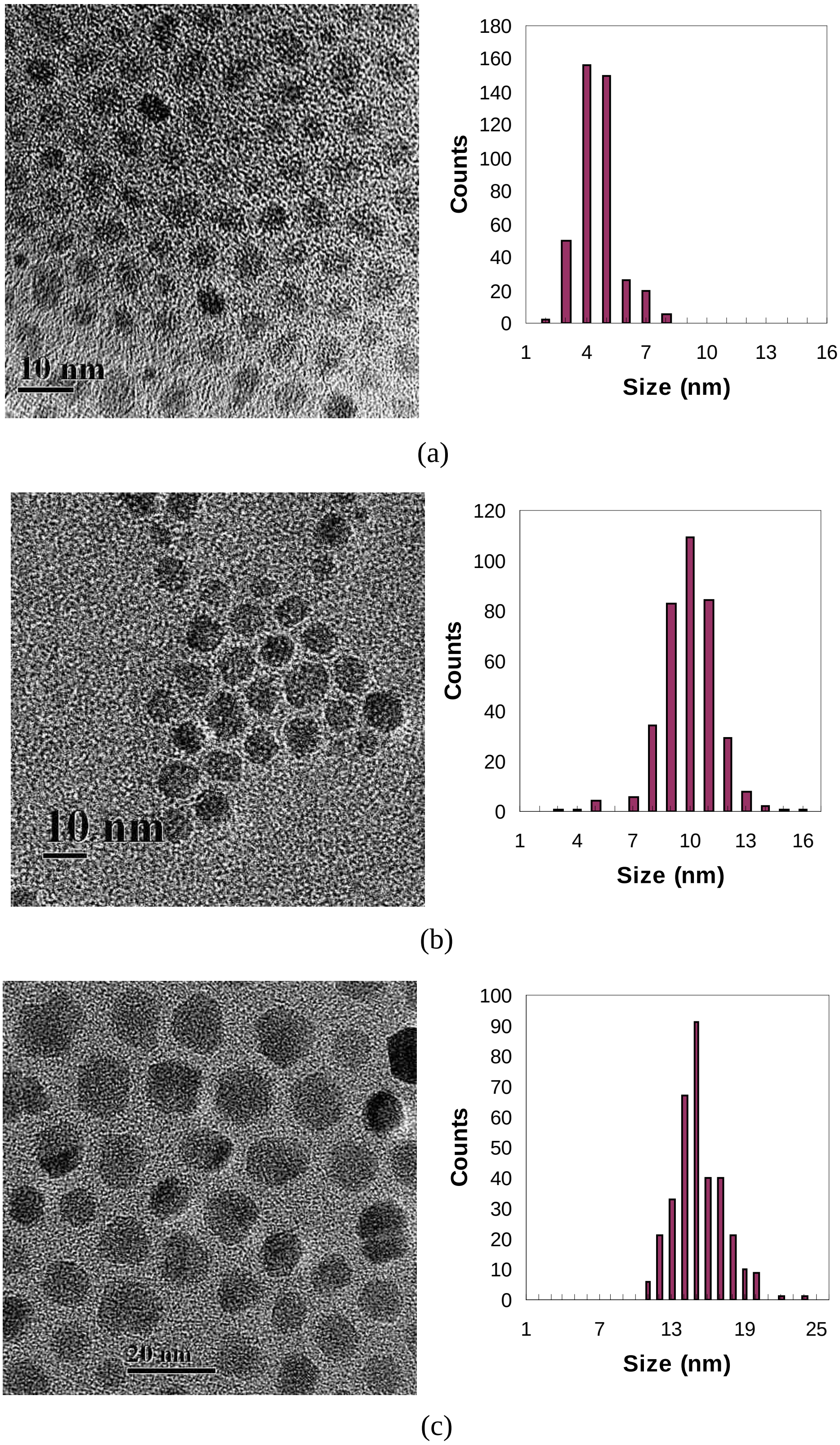

Figure 5.1. TEM micrographs of 5 nm (a), 10 nm (b) and 15 nm (c) iron oxide nanoparticles as deposited on TEM grids.

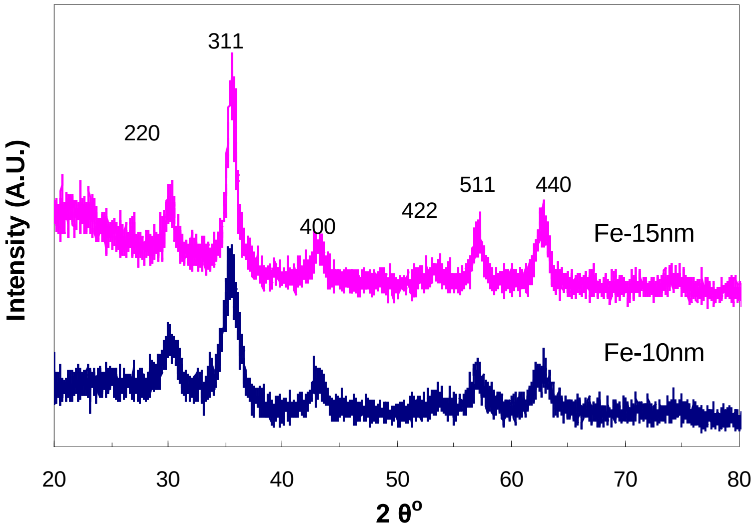

Figure 5.2. X-ray diffraction patterns of synthetic iron oxide nanoparticles with average particle sizes of 10 and 15 nm, indicating the formation of a cubic iron oxide.

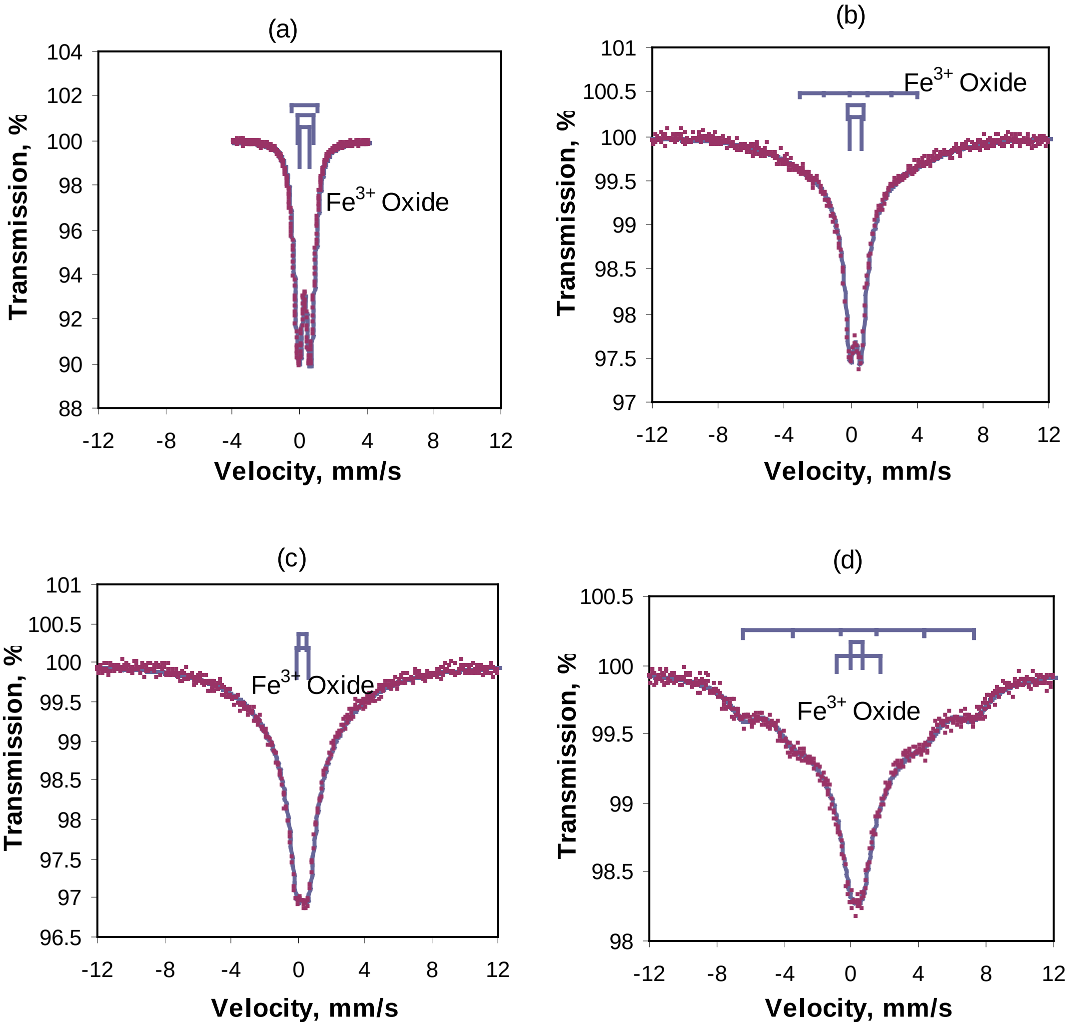

Figure 5.3. Room-temperature Mössbauer spectra of the as-prepared Fe catalysts: (a) Fe IW/Mg(Al)O; (b) Fe-5 nm/Mg(Al)O; (c) Fe-10 nm/Mg(Al)O and (d) Fe-15 nm/Mg(Al)O

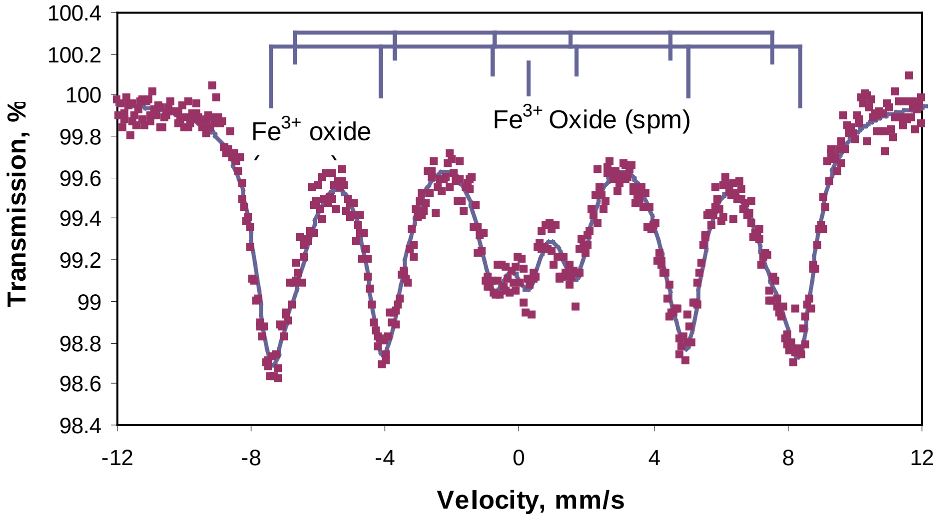

Figure 5.4. Mӧssbauer spectrum of the as-prepared Fe-5 nm/Mg(Al)O catalyst collected at 16.5 K.

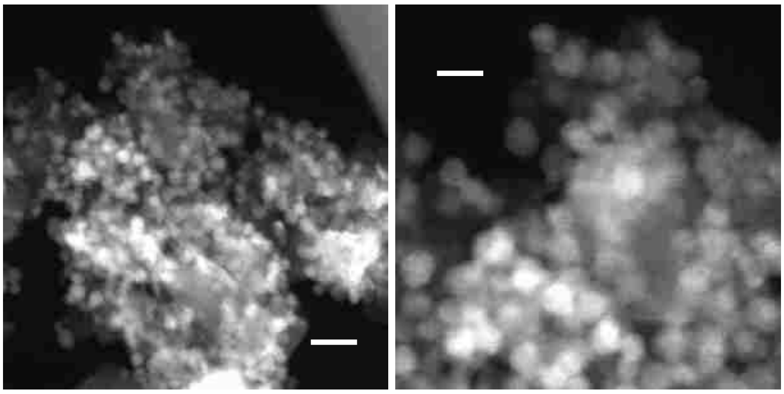

Scale bar: 20 nm Scale bar: 10 nm

(a)

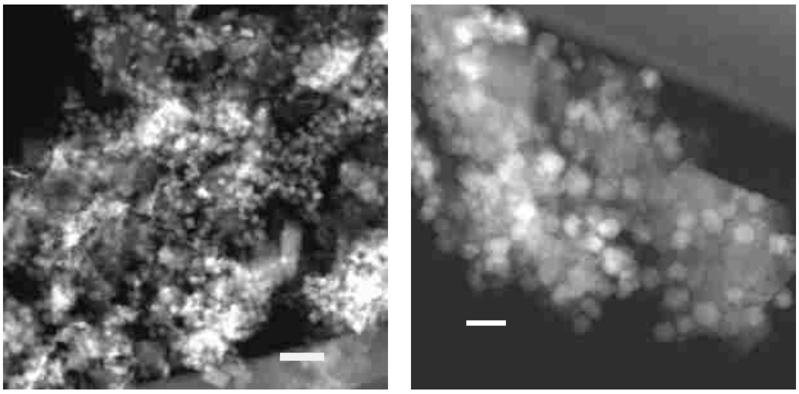

Scale bar: 50 nm Scale bar: 20 nm

(b)

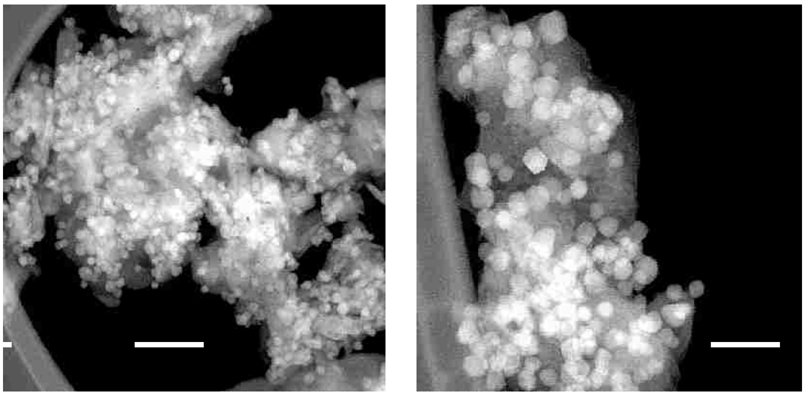

Scale bar: 100 nm Scale bar: 50 nm

(c)

Figure 5.5. STEM images of as-prepared Fe nanoparticle catalysts: (a) Fe-5 nm/Mg(Al)O; (b) Fe-10 nm/Mg(Al)O; (c) Fe-15 nm/Mg(Al)O. Iron oxide nanopartices are well dispersed onto the Mg(Al)O support in all three catalysts.

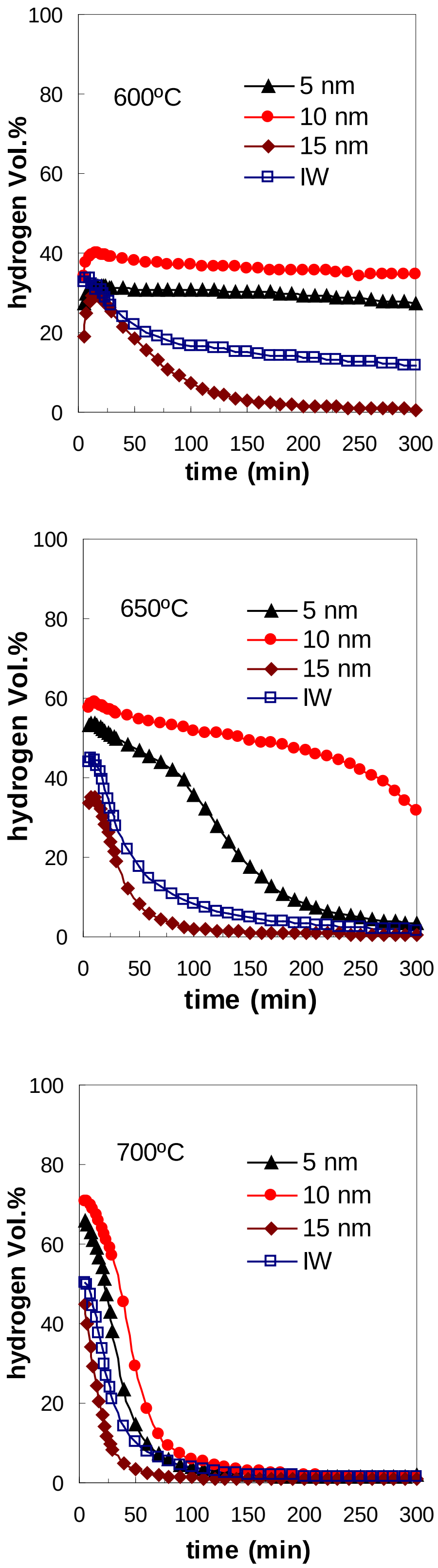

Figure 5.6. TOS H_2 production distribution at 600, 650 and 700ºC over Mg(Al)O supported Fe nanoparticle catalysts (0.2 g loading) with different particle sizes of 5nm, 10 nm and 15 nm and the Fe IW/Mg(Al)O catalyst

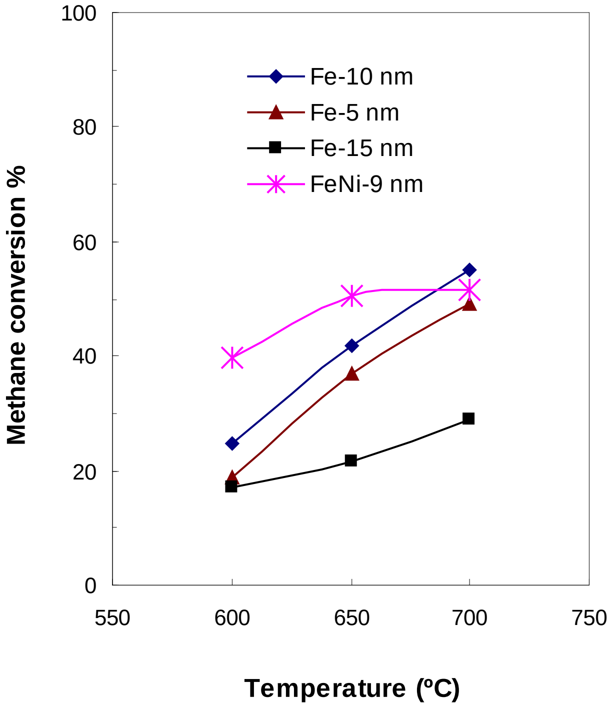

Figure 5.7. Methane conversion as a function of reaction temperature. Catalysts: Fe-10 nm/Mg(Al)O, Fe-5 nm/Mg(Al)O, Fe-15 nm/Mg(Al)O and FeNi-9nm/Mg(Al)O

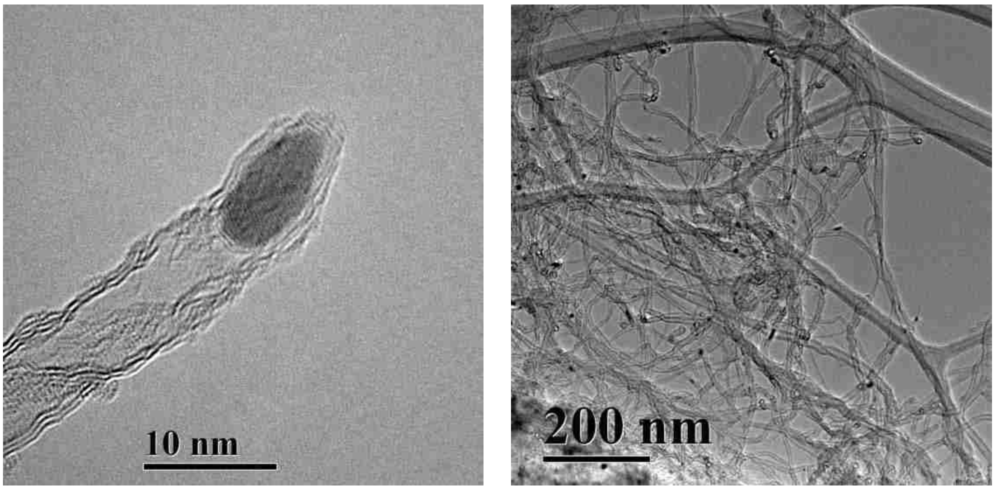

Figure 5.8. The morphologies of CNTs and Fe-5 nm nanoparticles after methane dehydrogenation reaction over Fe-5 nm/Mg(Al)O catalyst at 600ºC for 5 h

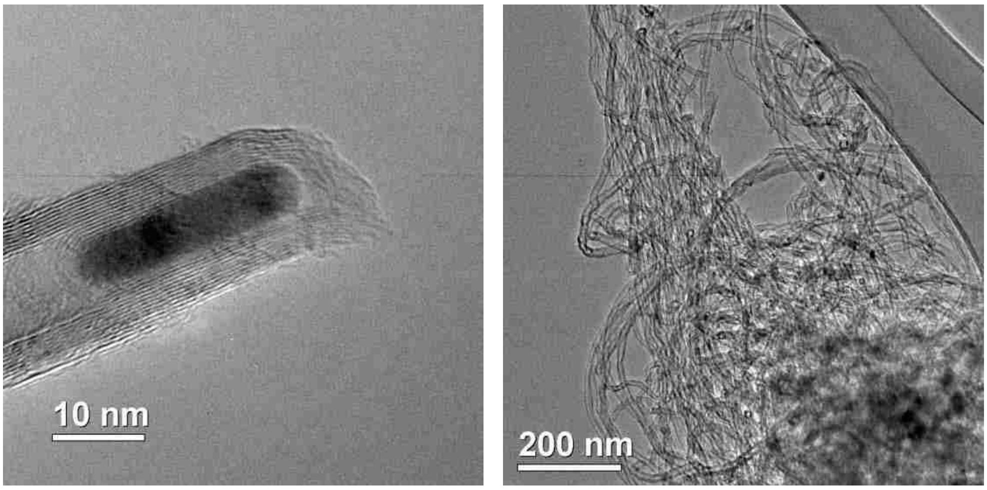

Figure 5.9. The morphologies of CNTs and Fe-10 nm nanoparticles after methane dehydrogenation reaction over Fe-10 nm/Mg(Al)O catalyst at 600ºC for 5 h.

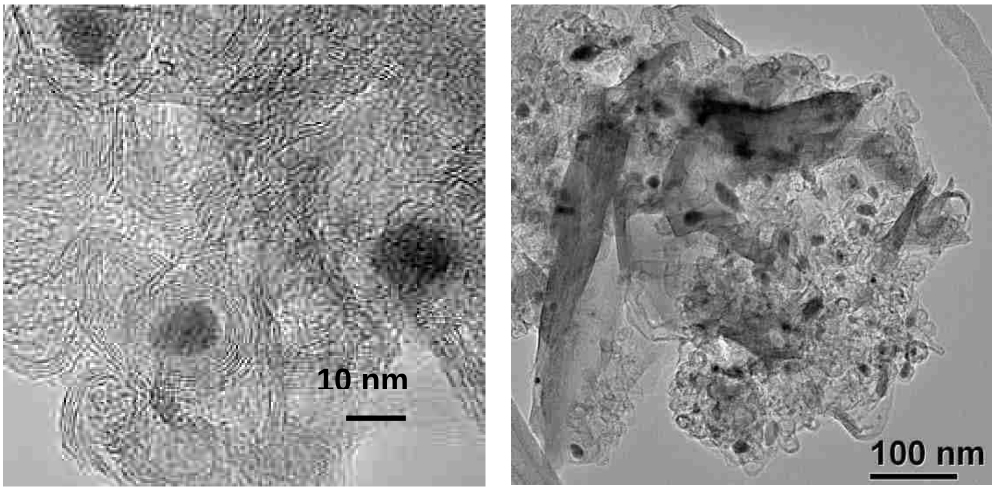

Figure 5.10. The morphologies of carbon product and Fe-15nm nanoparticles after methane dehydrogenation over Fe-15 nm/Mg(Al)O catalyst at 600ºC for 5 h.

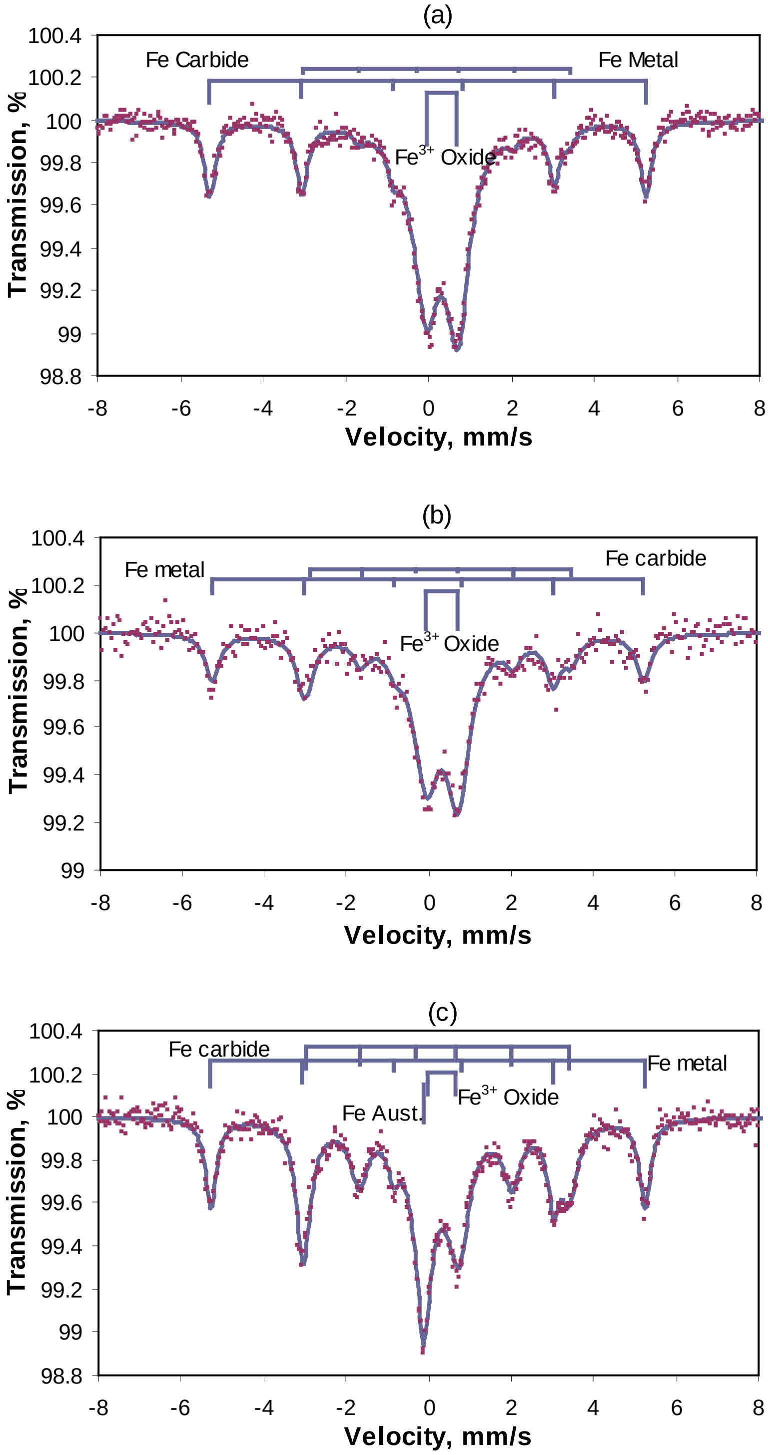

Figure 5.11. Mössbauer spectra of the Fe-10 nm/Mg(Al)O catalyst after reaction at 600ºC (a), 650ºC (b) and 700ºC (c) for 5 h. Spectra collected at room temperature.

Chapter 6. Conclusions and Future Work

6.1 Conclusions

Catalytic non-oxidative dehydrogenation of hydrocarbons is a simple one-step process to produce CO_x-free hydrogen for the energy supply of PEM fuel cells, where the purity of hydrogen is very demanding (CO<10 ppmv). The current work is designed to develop novel catalysts with excellent TOS performance and high activity for hydrocarbons dehydrogenation. Meanwhile, the generated carbon by-product should be potentially valuable in the form of carbon nanotubes (CNTs) or carbon nanofibers (CNFs) with high quality and easily purified.

It is well known that Fe, Co and Ni are good catalysts for the production of CNTs and CNFs from carbon-containing compounds such as hydrocarbons or CO. These catalysts could be potentially used in the production of hydrogen and carbon from hydrocarbon dehydrogenation. Ni has been the most investigated catalyst for this purpose. But it could only be used at temperatures below 600°C, thus limiting the conversion of hydrocarbons by dehydrogenation, which favors a high reaction temperature. Similar to Ni-based catalysts, Co-based catalysts could be used over the same temperature range of 400-600°C, but less efficiently. Fe-based catalyst were able to be used at high temperatures above 800°C for the production of CNTs with co-feed of hydrogen. There are few reports on the hydrogen production by using Fe-based catalysts due to the short life-times. In this study, monometallic Ni and Fe catalysts and bimetallic FeNi catalysts with a Fe:Ni ratio of 65:35 supported on a basic Mg(Al)O support were developed and investigated for the non-oxidative dehydrogenation of ethane and methane.

In chapter 3, a monometallic Ni IW/Mg(Al)O catalyst and a bimetallic FeNi IW/Mg(Al)O catalyst prepared by incipient wetness with total metal loading of 5 wt.% were used for ethane dehydrogenation in order to produce H_2 and easily purified CNTs. Consistent with literature reports, the Ni IW/Mg(Al)O catalyst only showed good catalytic activity at 500°C with 100% conversion of ethane to 20 vol.% H_2 and

80 vol.% methane. It had a long life-time and exhibited no loss of activity for over 16.7 h at a space velocity of 600 mL·h^{-}1·g^{-1} of undiluted ethane. Upon increasing the reaction temperature to 650ºC, the Ni IW/Mg(Al)O catalyst deactivated immediately. However, the FeNi IW/Mg(Al)O catalyst exhibited its best catalytic behavior at 650ºC and was active for more than 5 h, yielding 65 vol.% H_2, 10 vol.% CH_4, and 25 vol.% unreacted ethane. At 500ºC, it showed a high selectivity of H_2 to CH_4, but much less activity than that of the monometallic Ni catalyst. At 700ºC, both catalysts deactivated very quickly, but the FeNi catalyst showed a higher H_2 yield.

As summarized in chapters 4 and 5, a monometallic Fe-10 nm/Mg(Al)O and a bimetallic FeNi-9 nm/Mg(Al)O catalyst, both prepared by the nanoparticle impregnation method, were also investigated for methane dehydrogenation at 600, 650 and 700ºC in undiluted methane flow with a space velocity of 3000 mL· h^{-}1·g^{-1},. At 600ºC, the FeNi 9nm/Mg(Al)O catalyst maintains its catalytic activity for at least 5 h, yielding over 50 vol.% of H_2 in the effluent gas, while the activity of the Fe-10 nm/Mg(Al)O catalyst slightly declined during the 5 h reaction from the H_2 yield of 40 vol.% to 35 vol.% in the effluent gas. Upon increasing the temperature to 650ºC, the H_2 yield increased to 66 vol.% in the effluent over the FeNi 9 nm/Mg(Al)O catalyst, which maintained its activity for over 2 h and then gradually deactivated to 10 vol.% H_2 within 5 h. The Fe-10 nm/Mg(Al)O catalyst showed a higher methane dehydrogenation activity after about 10 min of reaction, yielding about 59 vol.% of H_2 in effluent gas. Then, the catalyst deactivated in two stages: the catalyst deactivated at an average rate of 4 vol. % H_2/h, from 59 vol. % to 43 vol. % H_2 in the first 4 h; after this point, the catalysts deactivated much faster and the H_2 content in the effluent gas dropped from 43 vol. % to 32 vol. % within 1 h. Both catalysts deactivated very quickly at 700ºC.

Overall, the bimetallic FeNi catalyst on Mg(Al)O support either prepared by incipient wetness method or by nanoparticle impregnation method showed improved performance for methane or ethane dehydrogenation compared with the monometallic

Ni-based and Fe-based catalysts on Mg(Al)O. Addition of Ni to Fe, forming an FeNi alloy, is able to either increase the catalytic activity or prolong the catalyst life-times at a higher reaction temperature above 600ºC. This is presumably due to the increased diffusion rate of carbon through the FeNi binary catalyst particles as discussed in chapter 3. At 700ºC, all FeNi binary catalysts deactivated very quickly, most likely due to the segregation of Ni to the FeNi catalyst particle surfaces.

A novel nanoparticle impregnation method was developed to prepare nanoparticle catalysts, in which the synthesized nanoparticles exhibited both a highly uniform composition and particle size distribution These monodispersed nonoparticles were then dispersed onto the Mg(Al)O support by ultrasonication. The resulting novel FeNi-9 nm/Mg(Al)O, Fe-10 nm/Mg(Al)O and Fe-5 nm/Mg(Al)O catalysts exhibited significantly better activity and stability for catalytic dehydrogenation of methane at moderate temperature of 600-650ºC than the similar FeNi IW/Mg(Al)O, and Fe IW/Mg(Al)O catalysts. Furthermore, comparison of the catalytic behavior of the Fe-5 nm/Mg(Al)O, Fe-10 nm/Mg(Al)O and Fe-15 nm/Mg(Al)O catalysts for methane dehydrogenation revealed that 10 nm was the optimal size for methane dehydrogenation reaction.

Also in this study, a basic Mg(Al)O compound with a Mg to Al ratio of 5 was synthesized by calcination of a MgAl-hydrotalcite prepared by co-precipitation; it was used as an alternative catalyst support. This synthesized catalyst support has high surface area, good stability towards heat and steam, and importantly, compared with alumina, it easily dissolved in dilute nitric acid. Therefore, the carbon by-product could be easily purified by a one-step dilute nitric acid treatment with the purity reaching as high as 99.6%. Moreover, the surface of this Mg(Al)O support interacted strongly with the surfactant shell (containing mainly oleic acid or oleylamine) of the synthesized nanoparticles, since it can absorb hexane dispersed catalyst nanoparticles easily by slightly stirring. Thus, it could be efficiently applied to prepare novel nanoparticle catalyst by nanoparticle impregnation method.

The morphologies of the carbon by-product are determined by the catalyst composition and the reaction temperature. Above 600ºC, over FeNi binary catalysts, Fe IW/Mg(Al)O, Fe-5 nm/Mg(Al)O and Fe-10 nm/Mg(Al)O catalysts, the carbon is in the form of multi-walled CNTs. The Fe-15 nm/Mg(Al)O catalyst could only generate carbon capsule at 600ºC, while the Ni IW/Mg(Al)O catalyst produced an onion soot/fiber mixed carbon product at 650ºC. It is noteworthy that the CNT structure produced over the Ni IW/Mg(Al)O catalyst was SCNTs. It is believed that the edges of the CNTs or CNFs are the most active and easily modified sites. Therefore, the SCNTs prepared here with purity of 99.5%, the surfaces of which are almost entirely graphitic edge sites, should have significant advantages compared to the other types of CNTs or CNFs as catalyst supports.

The following reaction mechanism was proposed for hydrocarbon dehydrogenation over the catalysts prepared in this work. The alkane is first adsorbed onto the surface of the catalyst particle, where it dissociates to surface carbon (C_s), releasing hydrogen and/or other gaseous products. The C_s dissolves into the catalyst particles and diffuses through the particle. At a high enough concentration of C_s, nucleation occurs at the particle surfaces to form filamentous carbon product. The driving force for carbon diffusion inside the catalyst particle is the concentration gradient arising from the difference in carbon solubility at the gas/catalyst surface and the CNT/catalyst particle surface. The generation of SCNTs and MWNTs over Fe, Ni or FeNi bimetallic catalysts on Mg(Al)O catalysts follows a tip-growth mechanism. Nanoscale Fe, Ni, Fe-Ni alloy and associated unsaturated metal-carbon solution particles are all catalytic active phases for alkane dehydrogenation. The “fluidity” property is observed on the catalytic active Fe and FeNi catalyst particles, since the metal particles filling the cavity inside the CNTs, behave like a liquid. The deactivation of catalysts is predominantly due to the carbon encapsulation of catalyst particles. However, the reason for the formation of carbon capsule is complicated, presumably due to the supersaturation of carbon in metal catalyst particles.

6.2 Suggestions for Future Work

Despite the above achievements, there are still a lot of interesting topics left for future research. First, as already noted, the deactivation mechanism of the catalyst for hydrocarbon dehydrogenation is still uncertain due to the limitation of the ex-situ characterization. Therefore, it is meaningful to use in-situ characterization techniques to study the reactions on these catalysts. Efforts have been devoted to using in-situ XAFS spectroscopy, which can provide detailed information about the phase changes at each step, such as those occurring during pre-reduction, reaction and deactivation. The initial experiments were only conducted to investigate the reduction behavior of Fe IW/Mg(Al)O and Fe-10 nm/Mg(Al)O catalysts by methane due to the limitations on the usage of flammable hydrogen gas in place at the National Synchrotron Light Source, Brookhaven National Laboratory. The details and the primary results were describes in reference [154]. Therefore, in-situ experiments close to actual reaction conditions need to be designed and conducted to reveal the reaction mechanisms.

Second, a single bimetallic FeNi nanoparticle catalyst, with a Fe to Ni molar ratio of 65:35, was investigated for hydrocarbon dehydrogenation. It exhibited much improved performance, compared to monometallic Ni and Fe nanoparticle catalysts, and the similar FeNi catalyst prepared by incipient wetness method. It would be very interesting to change the Fe to Ni ratio to achieve the optimal composition of Fe to Ni for hydrocarbon dehydrogenation. However, it is very challenging to prepare FeNi bimetallic nanoparticles with nickel content larger than 35% by using the method used herein, and different methods will need to be discovered.

Third, it would be of value to investigate the effect of addition of Co to the Fe catalyst on hydrocarbon dehydrogenation..

Last, but not least, potential applications of the purified carbon by-products such as SCNTs as catalyst supports are very attractive topics for future research. Ni, Ni-Cu, Pd, Ni-Pd, Fe-Co nanoparticles could be easily dispersed onto SCNTs. But the catalytic activities of these materials, potentially of importance in areas such as hydrogenation, electrolyte catalysts for fuel cell and Fischer-Tropsch synthesis, are still under investigation.

References

[1] J.P. Longwell, E.S. Rubin, J. Wilson, Progress in Energy and Combustion Science. 21 (1995) 269-360.

[2] D. Das, T.N. Veziroglu, International Journal of Hydrogen Energy. 26 (2001) 13-28.

[3] J.N. Armor, Applied Catalysis A-General. 176 (1999) 159-176.

[4] Retrieved Jan 12, 2009, from http://en.wikipedia.org/wiki/Hydrogen_economy.

[5] United State Department of Energy, National Hydrogen Road Map. april 2-3 (2002).

[6] S. Freni, G. Calogero, S. Cavallaro, J Power Sources. 87 (2000) 28-38.

[7] B.C. Enger, R. LR. Lødeng, A. Holmen, Applied Catalysis A: General. In presssed manuscript, available online (2008).

[8] M.H. Halabi, M.H.J.M. de Croon, J. van der Schaaf, P.D. Cobden, J.C. Schouten, Chem Eng J. 137 (2008) 568-578.

[9] F. G. Kaliler, B.S. Çağlayan, Z. İlsen Önsan, A. E. Aksoylu, International Journal of Hydrogen Energy. 33 (2008) 1383-1391.

[10] J.R.H. Ross, Catalysis Today. 100 (2005) 151-158.

[11] J.R. Rostrup-Nielsen, J. Sehested, J.K. Nørskov, Advances in Catalysis, Academic Press, 2002, pp. 65-139.

[12] A. Haryanto, S. Fernando, N. Murali, S. Adhikari, Energy & Fuels. 19 (2005) 2098-2106.

[13] P.V. Beurden, a literature survey, on the Catalytic Aspects of Steam-Methane Reforming (12/2004).

[14] B.T. Carvill, J.R. Hufton, M. Anand, S. Sircar, AIChE Journal. 42 (1996) 2765-2772.

[15] J.R. Hufton, S. Mayorga, S. Sircar, AIChE Journal. 45 (1999) 248-256.

[16] L. Barelli, G. Bidini, F. Gallorini, S. Servili, Energy. 33 (2008) 554-570.

[17] T. V. Choudhary, D.W. Goodman, Catalysis. 19 (2006) 164-183.

[18] T. V. Choudhary, E. Aksoylu, D. W. Goodman, Catalysis Reviews-Science and Engineering. 45 (2003) 151.

[19] S. Takenaka, H. Ogihara, I. Yamanaka, K. Otsuka, Applied Catalysis A-General. 217 (2001) 101-110.

[20] S. Takenaka, E. Kato, Y. Tomikubo, K. Otsuka, Journal of Catalysis. 219 (2003) 176-185.

[21] S. Takenaka, M. Serizawa, K. Otsuka, Journal of Catalysis. 222 (2004) 520-531.

[22] R. Guil-López, V. La Parola, M. A. Peňa, J. L. G. Fierro, Catalysis Today. 116 (2006) 289-297.

[23] G. Bonura, O. Di Blasi, L. Spadaro, F. Arena, F. Frusteri, Catalysis Today. 116 (2006) 298-303.

[24] T. V. Choudhary, C. Sivadinarayana, A. Klingerhoffer, D. W. Goodman, Study in Surface Science and Catalysis. 136 (2001) 197-202.

[25] T. V. Choudhary, D.W.Goodman, Catalysis Letters. 59 (1999) 93-94.

[26] T.V. Choudhary, D.W. Goodman, Journal of Catalysis. 192 (2000) 316-321.

[27] J. Chen, Y. Li, Z. Li, X. Zhang, Applied Catalysis A: General. 269 (2004) 179-186.

[28] S.Y. Chin, Y.-H. Chin, M.D. Amiridis, Applied Catalysis A: General. 300 (2006) 8-13.

[29] P.G. Savva, G.G. Olympiou, C.N. Costa, V.A. Ryzhkov, A.M. Efstathiou, Catalysis Today. 102-103 (2005) 78-84.

[30] V.R. Choudhary, S. Banerjee, A.M. Rajput, Applied Catalysis A: General. 234 (2002) 259-270.

[31] R.A. Couttenye, M.H. De Vila, S.L. Suib, Journal of Catalysis. 233 (2005) 317-326.

[32] Y. Li, B. Zhang, X. Tang, Y. Xu, W. Shen, Catalysis Communications. 7 (2006) 380-386.

[33] S. Takenaka, S. Kobayashi, H. Ogihara, K. Otsuka, Journal of Catalysis. 217 (2003) 79-87.

[34] A. Konieczny, K. Mondal, T. Wiltowski, P. Dydo, Int J Hydrogen Energ. 33 (2008) 264-272.

[35] M.A. Ermakova, D.Y. Ermakov, A.L. Chuvilin, G.G. Kuvshinov, Journal of Catalysis. 201 (2001) 183-197.

[36] M.A. Ermakova, D.Y. Ermakov, Catalysis Today. 77 (2002) 225-235.

[37] T.V. Reshetenko, L.B. Avdeeva, A.A. Khassin, G.N. Kustova, V.A. Ushakov, E.M. Moroz, A.N. Shmakov, V.V. Kriventsov, D.I. Kochubey, Y.T. Pavlyukhin, A.L. Chuvilin, Z.R. Ismagilov, Applied Catalysis A: General. 268 (2004) 127-138.

[38] T.V. Reshetenko, L.B. Avdeeva, V.A. Ushakov, E.M. Moroz, A.N. Shmakov, V.V. Kriventsov, D.I. Kochubey, Y.T. Pavlyukhin, A.L. Chuvilin, Z.R. Ismagilov, Applied Catalysis A: General. 270 (2004) 87-99.

[39] L.B. Avdeeva, D.I. Kochubey, S.K. Shaikhutdinov, Applied Catalysis A: General. 177 (1999) 43-51.

[40] H. Ogihara, S. Takenaka, I. Yamanaka, E. Tanabe, A. Genseki, K. Otsuka, Journal of Catalysis. 238 (2006) 353-360.

[41] A.M. Dunker, S. Kumar, P.A. Mulawa, Int J Hydrogen Energ. 31 (2006) 473-484.

[42] Z. Bai, H. Chen, B. Li, W. Li, Journal of Analytical and Applied Pyrolysis. 73 (2005) 335-341.

[43] N. Muradov, International Journal of Hydrogen Engery. 26 (2001) 1165-1175.

[44] N. Muradov, F. Smith, A. T-Raissi, Catalysis Today. 102-103 (2005) 225-233.

[45] N. Shah, Y.G. Wang, D. Panjala, G.P. Huffman, Energy & Fuels. 18 (2004) 727-735.

[46] Y.G. Wang, N. Shah, G.P. Huffman, Catalysis Today. 99 (2005) 359-364.

[47] Y.G. Wang, N. Shah, G.P. Huffman, Abstract Paper of American Chemical Society Symposium. 226 (2003) U573-U574.

[48] A. Punnoose, N. Shah, G.P. Huffman, M.S. Seehra, Fuel Processing

Technology. 83 (2003) 263-273.

[49] N. Shah, S. Pattanaik, F.E. Huggins, D. Panjala, G.P. Huffman, Fuel Processing Technology. 83 (2003) 163-173.

[50] J.-M.M. Millet, C.G. Bruce, K. Helmut, Advances in Catalysis, Academic Press, 2007, pp. 309-350.

[51] D.G. Rancourt, Hyperfine Interactions. 117 (1998) 3-38.

[52] R. Mössbauer, Hyperfine Interactions. 126 (2000) 1-12.

[53] A.M. van der Kraan, Hyperfine Interactions. 126 (2000) 107-111.

[54] J. Phillips, Hyperfine Interactions. 111 (1998) 3-16.

[55] J.W. Niemantsverdriet, Spectroscopy in catalysis: an introduction, 2nd ed., Wiley-VCH, Weinheim ; Chichester, 2000.

[56] D.C. Koningsberger, R. Prins, X-ray absorption: principles, applications, techniques of EXAFS, SEXAFS, and XANES, Wiley, New York, 1988.

[57] M. Newville (June 21, 2004), Fundamental of X-ray Absorption Fine Structure. Retrieved Jan 12, 2009, from http://cars9.uchicago.edu/xafs/NSLS_2004/Newville_Intro.pdf.

[58] M. Newville (July 25, 2008), Fundamentals of XAFS. Retrieved Jan 12, 2009, from http://cars9.uchicago.edu/xafs/xas_fun/xas_fundamentals.pdf.

[59] B. Ravel (Aug 19, 2008), Introductory and Tutorial Information on XAFS. Retrieved on Jan 12, 2009, from http://xafs.org/Tutorials.

[60] M. Newville (Mar 19, 2001), The IFEFFIT Tutorial. Retrieved Jan 12, 2009, from http://cars9.uchicago.edu/ifeffit/Documentation.

[61] M. Newville, J Synchrotron Radiation. 8 (2001) 96-100.

[62] M. Newville, J Synchrotron Radiation. 8 (2001) 322-324.

[63] S. Webb (Mar 07, 2008), SixPACK. Retrieved Jan 12, 2009, from http://www-ssrl.slac.stanford.edu/~swebb/sixpack.htm.

[64] B. Ravel, J Synchrotron Radiation. 8 (2001) 314-316.

[65] N. Shah, D. Panjala, G.P. Huffman, Energy & Fuels. 15 (2001) 1528-1534.

[66] Y.-Y. Fan, A. Kaufmann, A. Mukasyan, A. Varma, Carbon. 44 (2006) 2160-2170.

[67] A.C. Dillon, T. Gennett, K.M. Jones, J.L. Alleman, P.A. Parilla, M.J. Heben, Advanced Materials. 11 (1999) 1354-1358.

[68] K. Tohji, H. Takahashi, Y. Shinoda, N. Shimizu, B. Jeyadevan, I. Matsuoka, Y. Saito, A. Kasuya, S. Ito, Y. Nishina, J. Phys. Chem. B. 101 (1997) 1974-1978.

[69] K. Hernadi, A. Fonseca, J.B. Nagy, D. Bernaerts, J. Riga, A. Lucas, Synthetic Metals. 77 (1996) 31-34.

[70] P. Chen, H.B. Zhang, G.D. Lin, Q. Hong, K.R. Tsai, Carbon. 35 (1997) 1495-1501.

[71] E. Flahaut, A. Peigney, C. Laurent, A. Rousset, Journal of Materials Chemistry. 10 (2000) 249-252.

[72] E. Couteau, K. Hernadi, J.W. Seo, L. Thien-Nga, C. Miko, R. Gaal, L. Forro, Chemical Physics Letters. 378 (2003) 9-17.

[73] M.C. Bahome, L.L. Jewell, D. Hildebrandt, D. Glasser, N.J. Coville, Applied Catalysis A: General. 287 (2005) 60-67.

[74] H. Schaper, J.J. Berg-Slot, W.H.J. Stork, Applied Catalysis. 54 (1989) 79-90.

[75] M. Bellotto, B. Rebours, O. Clause, J. Lynch, D. Bazin, E. Elkaim, Journal of Physical Chemistry. 100 (1996) 8527-8534.

[76] P. Kustrowski, D. Sulkowska, L. Chmielarz, A. Rafalska-Lasocha, B. Dudek, R. Dziembaj, Microporous and Mesoporous Materials. 78 (2005) 11-22.

[77] M.M. Rao, B.R. Reddy, M. Jayalakshmi, V.S. Jaya, B. Sridhar, Mater Res Bull. 40 (2005) 347-359.

[78] T. Yoshida, T. Tanaka, H. Yoshida, T. Funabiki, S. Yoshida, Journal of Physical Chemistry. 100 (1996) 2302-2309.

[79] B. Ravel, M. Newville, J Synchrotron Radiation. 12 (2005) 537-541.

[80] S.M. Webb, Physica Scripta. T115 (2005) 1011-1014.

[81] A. Martins, N.M. Souza-Neto, M.C.A. Fantini, A.D. Santos, R.J. Prado, A.Y. Ramos, Journal of Applied Physics. 100 (2006) -.

[82] S. Takenaka, H. Ogihara, K. Otsuka, Journal of Catalysis. 208 (2002) 54-63.

[83] J. Shen, B. Guang, M. Tu, Y. Chen, Catalysis Today. 30 (1996) 77-82.

[84] T. Kawabata, N. Fujisaki, T. Shishido, K. Nomura, T. Sano, K. Takehira, Journal of Molecular Catalysis A: Chemical. 253 (2006) 279-289.

[85] A. Pattek-Janczyk, B. Miczko, A.W. Morawski, Applied Catalysis A: General. 141 (1996) 1-16.

[86] K. Polychronopoulou, A. Bakandritsos, V. Tzitzios, J.L.G. Fierro, A.M. Efstathiou, Journal of Catalysis. 241 (2006) 132-148.

[87] J. Zhao, F.E. Huggins, Z. Feng, G.P. Huffman, Physical Review B. 54 (1996) 3403.

[88] J.W. Snoeck, G.F. Froment, M. Fowles, Journal of Catalysis. 169 (1997) 240-249.

[89] J.W. Snoeck, G.F. Froment, M. Fowles, Journal of Catalysis. 169 (1997) 250-262.

[90] J. Rostrup-Nielsen, D.L. Trimm, Journal of Catalysis. 48 (1977) 155-165.

[91] R.T.K. Baker, Carbon. 27 (1989) 315-323.

[92] P.E. Nolan, D.C. Lynch, A.H. Cutler, Carbon. 32 (1994) 477-483.

[93] H. Dai, Accounts of Chemical Research. 35 (2002) 1035-1044.

[94] B. Bhushan, Springer Handbook of Nanotechnology, Spinger-Verlag, 2004.

[95] W. Li, C. Liang, W. Zhou, J. Qiu, Z.H. Zhou, G. Sun, Q. Xin, Journal of Physical Chemistry B. 107 (2003) 6292-6299.

[96] W. Shen, Y. Wang, X. Shi, N. Shah, F. Huggins, S. Bollineni, M. Seehra, G. Huffman, Energy & Fuels. 21 (2007) 3520-3529.

[97] J.M. Thomas, Pure and Applied Chemistry. 60 (1988) 1517-1528.

[98] R. Narayanan, M.A. El-Sayed, Journal of Physical Chemistry B. 109 (2005) 12663-12676.

[99] R. Narayanan, M.A. El-Sayed, Nano Letters. 4 (2004) 1343-1348.

[100] Y. Li, E. Boone, M.A. El-Sayed, Langmuir. 18 (2002) 4921-4925.

[101] H. Kimura, Y. Yokota, Y. Sawamoto, Catalysis Letters. 99 (2005) 133-140.

[102] H. Bönnemann, W. Brijoux, R. Brinkmann, E. Dinjus, T. Joussen, B. Korall, Angewandle Chemie International Edition (English). 30 (1991) 1344.

[103] H. Bönnemann , W. Brijoux, A. Schulze Tilling, K. Siepen, Topics in Catalysis. 4 (1997) 217-227.

[104] H. Bönnemann, W. Brijoux K. Siepen J. Hormes R. Franke J. Pollmann J. Rothe, Applied Organometallic Chemistry. 11 (1997) 783-796.

[105] H. Bönnemann, Rainer Brinkmann, Peter Neiteler, Applied Organometallic Chemistry. 8 (1994) 361-378.

[106] T. Vidakovic, M. Christov, K. Sundmacher, K.S. Nagabhushana, W. Fei, S. Kinge, H. Bönnemann, Electrochimica Acta. 52 (2007) 2277-2284.

[107] H. Bönnemann, R.Richard. Polymer International. 54 (2003) 343.

[108] X. Wang, Q. Peng, Y. Li, Accounts of Chemical Research. 40 (2007) 635-643.

[109] M. Chen, J.P. Liu, S. Sun, Journal of the American Chemical Society. 126 (2004) 8394-8395.

[110] C. N. Ramachandra Rao, Giridhar U. Kulkarni, P. John Thomas and Peter P. Edwards, Chemical Society Reviews 29 (2000) 27-35.

[111] S. Sun, C.B. Murray, D. Weller, L. Folks, A. Moser, Science. 287 (2000) 1989-1992.

[112] A.V. Blaaderen. 439 (2006) 545-546.

[113] M. Green, Chemical communications. 24 (2005) 3002-3011.

[114] Dong-Sik Bae, Kyong-Sop Han and James H. Adair, Journal of Materials Chemistry. 12 (2002) 3117 - 3120.

[115] K. Niesz, M.M. Koebel, G.A. Somorjai, Inorganica Chimica Acta. 359 (2006) 2683-2689.

[116] R. Massard, D. Uzio, C. Thomazeau, C. Pichon, J.L. Rousset, J.C. Bertolini, Journal of Catalysis. 245 (2007) 133-143.

[117] T. Saito, S. Ohshima, W.C. Xu, H. Ago, M. Yumura, S. Iijima, Journal of Physical Chemistry B. 109 (2005) 10647-10652.

[118] C.L. Cheung, A. Kurtz, H. Park, C.M. Lieber, Journal of Physical Chemistry B. 106 (2002) 2429-2433.

[119] Y. Li, J. Liu, Y. Wang, Z.L. Wang, Chemistry of Materials. 13 (2001) 1008-1014.

[120] J. Park, K. An, Y. Hwang, J.-G. Park, H.-J. Noh, J.-Y. Kim, J.-H. Park, N.-M. Hwang, T. Hyeon, Nature Materials. 3 (2004) 891-895.

[121] S.U. Son, Y. Jang, J. Park, H.B. Na, H.M. Park, H.J. Yun, J. Lee, T. Hyeon, Journal of the American Chemical Society. 126 (2004) 5026-5027.

[122] T. Hyeon, Chemical Communications (2003) 927-934.

[123] S. Sun, H. Zeng, D.B. Robinson, S. Raoux, P.M. Rice, S.X. Wang, G. Li, Journal of the American Chemical Society. 126 (2004) 273-279.

[124] Y. Hou, H. Kondoh, T. Ohta, S. Gao, Applied Surface Science. 241 (2005) 218-222.

[125] N. Cordente, M. Respaud, F. Senocq, M.J. Casanove, C. Amiens, B. Chaudret, Nano Letters. 1 (2001) 565-568.

[126] M.-S. Liao, Q.-E. Zhang, Journal of Molecular Catalysis A: Chemical. 136 (1998) 185-194.

[127] T.V. Choudhary, E. Aksoylu, D.W. Goodman, Catalysis Reviews-Science and

Engineering. 45 (2003) 151-203.

[128] O.P. Krivoruchko, A.N. Shmakov, V.I. Zaikovskii, Nuclear Instruments & Methods in Physics Research Section a-Accelerators Spectrometers Detectors and Associated Equipment. 470 (2001) 198-201.

[129] M.S. Y. Nakamura, Journal of physical scociety Japan. 19 (1964) 1177.

[130] Y.T. Y. Nakamura, M. Shiga, Journal of physical scociety Japan. 25 (1968) 287.

[131] K. Brzózka, B. Górka, M. Gawroński, T. Szumiata, Czechoslovak, Journal of physics. 54 Suppl. D (2004) D145.

[132] Yu.I. Petrov, E.A. Shafranovsky, Journal of Nanoparticle Research. 3 (2001) 417-430.

[133] F. Dury, E.M. Gaigneaux, P. Ruiz, Applied Catalysis A: General. 242 (2003) 187-203.

[134] F. Haass, M. Bron, H. Fuess, P. Claus, Applied Catalysis A: General. 318 (2007) 9-16.

[135] P.J. Schilling, J.H. He, J. Cheng, E. Ma, Applied Physics Letters. 68 (1996) 767-769.

[136] S. Pascarelli, F. Boscherini, S. Mobilio, K. Lawniczak-Jablonska, R. Kozubski, Physical Review B. 49 (1994) 14984.

[137] S. Yin, Z. Xie, J. Zhang, Q. Bian, W. Yan, Z. Jiang, S. Wei, Physica Scripta. T115 (2005) 421-423.

[138] M. Tomellini, I. Davoli, D. Gozzi, Journal of Alloys and Compounds. 218 (1995) 237-243.

[139] B. Ozturk, V. L. Fearing, J. A. Ruth and G. Simkovich, Metallurgical and Materials Transactions A. 13 (1982) 1871-1873.

[140] C. Park, N.M. Rodriguez, R.T.K. Baker, Journal of Catalysis. 169 (1997) 212-227.

[141] C. Park, R.T.K. Baker, Journal of Catalysis. 179 (1998) 361-374.

[142] A.T. Bell, Science. 299 (2003) 1688-1691.

[143] M. Valden, X. Lai, D.W. Goodman, Science. 281 (1998) 1647-1650.

[144] M.S. Chen, D.W. Goodman, Catalysis Today. 111 (2006) 22-33.

[145] Z. Liu, M. Shamsuzzoha, E.T. Ada, W.M. Reichert, D.E. Nikles, Journal of Power Sources. 164 (2007) 472-480.

[146] K. Bergamaski, A.L.N. Pinheiro, E. Teixeira-Neto, F.C. Nart, Journal of Physical Chemistry B. 110 (2006) 19271-19279.

[147] G.L. Bezemer, J.H. Bitter, H.P.C.E. Kuipers, H. Oosterbeek, J.E. Holewijn, X. Xu, F. Kapteijn, A.J. vanDillen, K.P. deJong, Journal of the American Chemical Society. 128 (2006) 3956-3964.

[148] M.A. Ermakova, D.Y. Ermakov, G.G. Kuvshinov, L.M. Plyasova, Journal of Catalysis. 187 (1999) 77-84.

[149] Z.X. Yu, D. Chen, B. Totdal, A. Holmen, Catalysis Today. 100 (2005) 261-267.

[150] R. T. K. Baker, N. M. Rodriguez, Materials Research Society Symposium Proceeding. 329 (1994) 251-259.

[151] W. Shen, F.E. Huggins, N. Shah, G. Jacobs, Y. Wang, X. Shi, G. P. Huffman, Applied Catalysis A: General. 351 (2008) 102-110.

[152] G.G. Tibbetts, M.G. Devour, E.J. Rodda, Carbon. 25 (1987) 367-375.

[153] Retrieved Jan 12, 2009,
from http://en.wikipedia.org/wiki/Superparamagnetism.

[154] F. E. Huggins, W. Shen, N. Cprek, N. Shah, N. S. Marinkovic, G. P. Huffman, Energy and Fuels. 22 (2008) 3620-3625.

Vita

BORN: May 26th, 1973, Huainan, Anhui Province, China

EDUCATION

1996-1999: M.S. Chemical Engineering Technology
East China University of Science & Technology (ECUST), Shanghai, China
1992-1996: B.S. Chemical Engineering Technology of Coal
East China University of Science & Technology (ECUST), Shanghai, China

SELECTED JOURNAL PUBLICATIONS

- F. E. Huggins, **W. Shen,** N. Cprek, N. Shah, N. Marinkovic, G. P. Huffman, "In Situ XANES Spectroscopic Investigation of the Reduction of Iron-based Catalysts for Non-oxidative Alkane Dehydrogenation", *Energy & Fuels*, 2008, 22(6), 3620.
- **W. Shen**, Y. Wang, F.E. Huggins, N. Shah, G.P. Huffman, "Novel FeNi nanopartice catalyst for the production of CO_x-free H_2 and carbon nanotubes by non-oxidative deyhydrogenation of methane", *Applied catalysis A: General*, 2008, 351, 102.
- **W. Shen,** N. Shah, F. E. Huggins, G. P. Huffman, "Non-oxidative dehydrogenation of methane over novel Fe/Mg(Al)O nanoparticle catalysts: effect of particle size", to be submitted to *Applied catalysis A: General*
- **W. Shen**, Y. Wang, X. Shi, N. Shah, F. Huggins, G.P. Huffman "Catalytic non-oxidative dehydrogenation of ethane over Fe-Ni and Ni catalysts supported on Mg(Al)O to produce pure hydrogen and easily-purified carbon nanotubes", *Energy & Fuels*, 2007, 21(6), 3520.
- **W. Shen**, N. Shah, F. Huggins, G. Huffman, "Nanoparticle catalysts for the production of CO-free hydrogen and carbon nanotubes by non-oxidative dehydrogenation of methane" *Prepr. Pap.-Am. Chem. Soc., Div. Fuel Chem.* 2007**,** *52 (2),* 463
- B. Dou, **W. Shen**, J. Gao, X. Sha, "Adsorption of alkali metal vapor from high-temperature coal-derived gas by solid sorbents", *Fuel Processing Technology,* 2003, 82(1), 51.
- B. Dou, M. Zhang, J. Gao, **W. Shen**, X. Sha, "High-temperature removal of NH_3, organic sulfur, HCl, and Tar component from coal-derived gas", *Industrial & Engineering Chemistry Research*, 2002, 41(17), 4195.
- B. Dou, **W. Shen**, X. Sha, "Study on Removal of HCl, NH_3, Organic Sulphur, Tar Component and Alkali Metal Vapor in High Temperature Coal gas" *Gas & Heat*, 2001, 21, 195.
- **W. Shen**, R. Xing, G. Zhao, X. Shao, "Study of Operating Condition for Catalytic Conversion of Organic Sulphur in Hot Coal Gas", *Gas & Heat*, 2000, 20, 327.
- **W. Shen**, B. Dou, R. Xing, "Removal of Alkali Metal Vapor from Hot Coal Gas", *Gas and Heat*, 2000, 20, 403.
- B. Dou, **W. Shen**, X. Sha, "Development of Disposal Sorbent for HCl Removal From High-temperature Coal-derived Gas", *Gas and Heat*, 2000,20, 88.

- **W. Shen**, L. Jun, Q. Jun, X. Sha, “Ammonia Removal in Hot Coal Gas (I) Screening of Catalyst for Ammonia Catalytic Decomposition”, *Ranliao Huaxue xuebao,* 1999, 27, 455.
- **W. Shen**, J. Lu, B. Dou, R. Xing, X. Sha, G. Zhao, H. Li, “Ammonia Removal in Hot Coal Gas. II. Kinetic Study on Ammonia Catalytic Decomposition”, *Ranliao Huaxue Xuebao,* 1999, 27, 462.
- C. Wan, X. Sha, **W. Shen**, “Investigation into High-temperature Coal Gas Desulfurization Using Cu-Mn-O Based Sorbent (I) Desulfurization of Cu-Mn-O Based Sorbent”, *Ranliao Huaxue Xuebao,* 1998, 26, 400.
- **W. Shen**, L. Xiong, X. Sha, “Development of Muti-functional Purificant for Hot Coal Gas”, *Clean Coal Technology,* 1998, 4, 2.

SELECTED CONFERENCES & PRESENTATIONS

- **W. Shen,** F. E. Huggins, G. P. Huffman, “Novel approach for the CO-free hydrogen production by non-oxidative dehydrogenation of hydrocarbons”, Symposium organized by Tri-State Catalysis Society, 2007.
- **W. Shen,** N. Shah, F. E. Huggins, G. P. Huffman, “Nanoparticle catalysts for the production of CO-free Hydrogen and carbon nanotbues by non-oxidative dehydrogenation of methane”, 234th ACS national meeting, Boston, MA, USA, Aug. 19-23, 2007.
- **W. Shen**, Y. Wang, N. Shah, F. Huggins, G. Huffman, “Development of Highly active nanoscale catalysts for production of CO free H_2 by dehydrogenation of methane” AIChE annual meeting, San Francisco, CA, Nov. 12-17, 2006.
- Y. Wang, N. Shah, **W. Shen**, F. Huggins, G. Huffman, “Production of H_2 and carbon nanotubes by catalytic non-oxidative dehydrogenation of hydrocarbon gases” American Chemistry Society, Division of Fuel Chemistry, 2006, 51(2), 465.
- C. Wan, X. Sha, **W. Shen**, L. Xiong, “An investigation into Cu-Mn Based Sorbent for Hot Gas Desulfurization”, Pittsburgh Coal Conference, 1998, 15th, 1220.
- **W. Shen,** B. Dou, X. Sha, “Ammonia Removal in Hot Coal Gas—(I) Screening of Catalyst for Ammonia Catalytic Decomposition”, Prospect for Coal Science in the 21th Century, 1481, Shanxi Science & Technology Press, 1999.
- **W. Shen,** B. Dou, X. Sha, “Ammonia Removal in Hot Coal Gas—(II) Kinetic Research of Ammonia Catalytic Decomposition”, Prospect for Coal Science in the 21th Century, 1377, Shanxi Science & Technology Press, 1999.